The Thesis Committee for Xufeng Liu
Certifies that this is the approved version of the following thesis:

Geologic Setting and Reservoir Characterization of Barnett Formation in Southeast Fort Worth Basin, Central Texas

APPROVED BY
SUPERVISING COMMITTEE:

William L. Fisher, Co-Supervisor

Robert G. Loucks, Co-Supervisor

Ronald J. Steel

Geologic Setting and Reservoir Characterization of Barnett Formation in Southeast Fort Worth Basin, Central Texas

by

Xufeng Liu, B.E.; B.S.

Thesis

Presented to the Faculty of the Graduate School of

The University of Texas at Austin

in Partial Fulfillment

of the Requirements

for the Degree of

Master of Science in Geological Sciences

The University of Texas at Austin

August, 2014

Dedication

This thesis is lovingly and gratefully dedicated to my mother: Ren Song Qing, who guided me with meticulous care and nurtured my growth, and my father: Liu Xian Tai, who inspired me throughout my childhood and later life to be a dedicated geologist and a conscientious person.

Acknowledgements

First of all, I offer my sincerest gratitude to my co-supervisors, Dr. Robert G. Loucks and Dr. William L. Fisher, for giving me great help in my academic research and for guiding me in completing this thesis. Their advice inspired me to accomplish what I wanted to achieve and showed me my path forward. Without their help, I could not have transformed my ideas and the seemingly lifeless "rocks" into a scientific thesis. I also want to thank my thesis committee member, Dr. Ronald J. Steel, for his useful comments and discussions.

My great gratitude also goes to members of the Mudrock Systems Research Laboratory (MSRL) at the Bureau of Economic Geology, UT Austin. The researchers there offered me a Research Assistant position in their group and enabled me to discuss my work with the entire team of experts and students, an opportunity that advanced my knowledge of mudrocks.

I want to thank Marathon Oil Company for providing core material for this thesis. I also thank Dr. Harry Rowe and his UT students, who measured the XRF and TOC of the core. Many thanks to Dr. Qilong Fu, a researcher in the MSRL and Sloan Project, who provided me useful well data on wireline-log cross sections; Patrick Smith, an expert in SEM, for patiently helping me capture information using the SEM; and Nathan Ivicic of the Bureau's Core Research Center, who laid out the core and cut the samples for thin

sections. Many thanks also go to Amanda Masterson, a professional editor, for helping me edit my thesis to make it more fluent in English, my second language.

Finally, I thank my family, especially my parents, who continue to offer me spiritual support and give me strength to keep going. A big thank you also goes to my uncle, Peter Wang, who gave me much support and care while I was in the United States.

Last but not least, I thank all of my friends, both in China and in the United States, especially Li Wen Jing, Shao Shu Xiao, Gan Wei and Wei Xiaojie who helped me resolve all kinds of issues, not only in my research but also in my everyday life.

Abstract

Geologic Setting and Reservoir Characterization of Barnett Formation in Southeast Fort Worth Basin, Central Texas

Xufeng Liu, M.S. Geo. Sci.

The University of Texas at Austin, 2014

Co-Supervisors: William L. Fisher and Robert G. Loucks

The Mississippian Barnett Formation is a prolific shale-gas reservoir that was deposited in the Fort Worth Basin, Texas. Many previous studies of the Barnett Formation have been conducted in the main production area; few studies have been made of the Barnett Formation in the southern part of the basin, which is a less productive area. In the present research, several cores from the Barnett Formation in Hamilton County, southeast Fort Worth Basin, are studied in detail.

Two vertical, continuous cores from Hamilton County, Texas, were studied to delineate the depositional setting, lithofacies, pore types, and reservoir quality of the Barnett Formation in the area. Five lithofacies were defined by analysis of the two cores: (1) laminated clay-rich silty and skeletal peloidal siliceous mudstone; 2) laminated skeletal silty peloidal siliceous mudstone; 3) nonlaminated silty peloidal calcareous mudstone; 4) laminated and nonlaminated skeletal calcareous mudstone; and 5) skeletal phosphatic packstone to grainstone. As indicated from this study, the dominant organic matter type is

a mixture of Type II (major) and Type III (minor) kerogen having a mean TOC content of approximately 4%. Analysis of Rock Eval data shows that most of the interval is within the oil window; calculated R_o is approximately 0.9%. Organic geochemistry shows that the hydrocarbon generation potential of the abundant oil-prone kerogen was excellent. Mineralogical analysis reveals that the two types of siliceous mudstone, which are similar in composition to the siliceous mudstone in the main producing area in the northern Fort Worth Basin, are good for hydraulic fracturing and production, but they are also limited by their marginal thickness. Organic matter pores, which are the dominant pore types in these two cores, are consistent with pore types found in currently producing wells in the Newark East Field.

This research also suggests that the deposition of Barnett Formation was controlled largely by basinal geometry, suspension settling, and slope-originated gravity-flow events. Skeletal deposits and carbonate-silt starved ripples suggest gravity-flow deposits and bottom-current reworking during deposition. Redox-sensitive elements and degree of pyritization both indicate anoxic/euxinic conditions during the deposition of the Barnett Formation.

Keywords: Barnett, geochemistry, pores, shale gas, sedimentology

Table of Contents

List of Tables xii

List of Figures xiii

INTRODUCTION 1

Barnett Shale Gas Resources 1

Objective 2

Previous Work 4

REGIONAL GEOLOGY OF THE FORT WORTH BASIN 6

Evolution of Fort Worth Basin 6

Stratigraphic Relationship of Barnett Formation 8

Paleogeography 10

Sedimentary Sources 12

Barnett Formation in Hamilton County 14

METHODOLOGY 18

Core and Wireline-Log Study 18

XRF-based Chemical Data 18

Thin-Section Study 19

Core Description 21

Inorganic Geochemistry 21

Cross Plot of Si% versus Al% 23

Paleoredox: Molybdenum Content and DOP_T 23

Organic Geochemistry 24

XRD Study 25

SEM Study 25

MINERALOGY 27

Introduction 27

Extrabasinal Particles 30

Intrabasinal Particles 33

Authigenic Quartz 33
Calcite 35
Calcite Concretion 35
Fracture Fills 40
Bivalve-related Calcite 40
Dolomite 43
Pyrite 43
Peloids 46
Rounded Peloids 46
Flat Peloids 47
Phosphate 49
Carbonate Intraclasts 50
Glauconite 50
Fossils 54
Agglutinated Foraminiferas 54
Radiolarians 55
Sponge Spicules 58
Bivalves, Ostracods and Brachiopods 58
Other Fossils 61

LITHOFACIES 63

Introduction 63
Laminated Clay-rich Silty Peloidal Siliceous Mudstone 64
Laminated Skeletal Silty Peloidal Siliceous Mudstone 66
Nonlaminated Silty Peloidal Calcareous Mudstone 68
Nonlaminated Silty Peloidal Calcareous Mudstone 70
Nonlaminated Skeletal Calcareous Mudstone 70
Laminated Skeletal Calcareous Mudstone 71
Skeletal Phosphatic Packstone to Grainstone 74

LITHOSTRATIGRAPHY **76**

INORGANIC GEOCHEMISTRY **80**

ORGANIC GEOCHEMISTRY **87**

Total Organic Carbon (TOC) 87

Kerogen Type 89

Thermal Maturity 91

Hydrocarbon Generation Potential 92

PORE TYPES **94**

Interparticle Pores 94

Intraparticle Pores 96

Organic Matter Pores 99

DISCUSSION **101**

Lithofacies and Depositional Processes 101

Depositional Environment 105

Reservoir Quality 106

CONCLUSION **108**

APPENDIX A **109**

REFERENCES **116**

VITA **127**

List of Tables

Table A1: Thin-sections used in this study.....109

Table A2: XRF sampling intervals of Hamilton County cores.....111

Table A3: SEM samples used in this study 112

Table A4: Organic chemical data used in this study.....113

Table A5: XRD data used in this study.....114

List of Figures

Figure 1: Map of general structural features of the Fort Worth Basin and the location of cored wells used in this investigation.. 3

Figure 2: General stratigraphic relationship of the Barnett Formation and the overlying and underlying formations.. 9

Figure 3: Paleogeographic maps.. 11

Figure 4: Possible source areas of sediment for the Barnett Formation in the Fort Worth Basin during the deposition of Barnett Formation.. 13

Figure 5: Line of section for the northeast-to-southeast cross section shown in Figure 6, from Denton County to Hamilton County. 16

Figure 6: Wireline-log cross section.....17

Figure 7: XRF geochemical data.. 20

Figure 8: Core descriptions of Mesquite No. 1 and Lake Davis No. 1. 22

Figure 9: Three end-members of matrix were identified using the XRF-based chemical data. 26

Figure 10: Compositional ternary plot showing relative proportions of mineralogy, based on XRD data. 28

Figure 11: Combination of SEM photomicrograph and EDAX map showing an example of the grain types in the Barnett Formation 29

Figure 12: Detrital quartz silt in a peloid-rich matrix.....31

Figure 13: Wood fragments as seen in core. 32

Figure 14: Authigenic quartz.....34

Figure 15: Calcite concretions.. 37

Figure 16: Calcite fracture fills.....41

Figure 17: Bivalve diagenesis 42

Figure 18: Authigenic dolomite as seen in the Lake Davis No. 1, 4175.1 ft thin section. 44
Figure 19: Pyrite 45
Figure 20: Peloids 48
Figure 21: Phosphatic grains 51
Figure 22: Intraclasts 52
Figure 23: Glauconite. 53
Figure 24: Agglutinated foraminiferas 56
Figure 25: Radiolarians 57
Figure 26: Examples of sponge spicules 59
Figure 27: Bivalves, brachiopods, and ostracods 60
Figure 28: Cephalopods and crinoids 62
Figure 29: Laminated clay-rich silty and skeletal peloidal siliceous mudstone. 65
Figure 30: Laminated skeletal silty peloidal siliceous mudstone 67
Figure 31: Laminated and nonlaminated skeletal calcareous mudstone 69
Figure 32: Nonlaminated skeletal calcareous mudstone 72
Figure 33: Laminated skeletal calcareous mudstone 73
Figure 34: Skeletal phosphatic packstone to grainstone 75
Figure 35: Lithostratigraphy correlations between the Mesquite No. 1 and Lake Davis No. 1. 79
Figure 36: Cross plot of Si% and Al% 81
Figure 37: Comparison of Mo content in normal gray shale and Mo content in Hamilton County 84
Figure 38: DOP_T plot of the Mesquite No. 1 core. 85
Figure 39: Plot showing weak correlation between DOP_T and TOC 86

Figure 40: Total Organic Carbon data. 88
Figure 41: Kerogen type. 90
Figure 42: Histogram of thermal maturity (calculated R_o from RockEval). 91
Figure 43: Dembicki plot showing hydrocarbon generation potential. 93
Figure 44: Example of interparticle pores 95
Figure 45: Example of intraparticle pores 97
Figure 46: Examples of intraparticle pores and organic matter pores. 98
Figure 47: Examples of organic matter pores 100

INTRODUCTION

BARNETT SHALE GAS RESOURCES

The Barnett Formation, which was deposited in the deeper water foreland Fort Worth Basin of North-Central Texas, is a well-known economic shale-gas system. It was deposited under storm wave-base from 345 Ma to 320 Ma during Mississippian time (Loucks and Ruppel, 2007). The Barnett Formation is both a primary source rock for Paleozoic reservoirs in Fort Worth Basin and a widespread unconventional gas and oil reservoir (Montgomery et al, 2005; Pollastro et al., 2007). Within the Fort Worth Basin, the areas of Denton, Wise, and Tarrant Counties are the center of Barnett Formation production. Extensive geologic and engineering research has been conducted on this northern producing area. However, until recently, a synthesis of the lithofacies, depositional characteristics, and reservoir characterization of the Barnett Formation in the southern Fort Worth Basin had been relatively ignored (e.g. Bunting and Breyer, 2012). This research will focus on the Barnett Formation in Hamilton County, in the southeastern part of the Fort Worth Basin, in Central Texas (Figure 1).

Shale gas reservoirs are typically source rocks as well as reservoir rocks and cap rocks (Schmoker, 1995). Before the 1980s, the Barnett Formation was not a target of exploratory efforts, and initial recoveries from the low-permeability reservoir were largely uneconomical. In the mid-1990s, drilling established a core productive area, Newark East field, in the northern part of the basin (Montgomery et al, 2005) and then utilization of horizontal drilling in 2003 dramatically increases the recovery. Now the Barnett Formation

continues to be an active target for shale gas in the Fort Worth Basin, in which 95% of the wells are horizontal (Abouelresh and Slatt, 2012). A comprehensive study of the reserve and production potential of the Barnett, conducted by Bureau of Economic Geology researchers from 2011 to 2013, forecasts a cumulative 44 trillion cubic feet (TCF) of recoverable reserves. Annual production declines in a predictable trend from the current peak of 2 TCF per year to about 900 billion cubic feet (BCF) per year by 2030 (Browning et al., 2013).

OBJECTIVE

In this study, several methods were applied to perform a comprehensive lithofacies classification and preliminary reservoir characterization of the Barnett Formation in southeastern Fort Worth Basin, using two continuous cores from wells in Hamilton County: the Mesquite No. 1 and Lake Davis No. 1 (Figure 1). The critical research questions in this area are: 1) what is the dominant lithofacies 2) what are the different mineral components and their potential for hydraulic fracturing; 3) what are the depositional environments and the dominant depositional processes; 4) what are the dominant pore types; and 5) what is the reservoir quality. Overall, the objective of this research is to answer these questions for the Barnett Formation in Hamilton County as part of a larger ongoing study of the regional Barnett system. This study will subsequently provide a general reference for the future geologic and production research in this area.

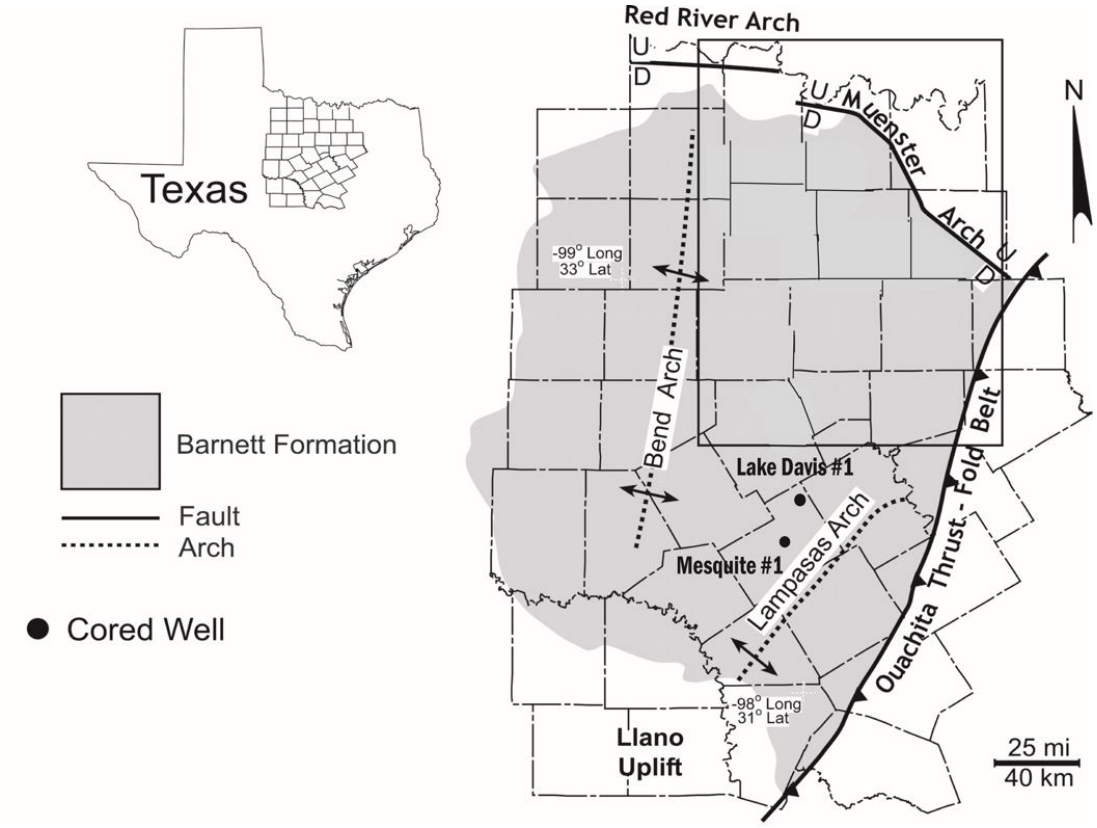

Figure 1: Map of general structural features of the Fort Worth Basin and the location of cored wells used in this investigation. Map is modified from Loucks and Ruppel (2007).

PREVIOUS WORK

Before the Barnett Formation was recognized as an unconventional reservoir, early research focused on the contact relationships of Carboniferous strata, based on the study of outcrops in San Saba and Lampasas Counties (Plummer and Moore, 1922; Plummer and Scott, 1937; Cheney, 1940; Oden, 1958; Pickens, 1959; McKinney, 1963; Kuich, 1964; Stitt, 1964; Turner, 1970). Turner (1957) first summarized the Paleozoic stratigraphy of the entire Fort Worth Basin. Later, Flippin (1982) and Walper (1982) discussed the structure and tectonic evolution of the Fort Worth Basin.

Currently, the Barnett Formation has been producing for more than 30 years, and many studies of the petroleum geology and geologic evolution of the entire basin have been made, especially in the main producing area (e.g., Montgomery et al., 2005; Hickey and Henk, 2007; Jarvie et al., 2007; Loucks and Ruppel, 2007; Pollastro et al., 2007). Loucks and Ruppel (2007) classified the Barnett Formation into three general lithofacies: 1) laminated siliceous mudstone; 2) laminated argillaceous lime mudstone (marl); and 3) skeletal argillaceous lime packstone. Abouelresh and Slatt (2012) studied Johnson County, in the south part of the basin, and they identified 10 facies. Bunting and Breyer (2012) also published a paper on the lithology of Johnson County, and Milliken et al. (2012) reported on the carbonate lithology of the Barnett using their extensive research on the northern, central, and southern parts of the Fort Worth Basin. Papazis (2005) and Bunting (2007) completed two detailed Barnett Formation core descriptions during their graduate studies. Few articles have been published specifically on the inorganic geochemistry of the Barnett Formation. Rowe et al. (2008) published a research paper on the geochemical depositional

environment. Recently researchers have begun to apply conventional sequence stratigraphy concepts to the deposition pattern of the Barnett Formation but without much success (Abouelresh and Slatt, 2012). Overall, very little attention has been paid to the southeastern part to the main producing area.

REGIONAL GEOLOGY OF THE FORT WORTH BASIN

EVOLUTION OF FORT WORTH BASIN

The origin and evolution of the Fort Worth Basin (FWB) have been discussed from many points of view, especially the basin's structure and tectonic development (Turner, 1957; Flawn et al., 1961; Henry, 1982; Walper, 1982; Flippin, 1982). Structures in the Fort Worth Basin include both major and minor faulting, local folding, fracturing, and karst-related collapse features (Montgomery et al., 2005; McDonnell et al., 2007). This summary focuses on the origin and characterization of the five geographic boundaries of the Fort Worth Basin (Figure 1) and includes a tectonic discussion as well.

The Fort Worth Basin is one of several Late Paleozoic structural and depositional features developed in conjunction with the Ouachita fold-belt on the southern margin of North America (Flawn, 1961).The basin is north-south-elongated and occupies approximately 15,000 mi^2 (38,100 km^2) in North-Central Texas (Montgomery et al., 2005). It has an asymmetrical wedge-shaped regional feature, and its thickest strata (more than 12,000 ft. (4000m)) formed in the area of the Ouachita fold-belt (Turner, 1957).

The Ouachita structural belt, which originated from the collision of Laurussia and Gondwana, resulted from successive orogenic events beginning in the Late Mississippian (Walper and Rowett, 1972; Keller and Cebull, 1973; Morris, 1974; Graham et al., 1975; Briggs and Roeder, 1975; Walper, 1977). The Fort Worth Basin is one of several foreland basins that formed along the front of the growing and advancing structural belt (Walper,

1977, 1982). This structural belt, which outlines the eastern and southeastern boundary of the Fort Worth Basin, contains Mississippian and older deposits (Montgomery et al., 2005).

The Fort Worth Basin is bounded on the northeast by the Red River Arch and the Muenster Arch; the latter is composed of a series of northwest-southeast- trending, asymmetrical fault blocks (Henry, 1982) that played an important role in sediment input during Early and Middle Mississippian time (Flawn et al., 1961; Hoffman et al., 1973, 1974). Near the Red River Arch, the Barnett Formation thins to extinction because of erosion along the southern flank of the arch (White, 1948). Flawn et al. (1961) stated that the Muenster Arch became active in Late Mississippian time and then emerged during Early and Middle Pennsylvanian time, shedding arkosic clastics to the southwest and northwest of the basin. This process made the Muenster Arch a potential source of siliciclastic sediments. This resulted from the Muenster Arch having been part of the remnant of an Early Paleozoic Southern Oklahoma Aulacogen (Hoffman, 1973, Walper 1977, 1982). This aulacogen occupied zones of vertical structural weakness that could be easily reactivated by subsequent tectonic events (Hoffman et al., 1974). In this case, Ouachita compression was triggered by the collision of Laurussia and Gondwana (Henry, 1982; Walper 1982).

The Llano Uplift marks the southern boundary of the basin. This domal-featured uplift acted as a firm buttress against the forces of the Ouachita Orogeny while having undergone intermittent positive movements since Precambrian time (Flawn, et al., 1961). Precambrian and Paleozoic rocks are exposed on the surface in the Llano Uplift in Central Texas (Flippin, 1982).

Westward, the basin is bounded by the Bend Arch, which extends northward from the Llano Uplift. It is a broad and gentle swell that formed in the late stages of the basin's evolution. The Bend is derived from a series of hinge lines composing the western boundary of the basin (Walper, 1982). The Barnett Formation thins rapidly against the eastern flank of the Bend Arch and is locally absent over the crest of the arch (Henry, 1982).

STRATIGRAPHIC RELATIONSHIP OF BARNETT FORMATION

The name Barnett (Figure 2) was first presented by Plummer and Moore (1922), who were working on outcrops in San Saba County. The Barnett Formation was deposited from Osagean to Chesterian age during a second-order, sea level highstand (345-320 Ma) (Ross and Ross, 1987), and continued accumulating sediments until the beginning of Pennsylvanian time, as suggested by conodont correlation (Merrill, 1980; Kier, 1980; Orth et al., 1986). Although the contact relationship is debatable (some thin detrital layers occurs in between, as will be discussed later), most geologists believe that the Barnett Formation is conformably overlain by the Pennsylvanian Marble Falls Limestone (Oden, 1958; Kuich, 1964; Turner 1970; Henry, 1982). It is underlain by lower Osagean Chappel Limestone on the southwest. Along the cross section northeast of the basin, the Chappel limestone tends to pinch out, and the Barnett is in unconformable contact with the Lower Ordovician Ellenburger group and the Upper Ordovician Viola - Simpson group respectively. In most of the basin, the Barnett strata rest on a major unconformity that spans 100 m.y. (Henry,

1982; Loucks and Ruppel, 2007). On the northern part of the basin, a limestone unit, the Forestburg, separates the Barnett Formation into upper and lower parts (Figure 2).

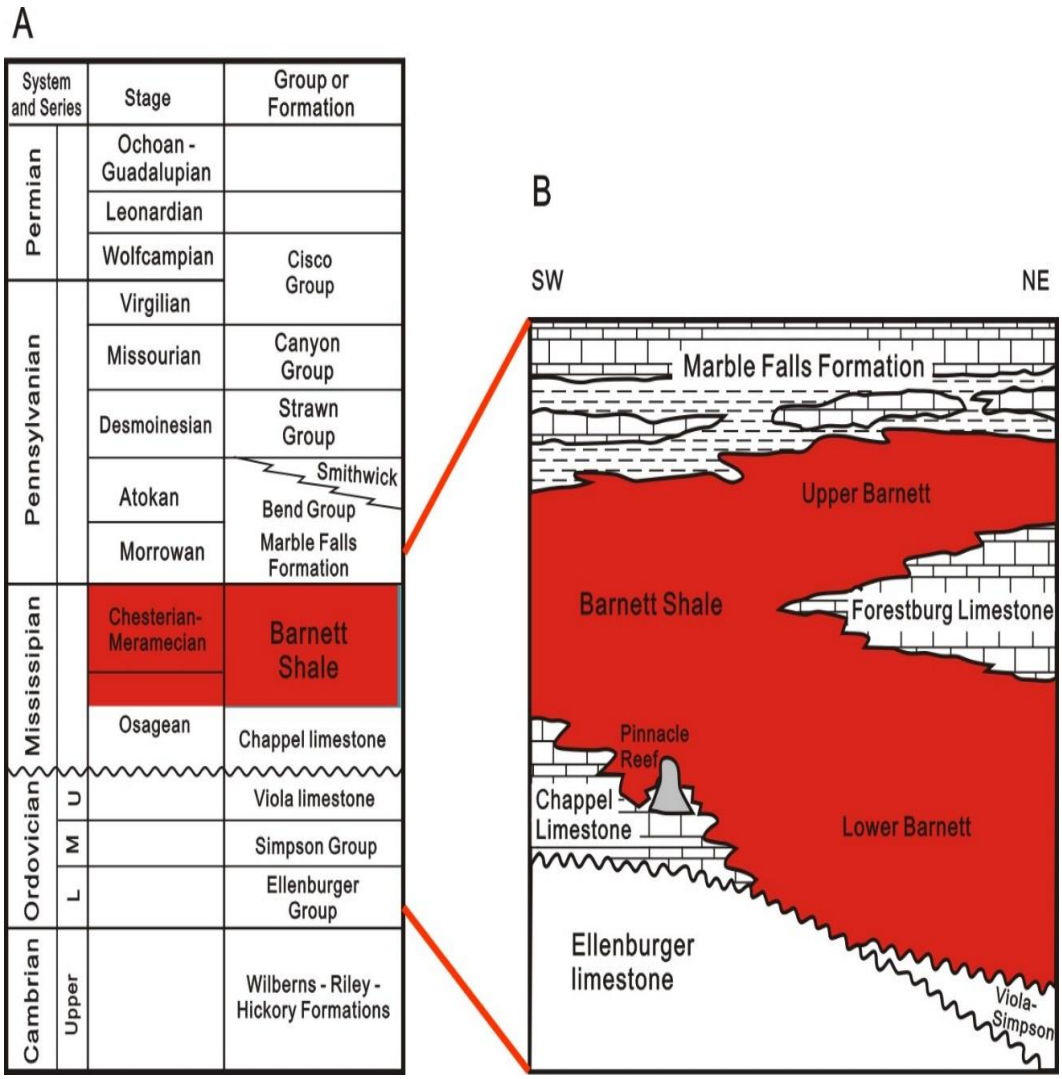

Figure 2: General stratigraphic relationship of the Barnett Formation and the overlying and underlying formations. A) Fort Worth Basin stratigraphy. B) Barnett Formation stratigraphy. Modified from Montgomery et al. (2005).

PALEOGEOGRAPHY

During Early Mississippian time when the Barnett Formation began to accumulate, the two continents, Laurussia and Gondwana, were far apart (Figure 3A). In between, a narrow ocean gateway connected the oceans on the west and east. Most of the land of North America today was submerged. During the Late Mississippian (Figure 3B) Laurussia and Gondwana were rapidly approaching each other, which accelerated the formation of a series of foreland basins near the Ouachita fold-belt. The formation of the Appalachian highlands shut down the gateway (Gutschick and Sandberg, 1983), which may have restricted the circulation of seawater and therefore probably accounts for the later occurrence of anoxia (Loucks and Ruppel, 2007). Evidence from Hamilton cores indicates that there is relatively high organic matter content throughout the deposition of the Barnett Formation in southeastern Fort Worth Basin, suggesting that the depositional settings were very stable in terms of low oxygen levels (anoxic) and deeper water depths.

The water depth of Barnett Formation is very difficult to decipher precisely; several researchers have proposed different depth intervals (Byers, 1977; Yurewicz, 1977; Gutschick and Sandberg, 1983; Ross and Ross, 1987; Loucks and Ruppel, 2007). Both Yurewicz (1977) and Gutschick and Sandberg (1983) estimated the water depth by analogy with other similar basins, which lacks more direct evidence. Byers (1977) cited the good preservation of organic matter and sedimentary features in determining his estimate. Ross and Ross (1987) addressed this problem from the standpoint of sequences and energy

conditions. All of the results indicate a depth of about 150 m to 200 m (450 ft. to 600 ft.), which is well below the storm-wave base.

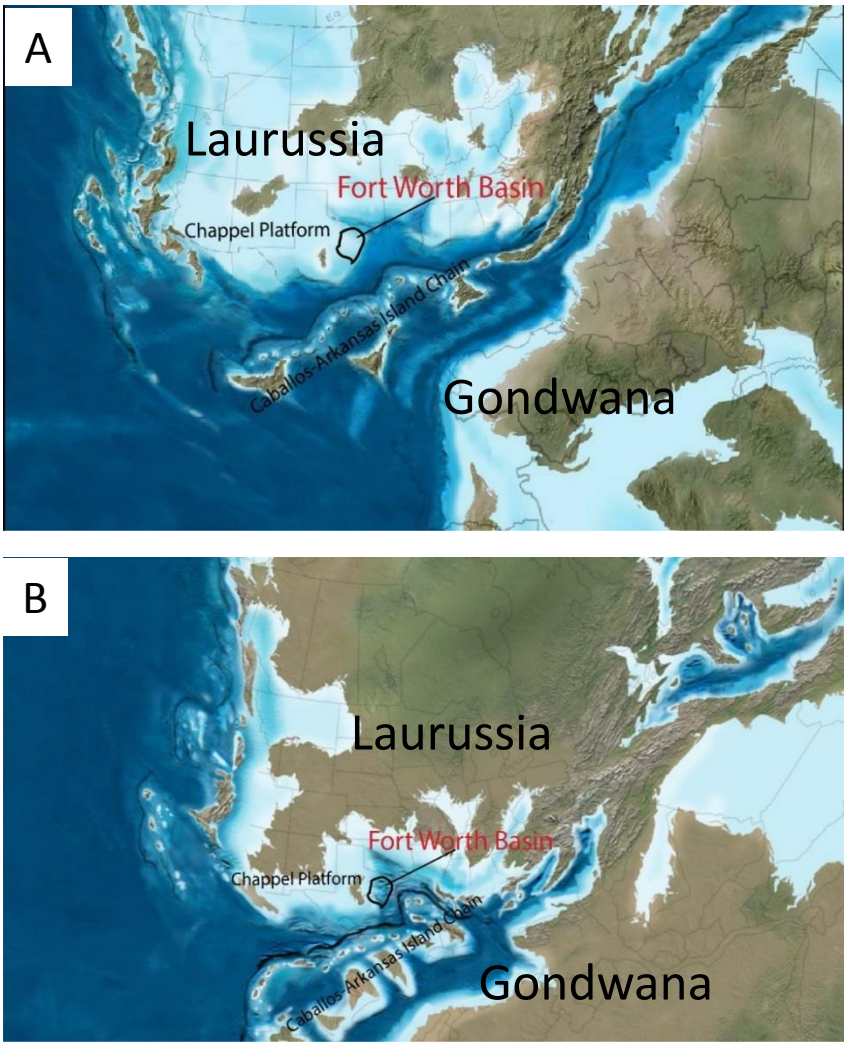

Figure 3: Paleogeographic maps. A) Paleogeographic map of the North American continent in Early Mississippian time (345 Ma) showing the location of Fort Worth Basin. B) Paleogeographic map of the North American continent in Late Mississippian time (325 Ma) showing the location of Fort Worth Basin. Modified from Blakey (2013).

SEDIMENTARY SOURCES

Two dominant sources may have supplied sediment to the Barnett Formation--- the Chappel platform and the Caballos-Arkansas Island Chain (Gutschick and Sandberg, 1983; Loucks and Ruppel, 2007) (Figure 4). Loucks and Ruppel (2007) thought that the Caballos-Arkansas island chain might be one important source for siliciclastic sediments because of the presence of silt-sized detrital quartz and feldspars. Subject to the collisions of continental plates on west, east and southeast, as well as to the transgression of the Early Mississippian sea (Yurewicz, 1977; Ruppel and Kerans, 1987), a large carbonate platform began to form around the transcontinental arch in Early Mississippian time (Lineback, 1969; Yurewicz, 1977; Gutschick and Sandberg, 1983). The Chappel limestone was deposited on the southeastern part of the large carbonate platform, and the Barnett Formation was deposited in the Fort Worth Basin, receiving sediments from the platform and slope in the form of hemipelagic plumes and gravity flows (Loucks and Ruppel, 2007). The Caballos-Arkansas Island Chain was also formed because of the Ouachita thrust fold-belt, where the collision of North and South American Continents produced a medial welt in the middle, where parts of the welt were emergent. Generally, the Fort Worth Basin was starved because neither the carbonate platform nor the island chain contributed much sediment to the basin (Gutschick and Sandberg, 1983). In addition, Barnett sediments may also have come from the Muenster Arch (Pollastro, 2003), which was reactivated by the continental collision. Both carbonate and terrigenous material could have been brought into the basin as shown by the interruption of Forestburg Limestone northeast of the basin, but

the influence of this source is weak in Hamilton County because of the great distance from these sources.

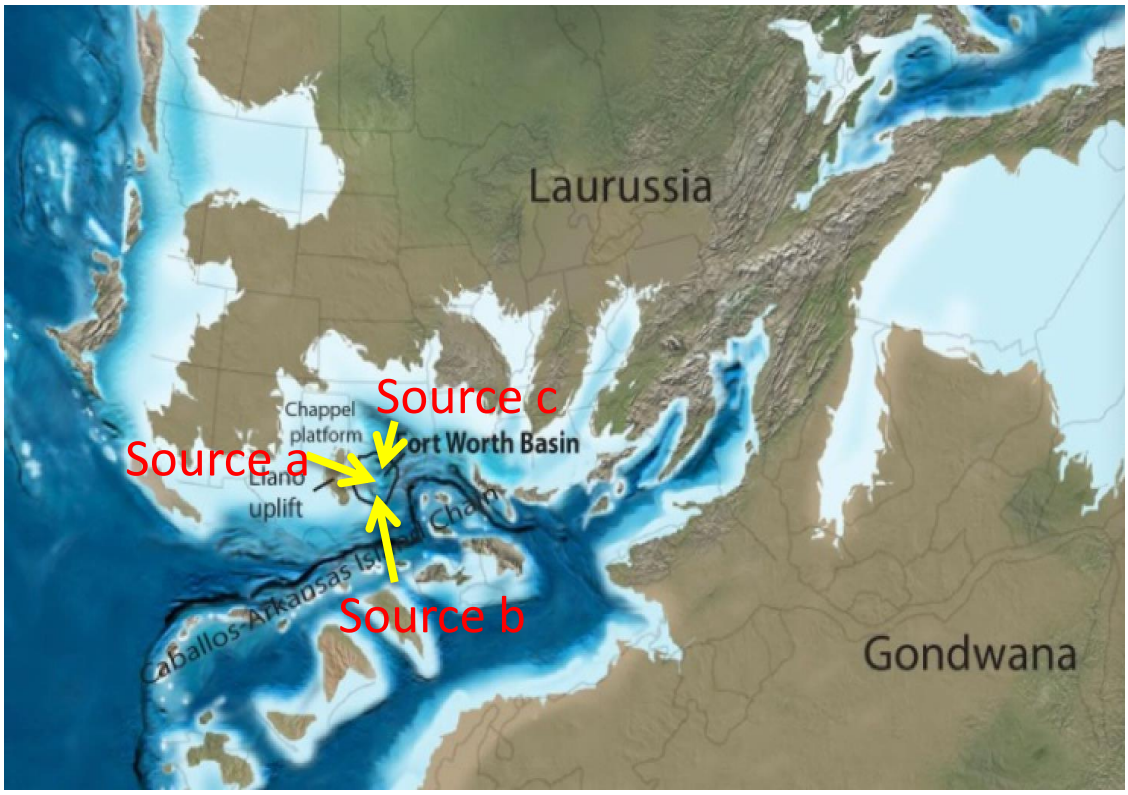

Figure 4: Possible source areas of sediment for the Barnett Formation in the Fort Worth Basin during the deposition of Barnett Formation. Source a: Chappel carbonate platform; Source b: Caballos-Arkansas Island Chain; Source c: Muenster Arch. Paleogeographic map from Blakey (2013).

BARNETT FORMATION IN HAMILTON COUNTY

The two cores used in this study (Mesquite No. 1 and Lake Davis No. 1, Hamilton County) are from exploration wells that never produced. The top and bottom of the Barnett Formation were confirmed by the combination of wireline log and core observations. Two marked peaks of natural gamma ray were identified from the Lake Davis No.1 (Figure 35). The top of Barnett Formation is right below the upper peak and the bottom is also right below the lower peak. The increase in gamma ray response is related to phosphate accumulation, which commonly has a high uranium composition (Baturin, 1982). For Mesquite No.1, the top and bottom were also confirmed respectively, but the increases are not obvious on the gamma ray curve. There are some thin formations between the Ellenburger, Barnett, and Marble Falls and evidence for their existence was obtained from core observation. For the gamma ray peak between Barnett and Ellenburger, the corresponding thin layer (3 to 4 inch thick) in core was informally named "Pennsylvanian detrital unit" (Robert Loucks, 2014, personal communication) which is characterized by a variety of lithology including dark-grey shales, abundant poorly sorted phosphatic grains as well as some sandstone, and the various phosphatic content account for the gamma ray peak above the Barnett (Wood, 2013). For the lower contact, the layer below Barnett is the remnant of Chappel cherty limestone, which is only for 2 to 3 feet, and is followed by a thin interval of Ives Breccia. The Ives Breccia is a regolith of eroded cherty carbonates and represents approximately a 100 million year hiatus (Watson, 1980, Loucks and Ruppel 2007).

A cross section from Denton County, located in the main producing area (adjacent to the Muenster Arch), to Hamilton County (Figure 5) was generated to show the changes in thicknesses and strata (Figure 6). As indicated from the cross section, the Barnett Formation is thicker in the northern Fort Worth Basin and is attenuated as it extends southward, which is consistent with the geometry of the Fort Worth Basin. The Barnett Formation in the northern producing area is approximately 800 ft. (270m) thick and buried as deep as 7000 to 8000 ft. (2300 to 2700 m); but in the Hamilton County study area, the Barnett interval in the two cores are only 138 ft. (46 m) and 167 ft. (56 m) thick and are buried much shallower at 3500 to 4500 ft. (1150 m to 1500 m). These differences are partly related to the geometry of the foreland basin, as the main producing area is closer to the fault blocks of the Muenster Arch, where the active remnant of Oklahoma Aulacogen created greater accommodation. The other reason is the deposition of Forestburgh Limestone, which separates the intact Barnett into Upper Barnett and Lower Barnett, both of which thicken the Barnett Formation. The two cores drilled in Hamilton County show the Barnett Formation in southwest Fort Worth Basin as one continuous section not separated by a similar carbonate unit.

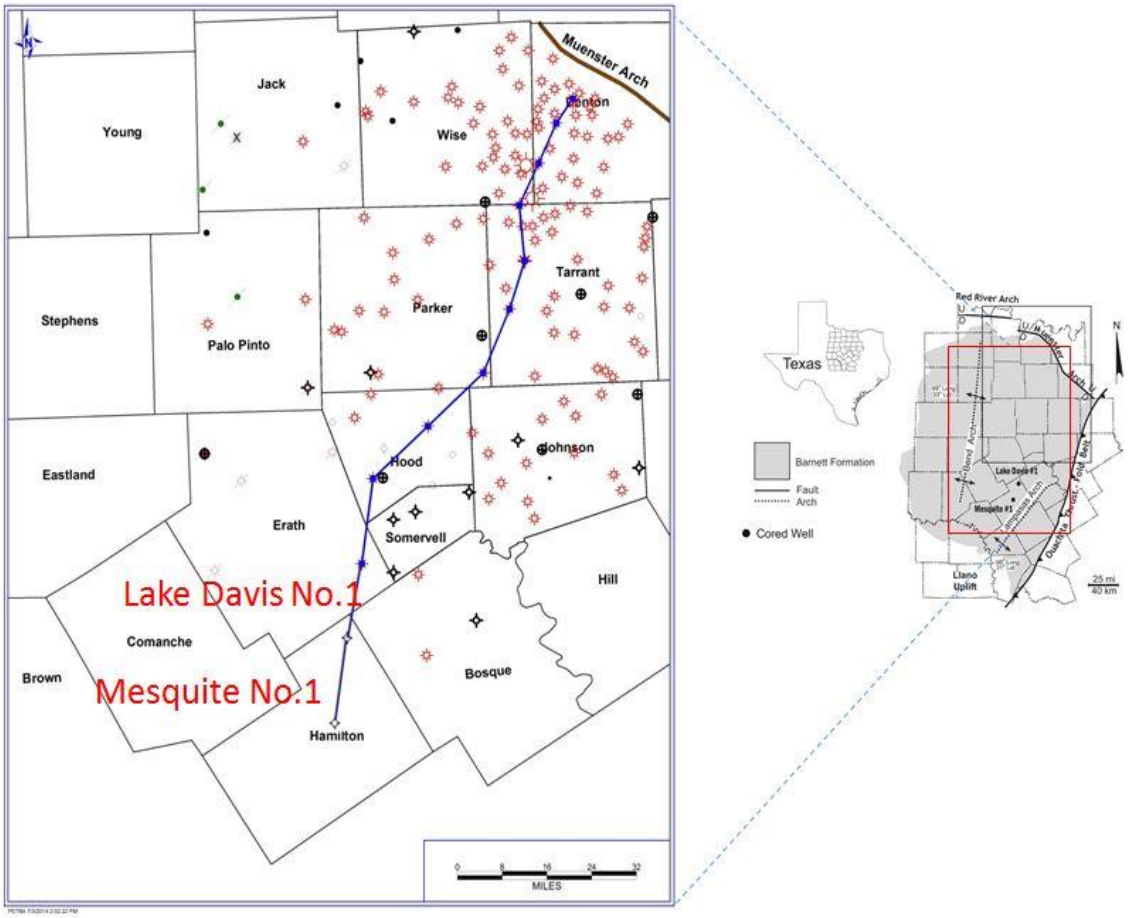

Figure 5: Line of section for the northeast-to-southeast cross section shown in Figure 6 from Denton County to Hamilton County. Wireline logs were provided by the Sloan Project of the Bureau of Economic Geology, UT Austin.

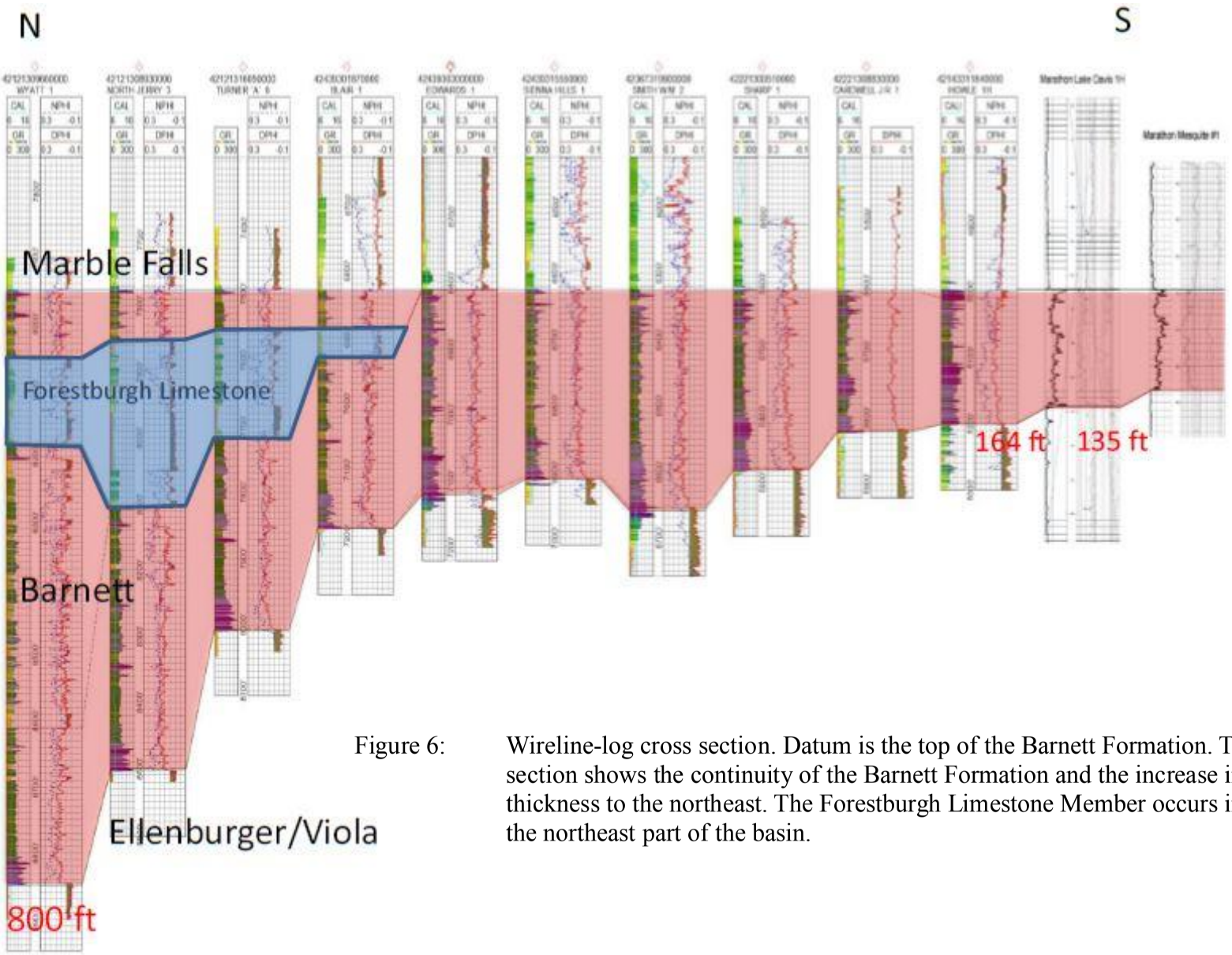

Figure 6: Wireline-log cross section. Datum is the top of the Barnett Formation. The section shows the continuity of the Barnett Formation and the increase in thickness to the northeast. The Forestburgh Limestone Member occurs in the northeast part of the basin.

METHODOLOGY

CORE AND WIRELINE-LOG STUDY

In this study, all the data were obtained from the two continuous cores drilled in wells in Hamilton County, Texas, by Marathon Oil Company: Mesquite No. 1 and Lake Davis No. 1 (Figure 5). The two cores were slabbed to observe their texture, fabric, and composition. Only the Lake Davis No.1 had the butt section of the core available, which can be used for different types of destructive sampling, including XRD, thin sections, and SEM samples. The Barnett interval of Mesquite No.1 covers the depth from 3690 to 3828 ft. The Barnett interval of Lake Davis No.1 covers the depth from 4073 to 4240 ft. The distance between the two cores is approximately 12.6 miles (20.3 kilometers). Wireline logs, including natural gamma ray and porosity, were taken with these two cores. In addition, CGR (K, Th) logs were generated by XRF-based elements in order to be correlated with a natural gamma-ray log and with lithofacies. Other wireline log data that were used in the cross section were provided by the Sloan Foundation Shale Gas Study, a project directed by the Bureau of Economic Geology.

XRF-BASED CHEMICAL DATA

The XRF data were collected by Dr. Harry Rowe (Bureau of Economic Geology, UT-Austin) using a Brüker Tracer III-V Energy-dispersed XRF instrument at the Bureau of Economic Geology in Austin, Texas. This device allows the investigator to acquire rapid and quantitative data from drill core without any destruction of the core (Rowe, 2012). The

cores in Hamilton County were sampled every 6 inches (15.2 cm) to ensure a good resolution. Measurements were made on both major elements (Mg, Al, Si, P, S, K, Ca, Ti, Mn, and Fe) and minor elements (Ba, V, Cr, Ni, Cu, Zn, Rb, Sr, Y, Zr, Nb, Mo, Th, and U). Samples were analyzed for major elements at 15 kv for 60 seconds; for minor elements, they were measured at 40 kv for 2 minutes. All the measured data were output into an Excel spreadsheet for future work. The unit for major elements was weight percent of the bulk rock; for minor elements, the unit is parts per million (ppm). The quantified results of major elements can represent the minerals in which these major elements predominate. Finally, XRF-based elements, logs, and gamma-ray curves were plotted with depth and correlated horizontally, in order to aid in the classification of lithofacies (Figure 7).

THIN-SECTION STUDY

On the basis of the core and XRF data, 54 samples were selected for thin sections. They were made by National Petrographic Services, Inc., in Houston. The thin sections were mounted on 46 x 27 mm glasses without epoxy impregnation due to the low porosity and tight pore system of the samples. Thin-section analysis was completed at the University of Texas at Austin using a Zeiss Axioskop 40 Polarizing Microscope. Photographs of the features seen under microscopy were taken using a Sony NEX-10 camera.

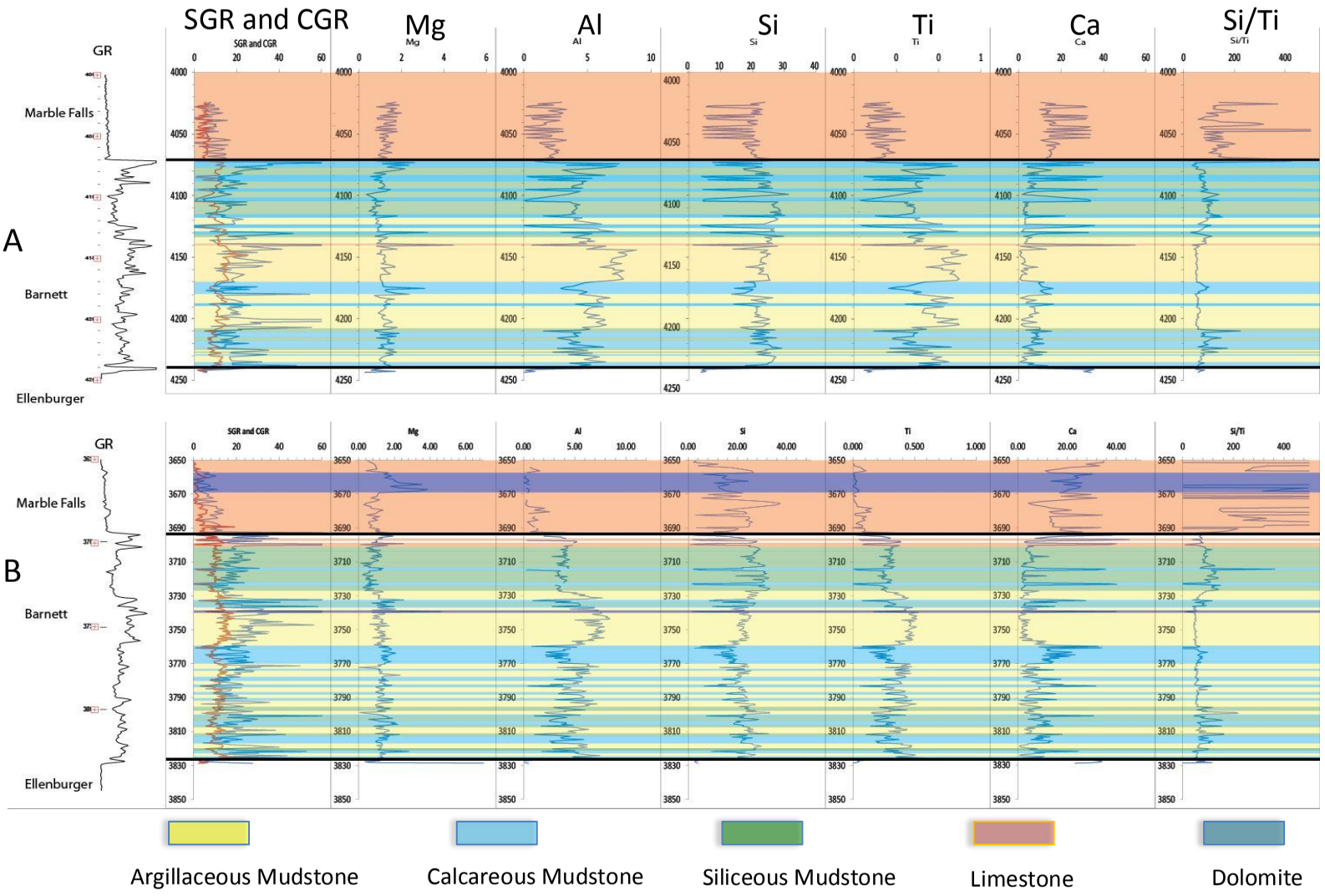

Figure 7: XRF geochemical data. A) XRF-based elemental log for the Lake Davis No. 1. B) XRF-based elemental log for the Mesquite No. 1.

CORE DESCRIPTION

More than 300 ft. (100 m) of the core was logged from the Barnett Formation (Figure 8). Cores were described with the aid of a binocular microscope and hand lens, and core observation was augmented by thin sections and XRF-based chemical data. A solution of 10% hydrochloric acid was dropped on the back of the core in order to estimate the general percentage of carbonate content and this was collaborated by the calcium measured XRF analysis.

Five lithofacies were defined. Four of them were classified according to Folk's mudrock classification (1980) and on the basis of their dominant mineral compositions. For the packstone to grainstone, it is classified according to Dunham's Classification (1962). Three types of matrix: argillaceous/clay-rich siliceous, siliceous and calcareous (their signatures on XRF are shown on Figure 9), which were interpreted according to the XRF-based and XRD-based data, were applied to define the five lithofacies as the most critical modifiers. For the other mineral modifiers, the closer to the rock name, the more important they are.

INORGANIC GEOCHEMISTRY

After facies classifications were made, more additional inorganic chemical analyses in terms of different facies were conducted. Different parameters were utilized, such as the cross plot of Si and Al, showing excess silica, and the plot of Degree of Pyritization of Total Iron (DOP_T) (Raiswell and Berner, 1986) to examine the silica content and paleoredox environment.

A. Mesquite No.1 B. Lake Davis No.1

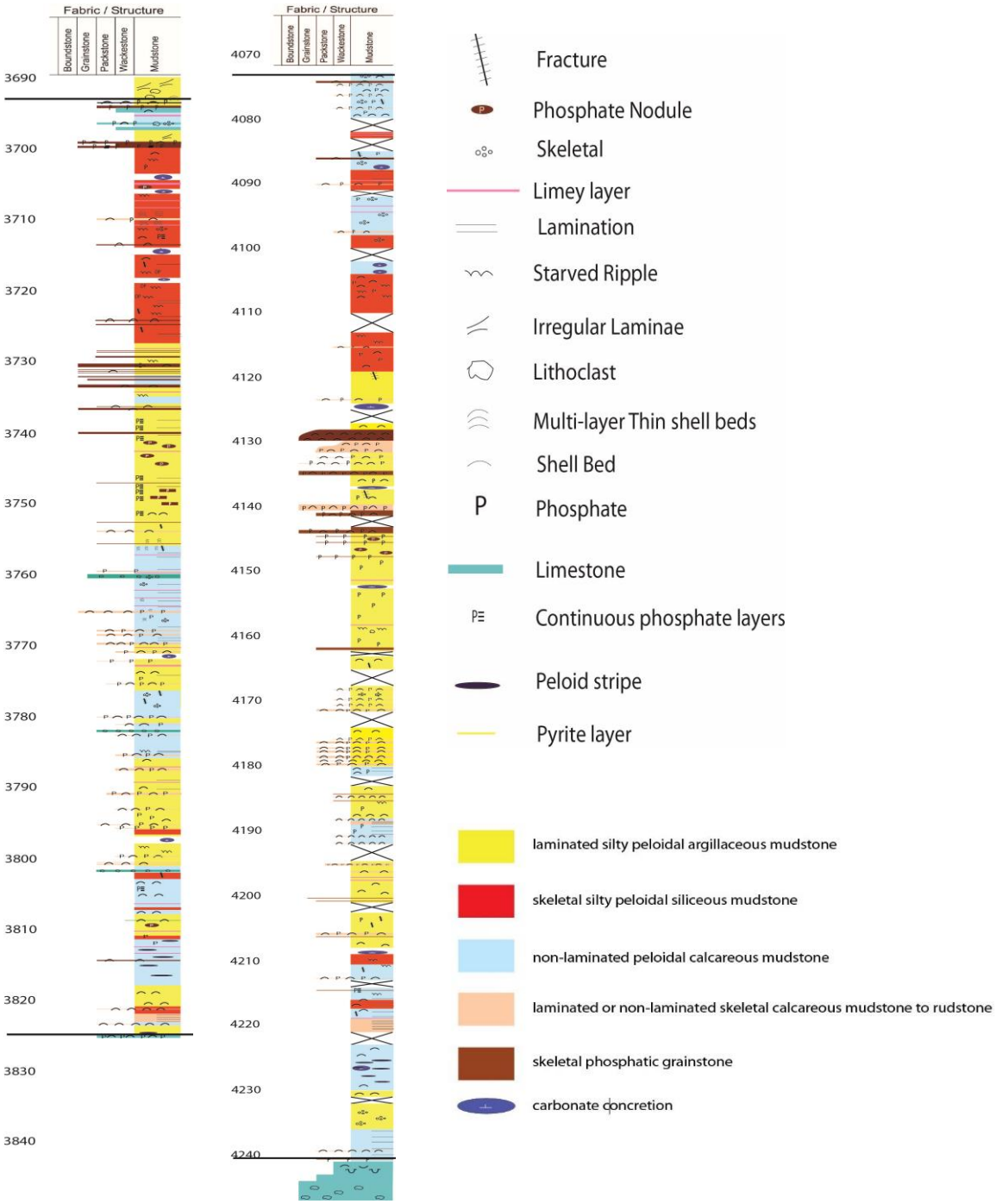

Figure 8: Core descriptions of Mesquite No. 1 and Lake Davis No. 1.

Cross Plot of Si% versus Al%

Detrital input is always a considerable factor to be evaluated because it can dilute the marine sediments and organic matter. In order to know the influence of detrital input, it is meaningful to cross-plot the elements with Al because Al is the crucial component within detrital clay, and it is fixed in the clays during diagenesis (Tribovillard et al., 1994; Potter et al., 2004; Tribovillard et al., 2006,). In this study, a cross-plot of %Si versus %Al (Figure 36) was generated to evaluate detrital influence (as will be explained in detail in Inorganic Chemistry Chapter). The "%Si-excess" parameter is calculated as the %Si difference between the measured %Si of a sample and the %Si versus %Al regression line (illite-silica line) for the argillaceous mudstone (Rowe, 2008).

Paleoredox: Molybdenum Content and DOP_T

Molybdenum (Mo) is widely used as a paleoredox indicator owing to its abundance in anoxic environment (e.g., Sternbeck, 2000; Rowe, 2008; Baldwin, 2014). In this study, the Mo content in Mesquite No.1 (Figure 37) was compared with the average content of Mo in gray shale (Wedepohl, 1971**)**. However, authors of recent studies have re-evaluated the use of Mo as a paleoredox proxy in restricted (silled) depositional environments and have suggested that Mo should be used in association with other parameters (Algeo, 2004; Algeo and Lyons, 2006).

Offering stability and abundance in marine anoxic conditions, pyrite-related parameters have been widely used as a proxy to identify paleoredox conditions (Raiswell et al., 1988; Lyons and Severmann, 2006). Among these parameters, degree of pyritization

(DOP), developed by Berner (1970), is the most commonly used. DOP is defined by the ratio of pyritized Fe (based on total sulfur) to the total amount of reactive Fe:

$$DOP = \%Fe\ pyrite / (\%Fe\ pyrite + \%Fe\ reactive) \quad (1)$$

DOP_T (Degree of Pyritization of Total Iron), proposed by Raiswell and Berner (1986), can be used as an approximated and reliable proxy for DOP. It is defined as pyritic iron over total iron (Raiswell and Berner, 1986), and the data are easier to obtain. Thus, DOP_T is applied in this study to infer primary redox conditions (Figure 38). Raiswell et al. (1988) have proposed that sediments with DOP of <0.46 indicate aerobic bottom water conditions; dysoxic or restricted conditions are implied by a DOP value of between 0.46 and 0.75, and a DOP of greater than 0.75 suggests euxinic conditions for the deposition of fine-grained sediments. Rowe (2008) suggested the weakness of this proxy, which is that where secondary pyrite exists in addition to primary pyrite, the combination of both may influence the accuracy of DOP_T.

ORGANIC GEOCHEMISTRY

Organic chemical analysis was also conducted on the two cores. In all, LECO TOC was analyzed for 273 samples of Barnett mudrock from the Mesquite No.1 well. In addition, existing hydrocarbon in the core (S1), hydrocarbon (mg per gram of rock) generated by thermal cracking (mg per gram of rock) (S2) and carbon dioxide (mg per gram of rock) (S3) as well as Tmax (^oC) were obtained by pyrolysis. The hydrogen index (HI) and oxygen index (OI) were calculated using the formulas (Peters 1986, 1994)

$$HI = S2 \times 100/TOC \quad (2)$$

$$OI = S3 \times 100/TOC \quad (3)$$

HI and OI are used in the identification of kerogen types (Figure 41). Since only a few samples have measured vitrinite reflectance, calculated vitrinite reflectance values were obtained to observe maturity:

$$\text{Cal. \% Ro} = 0.0180 \times Tmax - 7.16 \text{ (Jarvie et al., 2001)} \quad (4)$$

Dembicki's (2009) scheme was also applied to classify kerogen quality by plotting TOC using S2 only, as well as with S1+S2 (Figure 43).

XRD STUDY

Twenty-four samples were drilled from the Lake Davis No.1 well, and the collected fine-powder (10-15um) samples were scanned with a Bruker AXS D4 Endeavor x-ray diffractometer using copper K-alpha radiation at standard scanning parameters. All of the cores were measured for approximately 7 minutes. Then the resulting patterns of each sample were analyzed using XPowder software (A product of Bruker Corp.) by which diffraction peaks can be detected and matched with the mineral based on the mineral database PDF2.

SEM STUDY

Four samples with various porosities were selected from Lake Davis No.1 for SEM-scale pore observation. The samples were prepared using broad beam Ar ion-milling techniques (Reed and Loucks, 2007; Loucks et al., 2009). This method does well in controlling topographic irregularities when the samples have differences in hardness (Loucks et al., 2009, 2012). Artifacts related to this method during preparation are easily

discovered. Then the samples were observed under an FEI Nova NanoSEM 430 at the University of Texas at Austin. The observed pores were classified using the classification proposed by Loucks et al. (2012).

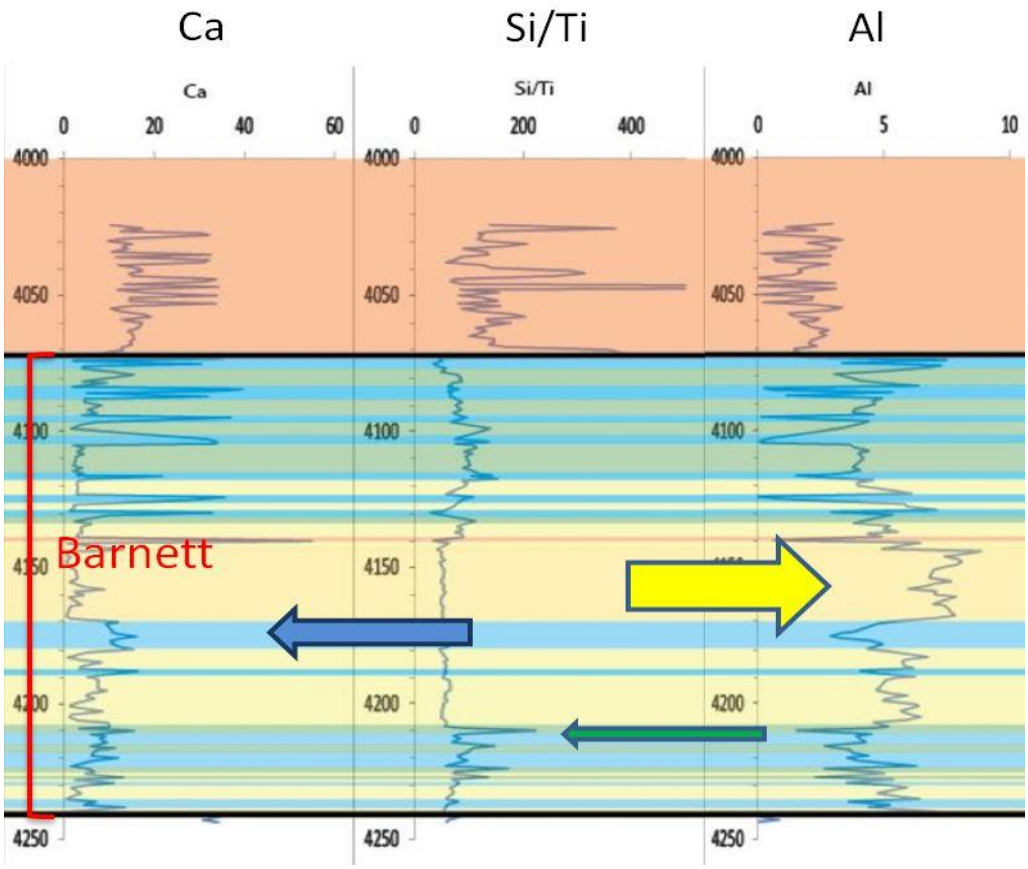

Figure 9: Three end-members of matrix were identified using the XRF-based chemical data. The yellow arrow points to argillaceous/clay-rich siliceous mudstone; the blue arrow points to calcareous mudstone; and the green arrow points to a siliceous peak indicating a siliceous mudstone.

MINERALOGY

INTRODUCTION

The mineralogy of the Barnett Formation is diverse. A ternary diagram plotted according to XRD analysis (Figure 10) shows relative proportion of carbonate minerals, clay minerals, and other minerals (mainly quartz, feldspar, pyrite and phosphate). The relative proportions of the three minerals have an influence on the Young's Modulus and Poisson's ratio (Lowrie, 2007) and will affect the performance of hydraulic fracturing. Generally, most of the samples have a clay content less than 30%; the skeletal-rich mudstones and calcareous mudstones have the lowest clay content and highest carbonate content. Most of the siliceous mudstones have a carbonate content of less than 20%. The important signature of low clay and high quartz content is favorable for fracturing (e.g. Matthews et al., 2007). An EDAX map displays the distribution of mineral components and organic matter (Figure 11). Microscopically the mineralogy of Barnett can be divided into extrabasinal and intrabasinal minerals.

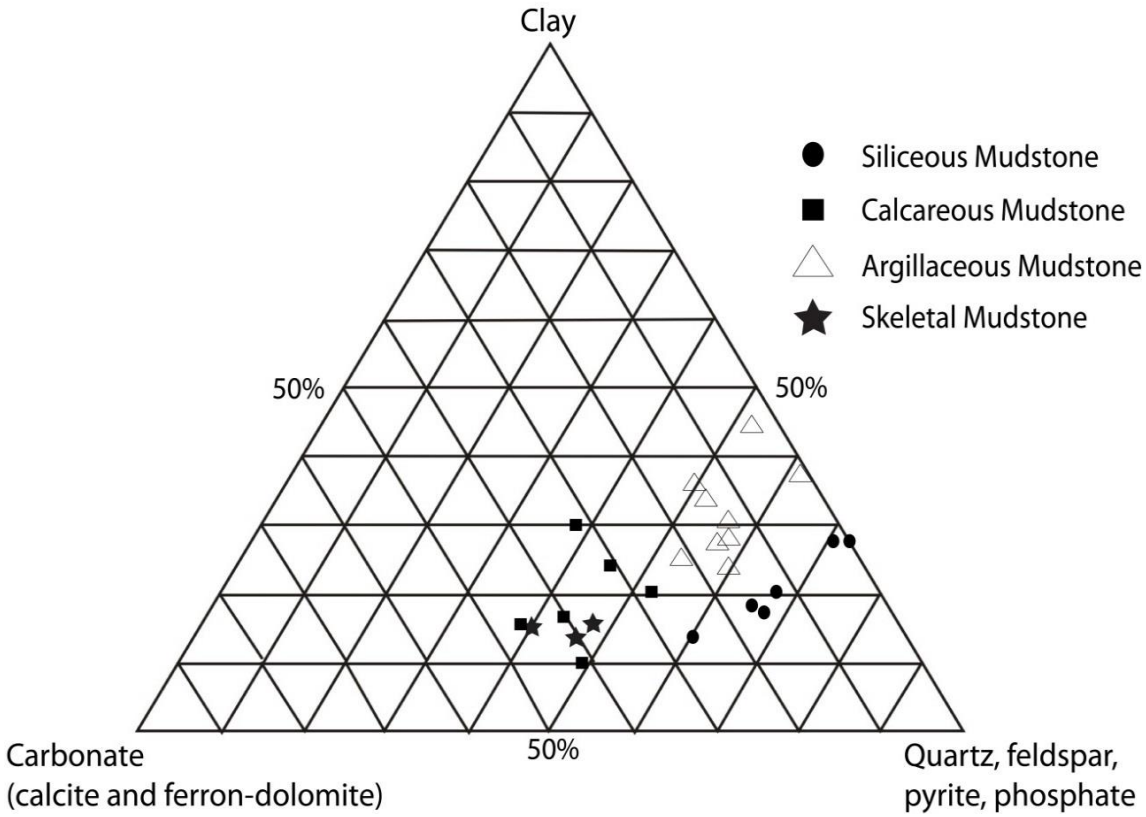

Figure 10: Compositional ternary plot showing mineralogy. Based on XRD data.

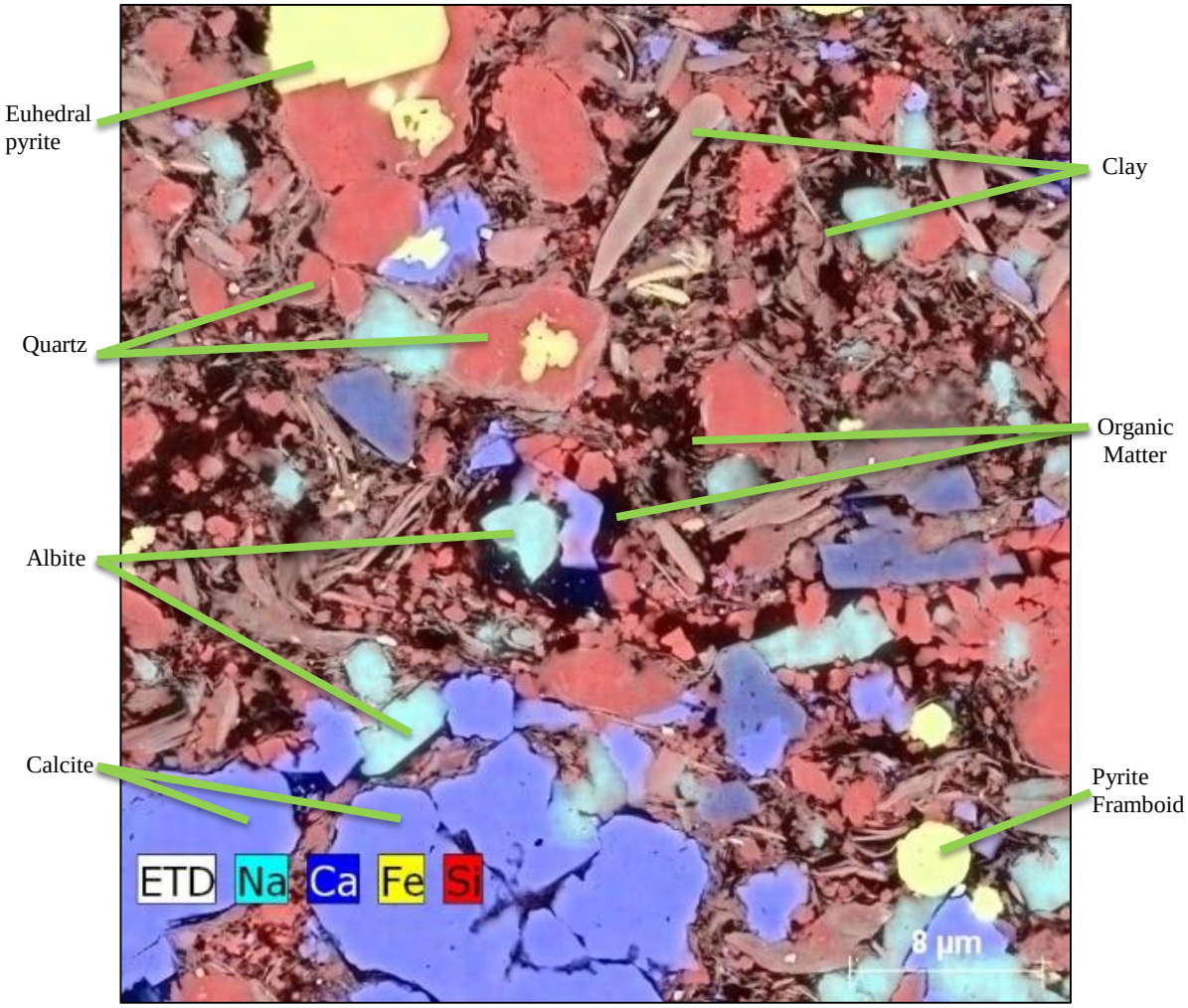

Figure 11: Combination of SEM photomicrograph and EDAX map showing an example of the grain types in the Barnett Formation. Lake Davis No. 1, 4189 ft.

EXTRABASINAL PARTICLES

A common component of the Barnett Formation is detrital particles. Detrital quartz is the most abundant extrabasinal particle in the Barnett (Papazis, 2005). These particles can be recognized by optical microscopy as extrabasinal detritus by their angular monocrystals (Milliken, 1994). They are mostly subangular to angular with fine-silt size with small inclusions (Figure 12). Generally, the abundance of detritus does not affect the classification of lithofacies because a similar amount of detritus occurs in all the studied lithofacies. Bunting (2007) assumed that the detrital quartz was induced into the water column by wind. Locally horizontal variation in abundance can be observed, which was probably caused by bottom current reworking. It is difficult to differentiate feldspars and quartz grains under the microscope because of their small size. Albite is recognized by its high sodium content as noted using EDAX analysis (Figure 11). Other feldspar grains such as K-feldspar and Ca-plagioclase are rare in the Barnett (Papazis, 2005).

Wood fragments, Type III organics, (Figure 13) was observed in core and thin section. It is commonly larger than 0.1 cm and is black. As seen under the microscope they show a well-preserved cellular structure.

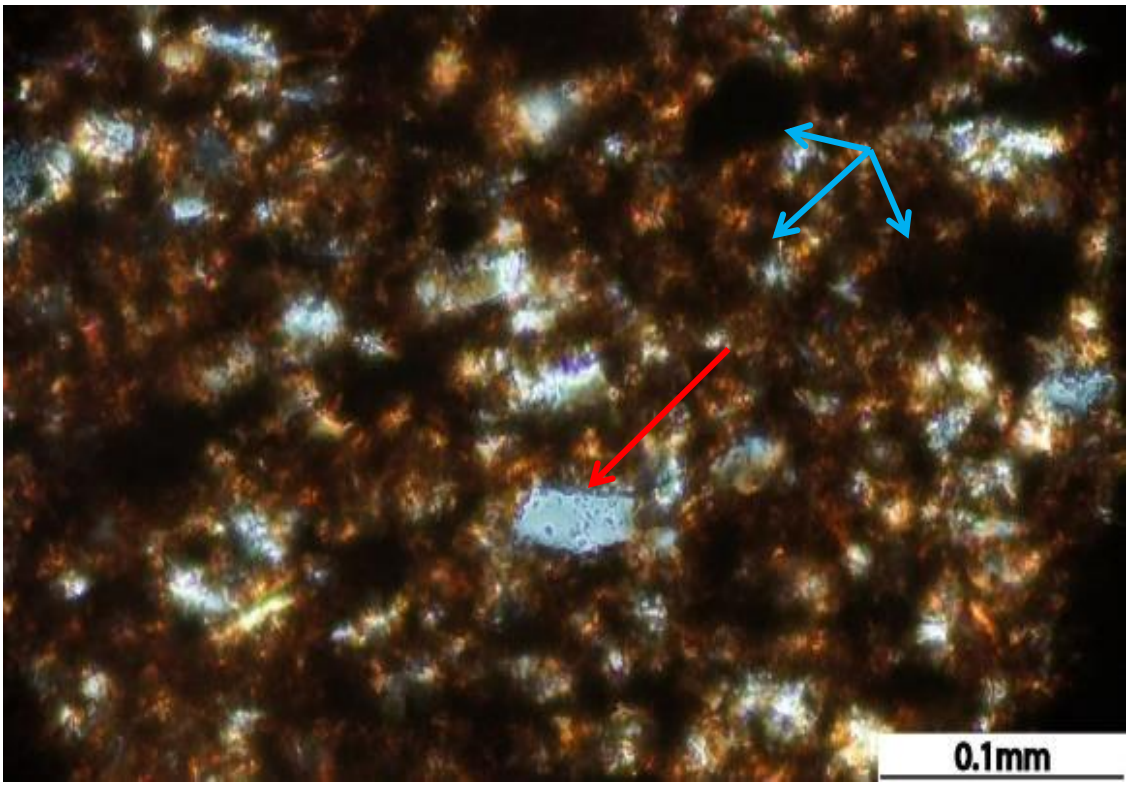

Figure 12: Detrital quartz silt (red arrow) in a peloid-rich matrix (blue arrows). Lake Davis No. 1, 4081.8 ft.

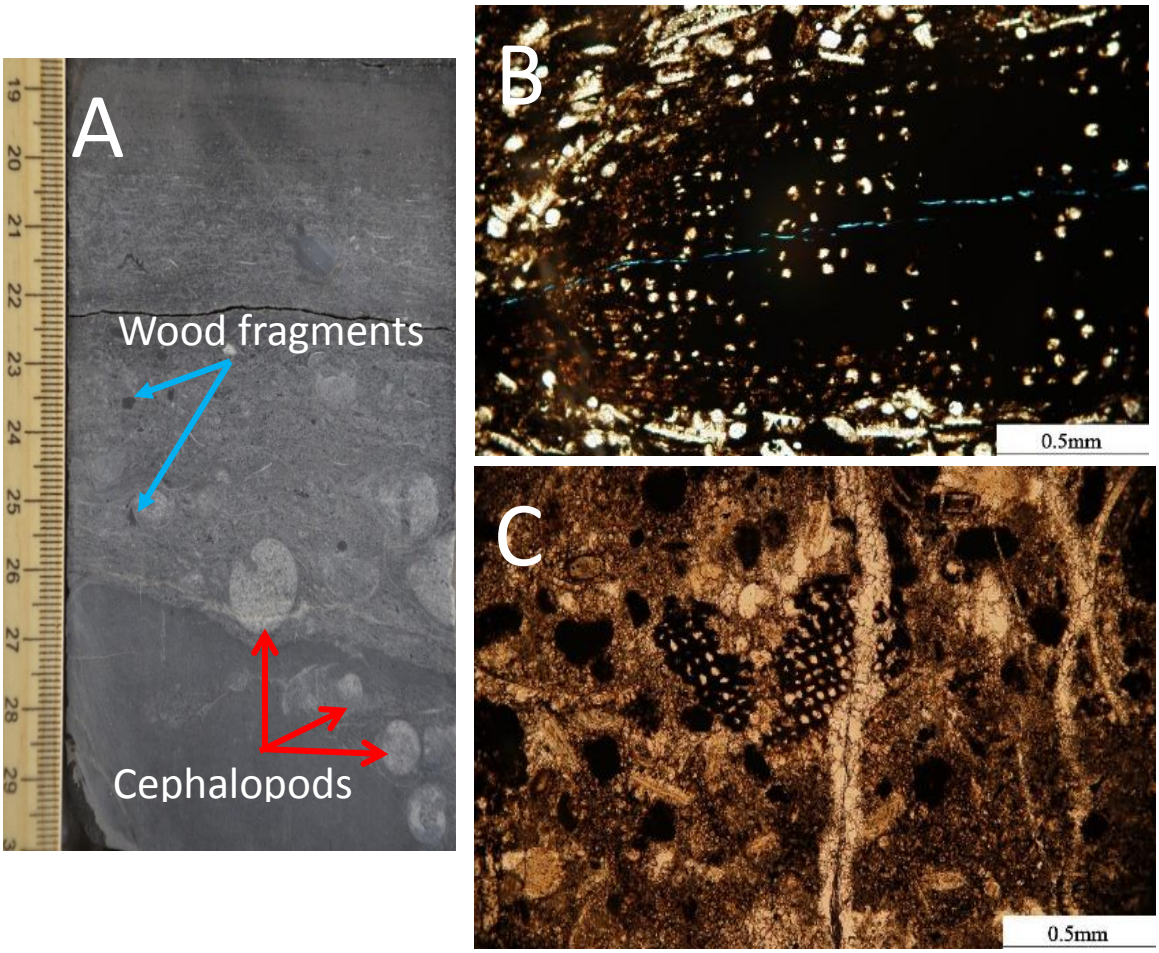

Figure 13: A) Wood fragments as seen in core (blue arrows). Mesquite No. 1, 3696.8 ft. Scale in centimeters. B) Woody material showing cellular structure. Lake Davis No. 1, 4078.5 ft. C) Fragments of woody material. Lake Davis No. 1, 4095.2 ft.

INTRABASINAL PARTICLES

Authigenic Quartz

Quartz is the most abundant authigenic mineral in the Barnett mudstones. In this study, cathodoluminescence work was not performed, but authigenic phases can be distinguished from detrital quartz by cathodoluminescence according to Papazis and Milliken (2005). In the Barnett, the materials for authigenic quartz come from many sources. Since the clay minerals in Barnett mudstones are dominated by illite and a small amount smectite (Bowker 2002), the most important source is thought to have been the transformation of smectite to illite, during which large amount of silica and pore water were released with increasing temperature in diagenesis (e.g., Boles and Franks, 1979; Lynch, 1997). The dissolution of the abundant silica-producing biota such as radiolarians and sponge spicules also contributed to the authigenic quartz. In addition, the dissolution of very fine quartz may also provide material for the formation of authigenic quartz. Unlike the detrital quartz, authigenic quartz exists in matrix, and it is difficult to differentiate under a microscope. SEM revealed authigenic quartz replacement within a shell fragment. (Figure 14)

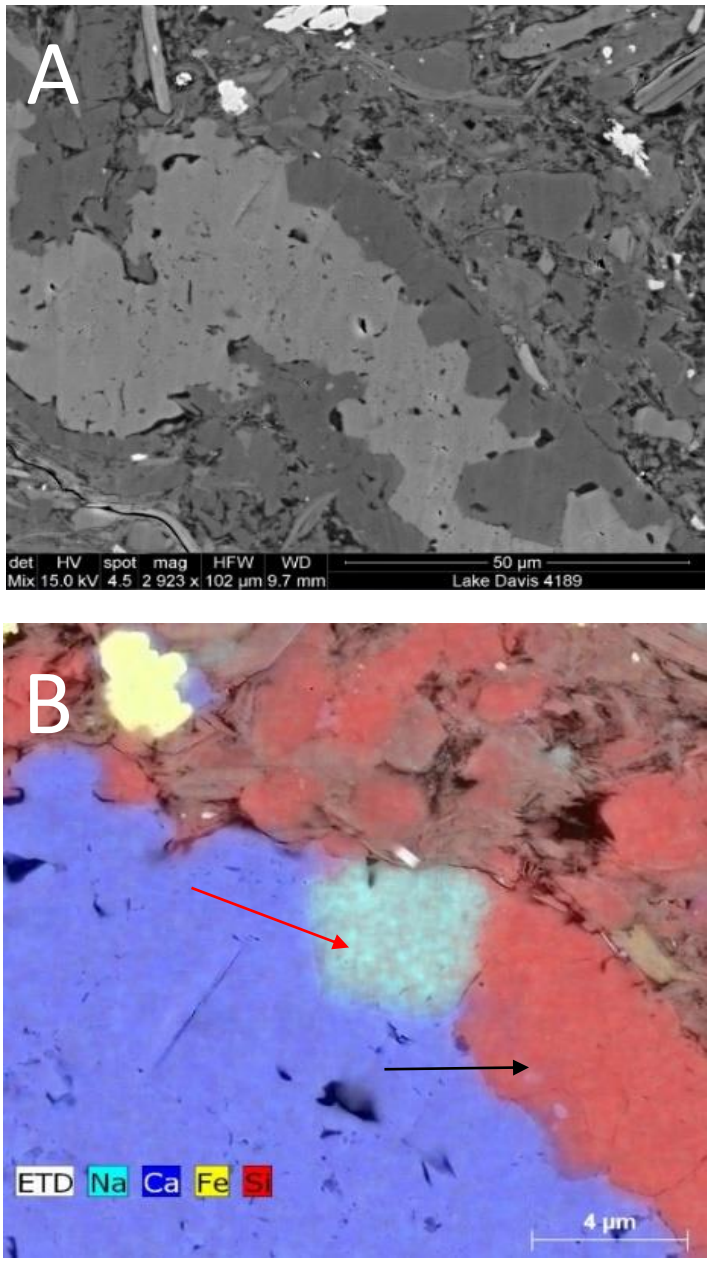

Figure 14: Authigenic Quartz. A) Bivalve fragment with rim replaced by authigenic quartz and albite. Lake Davis No. 1, 4189 ft. B) Close-up of the bivalve fragment produced by SEM microphotograph and EDAX map. The original calcite shell (blue) is in part replaced by authigenic albite (red arrow) and authigenic quartz (black arrow). Lake Davis No. 1, 4189 ft.

Calcite

In the Barnett mudstones, calcite is also an important authigenic mineral as also noted by Papazis (2005). Calcite occurs as concretions, fracture fills, and bivalves-related calcite.

Calcite Concretion

Calcite concretions in mudstones and shales are thought to be form early just beneath the sediment surface and lithify before compaction of the adjacent sediment (e.g., Weeks, 1957; Raiswell, 1971; Selles-Martinez; 1996; Loucks and Ruppel; 2007). Evidence of compaction of adjacent sediment was noted around the concretions (Figure 15J) where fine-grained materials are aligned. Toward the center of the concretion, the texture is uncompacted because of early lithification. Pellets and peloids retain their original rounded shapes. The evidence illustrates that 1) early lithification preserved the original texture and fabric; and 2) cementation began at the center of the concretion and progressed outward.

Three types of concretions with different features were identified (Figure 15). The first type of concretion is clay-rich. It is composed of calcite pseudospar (15-20 micrometers in diameter). Clay minerals and organic matters are abundant and account for 20-30% of the whole rock. The clays form thin seams that separate carbonate materials into individual grains and clusters (Figure 15A). Calcite cements are patchy and disseminated in the concretion. Radiolarians are abundant in these concretions. Most of the radiolarians are replaced by equant calcite (Figure 15B). The internal structures are unrecognizable

because medullary shells within the tests were dissolved. Bladed calcite cement precipitated on some of the small skeletal fragments (Figure 15D).

The second type of concretion consists predominantly of calcite pseudospar that ranges from 15 micrometers to more than 30 micrometers. Clay minerals are not abundant enough to separate carbonate particles compared with the first type of concretion (Figure 15E). Calcite precipitation in this concretion type is much more apparent, showing larger, euhedral sparry calcite crystals. Dark peloids are disseminated within the calcareous matrix. Some of the peloids show a micritic texture. In some cases, clear boundaries can be recognized between the first and second type because of the different level of cementation in the two beds (Figure 15F). Fossils are extremely rare or indistinct; only a few radiolarians were observed in the second type.

The third type of concretion is also dominated by dark gray micritic material and pseudospar, similar to the second type (Figure 15G). The difference is that small pyrite framboids or crystals were uniformly distributed within the calcareous matrix. The most remarkable feature in this concretion type is the occurrence of a pyritic zone containing isolated pyrite crystals around the outer rim of the concretion (Figures 15H). Unlike the isolated pyrite in the matrix, which are in a size range of less than 5 micrometers, the pyrite within the rim are mixed with well-developed euhedral pyrite that vary in crystal size from 5 micrometers to 200 micrometers (Figure 15I). Overgrowths may appear on both large and small pyrite crystals. The similar zonation of pyrite was also recognized by Papazis (2005) and Milliken et al. (2012). Closer to the rim of the concretion beyond the pyritic zone, more clay minerals or organic material are present, and an increase of compaction

appears gradually. The transition from the concretion to the overlying and underlying mud was gradational and the amount of fine-grained material increases, which may result from the gradual changes in composition of pore-water through time (Figure 15J).

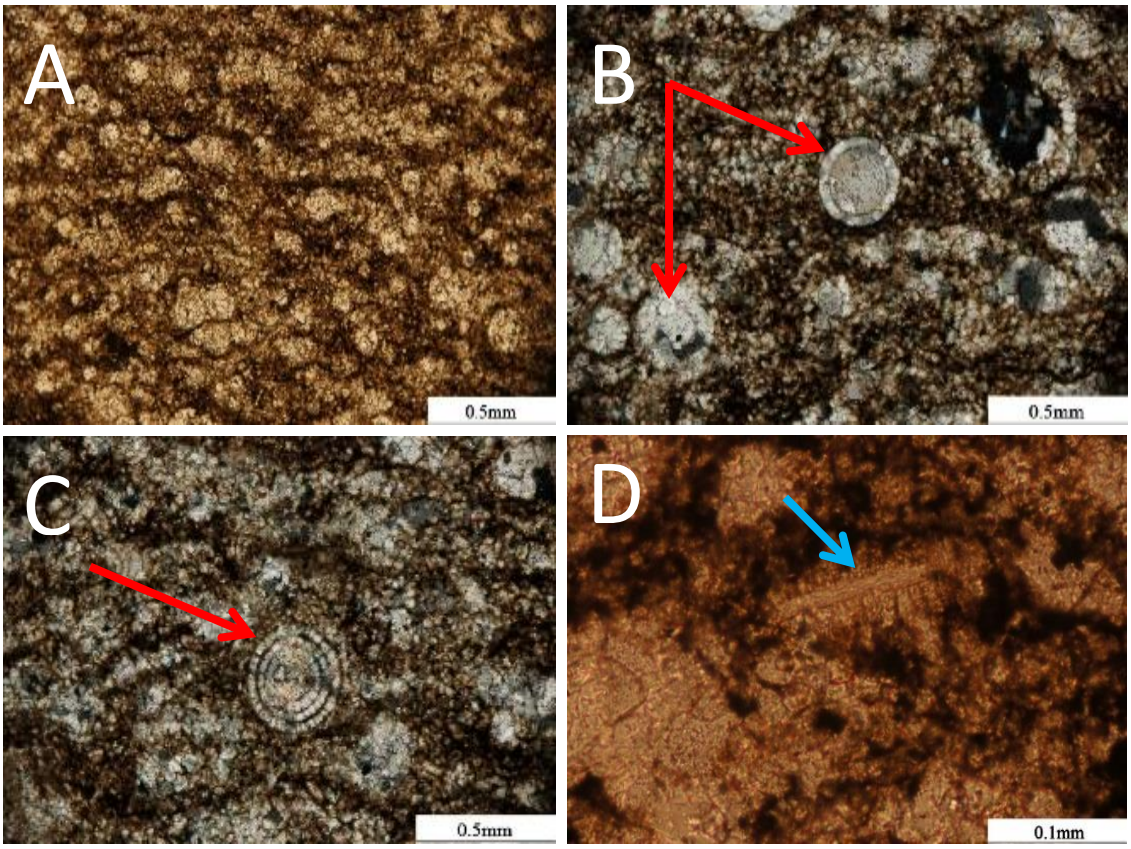

Figure 15: Calcite concretions. A-D: Type I A) Concretion with radiolarians and pseudospar as well as abundant clay seams that separate grains into individual grains or clusters. Lake Davis No. 1, 4104.1 ft. B) Calcified radiolarians (red arrows) replaced by equant calcite. Lake Davis No. 1, 4104.1 ft. Photomicrograph taken with polarized light. C) Calcified radiolarian with medullary shells (red arrow). Lake Davis No. 1, 4104.1 ft. Photomicrograph taken with polarized light. D) Thin-walled bivalve fragments with blading cement (blue arrow). Lake Davis No. 1, 4104.1 ft.

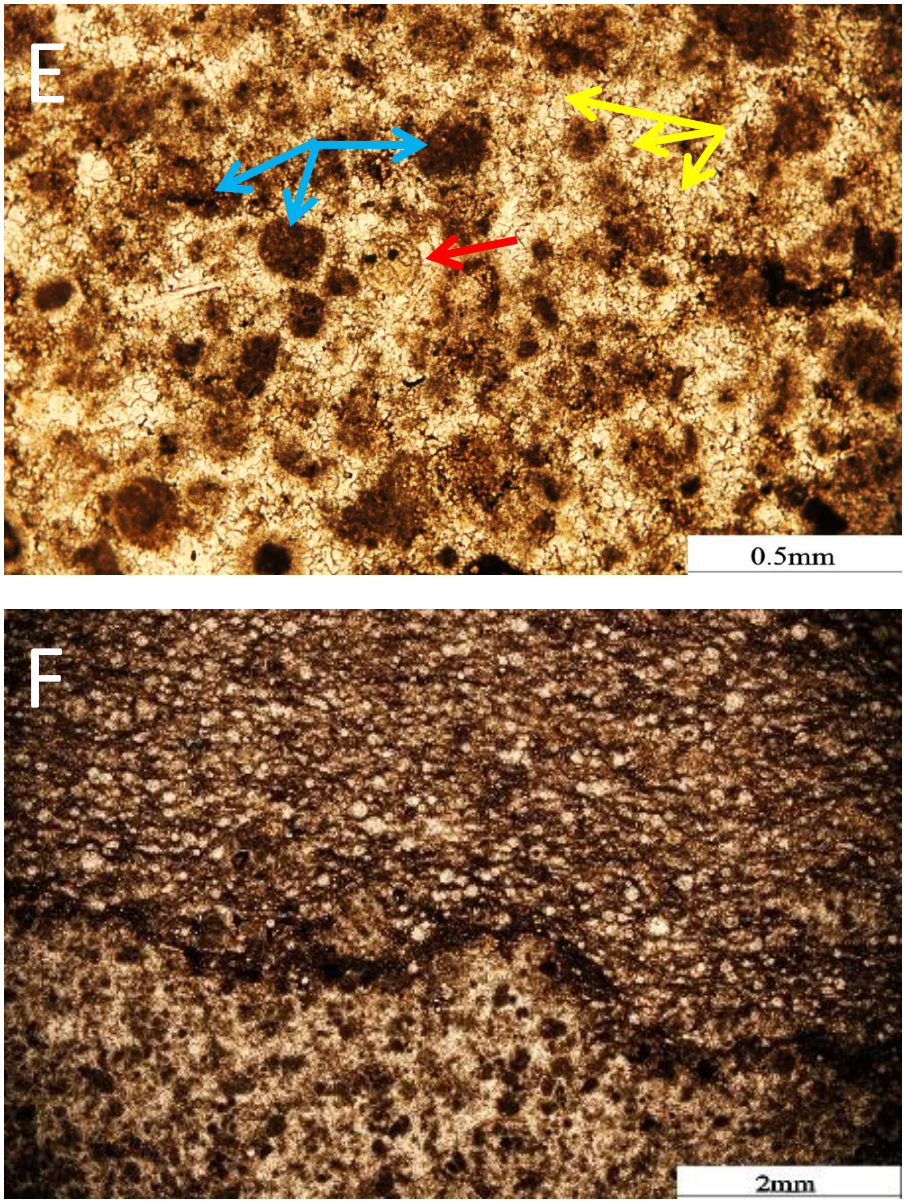

Figure 15: (continued). Calcite Concretion Type II. E) Concretion containing pseudospar cement (yellow arrows), uncompacted peloids (blue arrows), radiolarian (red arrow), and bioclastic material. Lake Davis No. 1, 4104.2 ft. F) Contact separating two types of concretion that have different amounts of cement and clay. Lake Davis No. 1, 4140.2 ft.

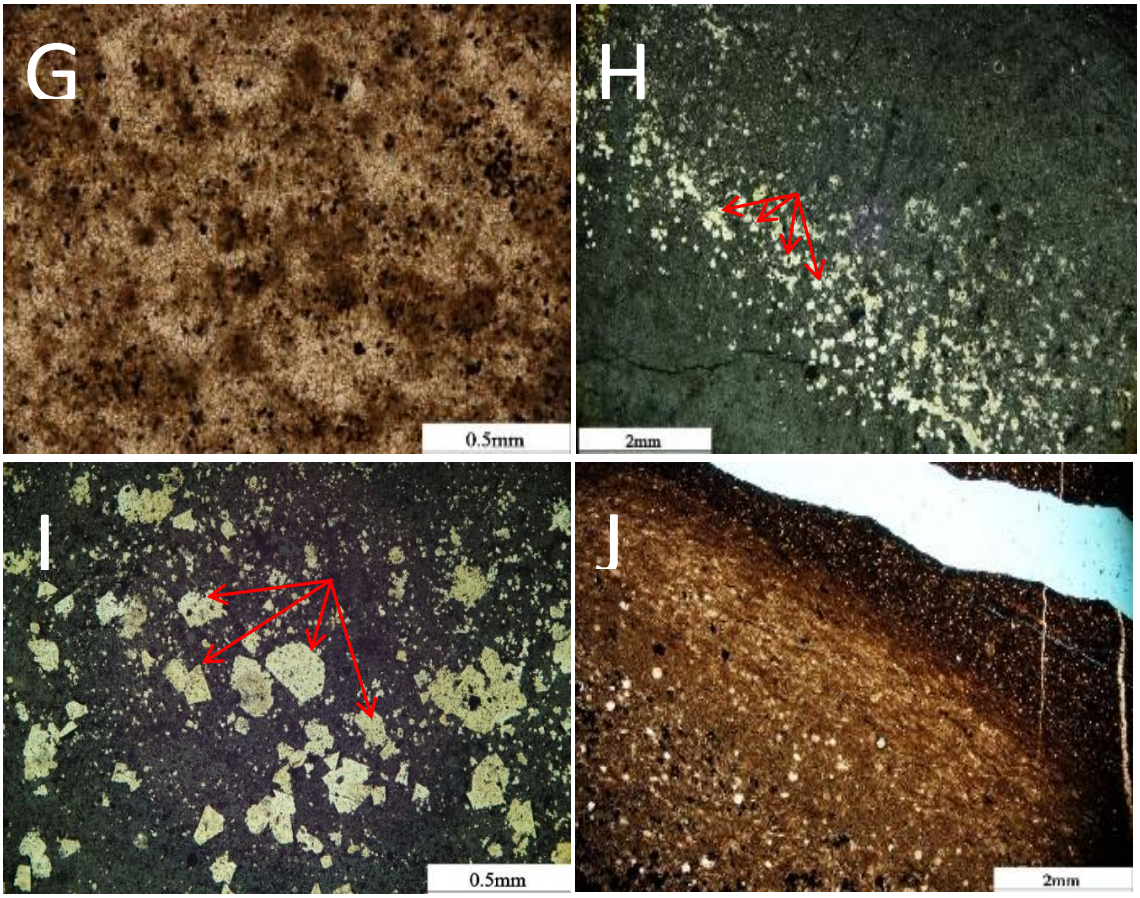

Figure 15: (continued). Calcite Concretion Type III. G) Type III concretion with matrix composed of pseudo spar (lighter color) and uncompacted peloids (darker areas), small grains of pyrite (black dots) are disseminated in the matrix. Lake Davis No. 1, 4134.8 ft. H) Pyrite (red arrows) in the outer rim of a concretion under reflected light. Lake Davis No. 1, 4134.8 ft. I) Close-up of pyrite showing is it is comprised of euhedral crystals (red arrows). Lake Davis No. 1, 4134.8. J) The mud at the edge of the concretion shows compaction around the concretion. Lake Davis No. 1, 4134.8 ft.

Fracture Fills

Most fractures are filled with authigenic calcite. The size of calcite crystals in fractures is much larger than that in the matrix. In fractures, different calcite patterns appear. Calcite crystals were likely to grow from both sides of the fracture and meet in the middle (Figure 16A). The fibrous calcite may indicate an aragonite origin. Sometimes, the center parts of the fractures are filled with coarse-crystalline calcite (Figure 16B). In the relatively narrow part, calcite tends to be single grains that can be as much as 250 um in size (Figure 16C). Within the fracture, silica cement also exists (Figure 16D).

Bivalve-related calcite

Filibranch shell fragments are rimmed by bladed cement (Figure 17A, B). This type of cement also nucleated on thin-walled shell fragments of bivalves in concretions, where the calcite predominates. In addition, biogenic calcite is more abundant in the skeletal-rich lithofacies. It forms the thick-walled shell fragments (Figure 17C), and square calcite is the most common form of calcite within these shell fragments. The coarse shell fragments were broken into silt- to sand-sized square pieces and some of these fragments were redeposited (Figure 17D).

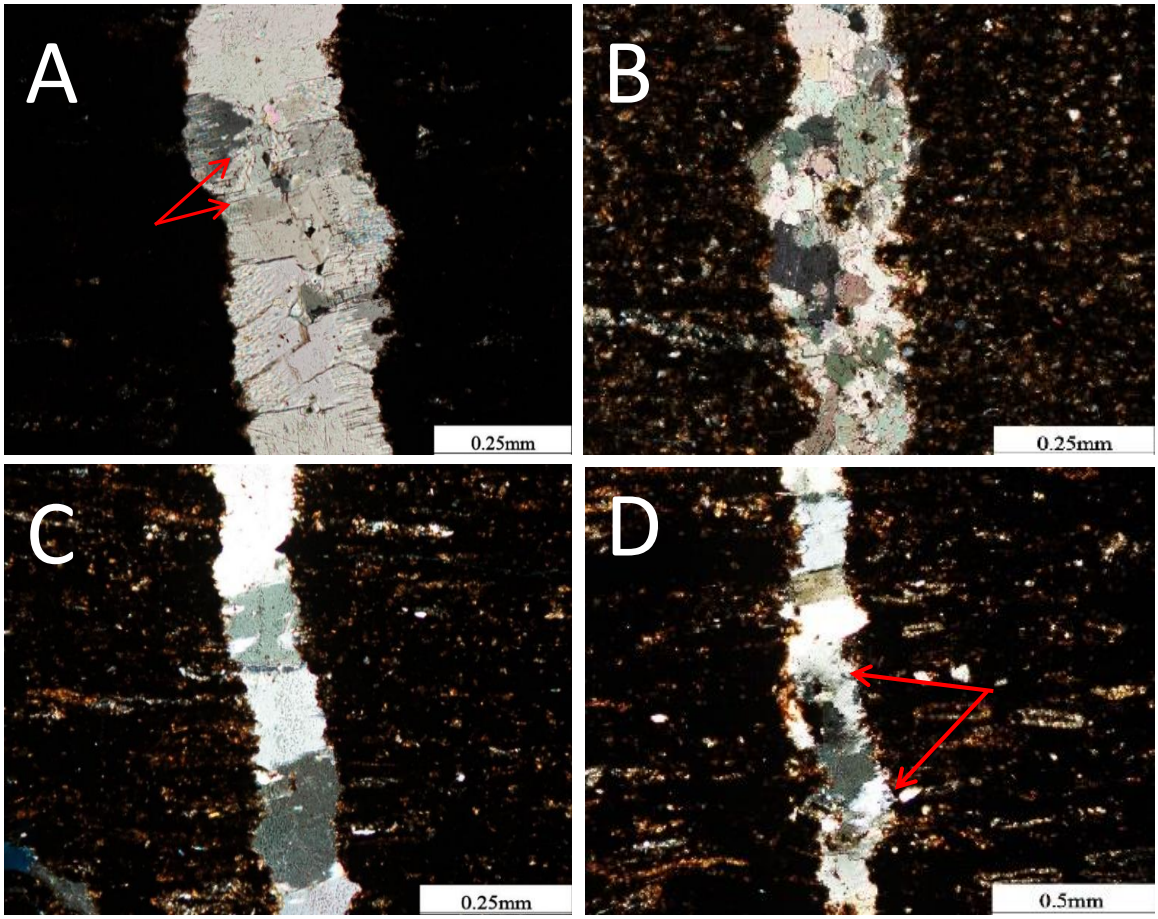

Figure 16: Calcite fracture fills. A) Fracture filled with calcite that initiated from both walls. The fibrous structure of the calcite (red arrows) suggests that it was originally aragonite and recrystallized to calcite. Lake Davis No. 1, 4164.4 ft. Photomicrograph taken with polarized light. B) A fracture filled with equant calcite cement. Lake Davis No. 1, 4164.4 ft. Photomicrograph taken with polarized light. C) Large crystals of calcite bridge the complete fracture. Lake Davis No. 1, 4164.4 ft. Photomicrograph taken with polarized light. D) Authigenic quartz (red arrow) and calcite fill the fracture. Lake Davis No. 1, 4164.4 ft. Photomicrograph taken with polarized light.

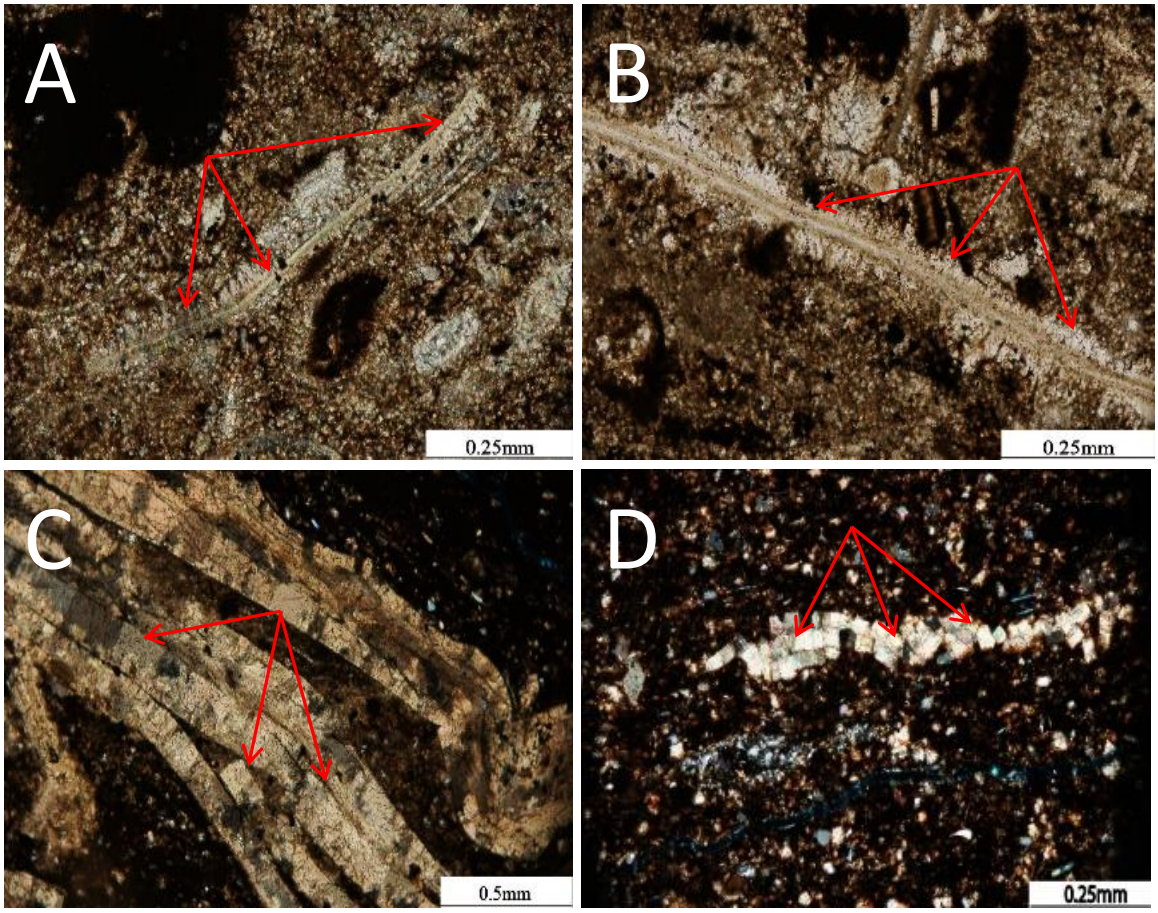

Figure 17: Bivalves diagenesis. A) Authigenic bladed calcite nucleated on thin-walled bivalve fragment (red arrows). Lake Davis No. 1, 4095.2 ft. Photomicrograph taken with polarized light. B) Authigenic bladed calcite nucleated on thin-walled bivalve fragment (red arrows). Lake Davis No. 1, 4095.2 ft. C) Thick bivalve fragments with neomorphous replacement? (red arrows) Lake Davis No. 1, 4197.8 ft. Photomicrograph taken with polarized light. D) Collapsed bivalve fragments (red arrows). Lake Davis No. 1, 4217.5 ft. Photomicrograph taken with polarized light.

Dolomite

Dolomite is considered to be an authigenic phase in the Barnett and was also observed by Milliken et al. (2012). Dolomite exists mainly in calcareous facies, the greatest amount of dolomitization occurring at 4175.1 ft (Figure 18). In other lithofacies, the small dolomite crystals are difficult to differentiate from other silt-sized minerals. The size of dolomite crystals ranges from 50 micrometers to 100 micronmeters. Generally, the grains are partly euhedral with two or three straight sides. The grain surface is iron stained, and XRD data show that most of the dolomite is ferroan dolomite. Commonly, some dolomite particles are clumped (Figure 18B). Some seemingly isolated crystals are rounded and larger than most of the associated particles. A few crystals are elongated (Figure 18C, D). The irregular crystals of dolomite may suggest that they were reworked or corroded.

Pyrite

In the Barnett, pyrite (Figure 19) occurs in two forms: framboidal pyrite and euhedral pyrite. Syngenetic framboidal pyrite (2-4 micrometers in diameter) can form in the water column during the process of deposition, and it indicates anoxic and euxinic water column during time of deposition (Wilkin et al., 1996; Wignall et al., 2005). Under optical microscope, they are too small to be clearly observed. The diagenetic framboidal pyrites formed during diagenesis within the sediment are 6-10 micrometers in diameter (Figure 19A). Under SEM, pyrite framboids are seen to be comprised of many single crystals with pores in between (as will be discussed later). In the Barnett section, euhedral pyrite commonly replaces other minerals and fossils such as agglutinated foraminiferas and shell

fragments (Figure 19B, C). Large amounts of pyrite can occur as cement that occupies not only the chamber of a fossil (Figure 19E), but also in the sheltered voids under the protected area of the shells (Figure 19D). Additionally, pyrite forms cement within pyrite hardgrounds (Figure 19F, G).

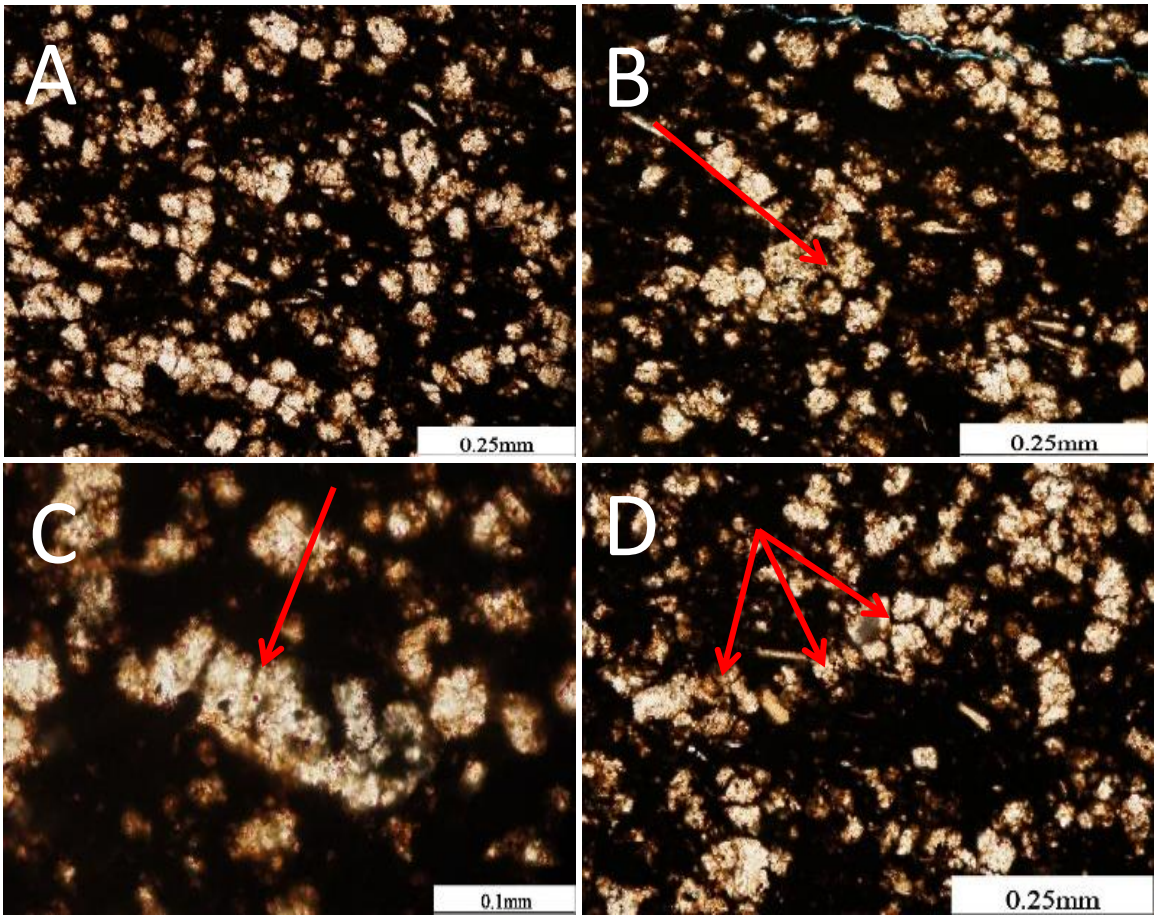

Figure 18: Authigenic dolomite as seen in the Lake Davis No. 1, 4175.1 ft. thin section. A) Dolomite crystals in an organic–rich peloidal matrix. B) Dolomitic aggregate (red arrow). C) An elongate dolomitic aggregate; the aggregates (red arrow) may be reworked clasts. D) Elongate dolomitic aggregates (red arrow).

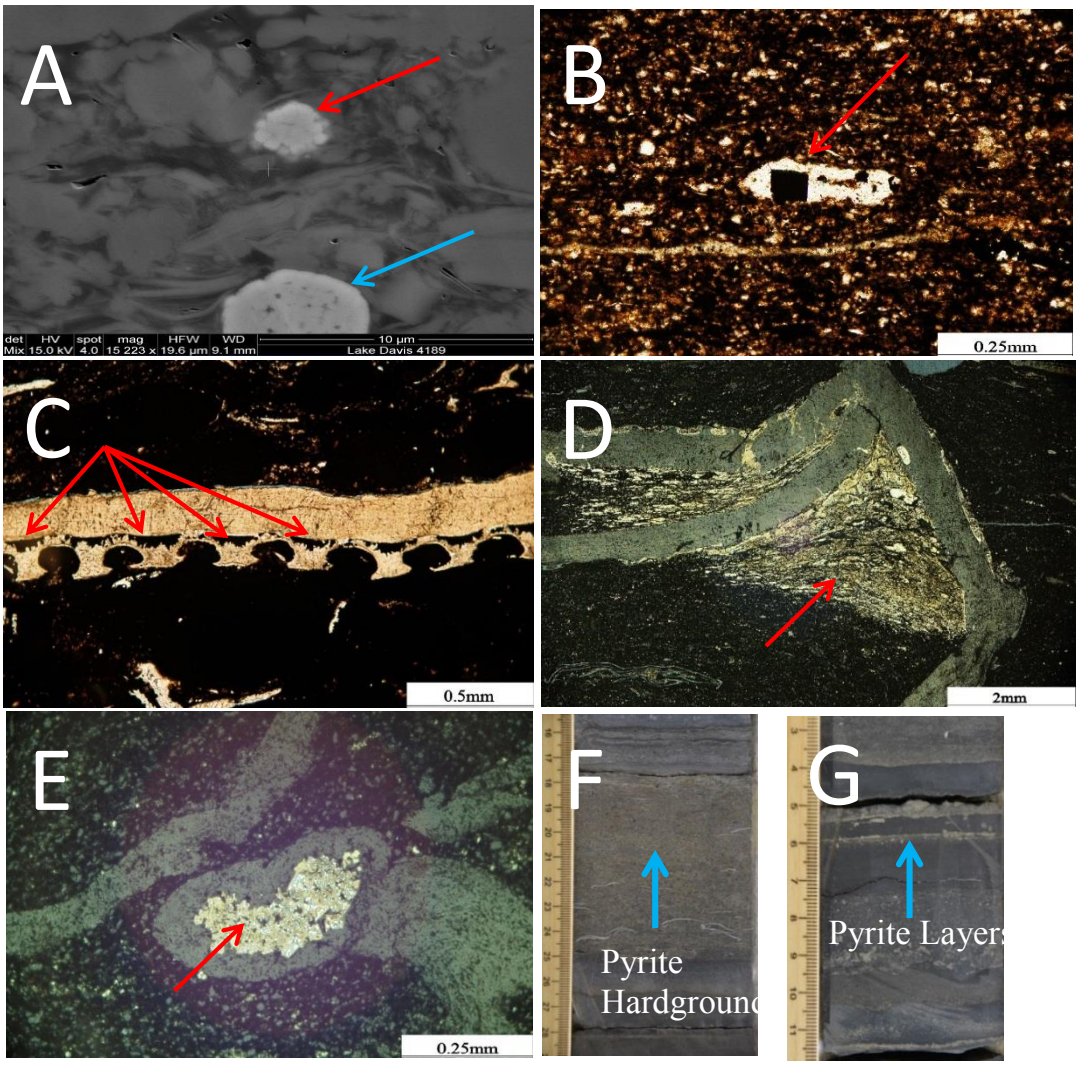

Figure 19: Pyrite. A) SEM photomicrograph of pyrite framboid. According to the size of the framboids, the smaller framboid may be syngenetic pyrite (red arrow) and the larger framboid may be diagenetic pyrite (blue arrow). Lake Davis No. 1 4189 ft. B) Diagenetic pyrite crystal that replaced an agglutinated foraminifera (red arrow). Lake Davis No. 1, 4158.4 ft. C) Pyrite that replaced a shell fragment (red arrows). Lake Davis No. 1, 4181.3 ft. D) Local pyrite cementation around deformed skeletal fragments (red arrow) under reflected light. Lake Davis No. 1, 4181.2 ft. E) Pyrite in the interparticle pore space of a bioclast (red arrow) under reflected light. Lake Davis No. 1, 4181.3 ft. F) Core slab showing thick pyritized layer may be a pyrite hardground. Mesquite No. 1 3699.5 ft. Scale in centimeters. G) Core showing several pyrite layers, which may be hardground. Mesquite No. 1, 3756.2 ft. Scale in centimeters.

Peloids

Peloids (Figure 20) are a comprehensive descriptive term for polygenetic grains composed of micro- and cryptocrystalline carbonate (McKee and Gutschick, 1969). Under the microscope, peloids commonly have no internal structures. Two types of peloid appear in the Barnett cores: the predominant form is a fine-grained gray to black rounded peloid (Figure 20A) having no internal structures. The other form is the flat and elongated grain of unclear origin (Figure 20D). This flat peloid is bright yellow and ranges from micrometer-scale to millimeter-scale in size.

Rounded Peloids

Rounded peloids (less than 50 microns) are probably biotic and clay associated pellets. Characteristics were difficult to describe because of their black color and structureless texture. This type of peloid is widely distributed in all of the lithofacies in varying amounts. The dark shading viewed under the microscope may be caused by a large amount of organic matter and clay minerals. Coarser peloids (0.2-0.3 mm) that are much rarer mainly exist in debris deposits and concretions (Figure 20B). They may also come from preexisting carbonate mud or micritic remnants that underwent post-depositional reworking that allowed rounding of the peloid (Flügel, 2004).

Flat Peloids

The flat peloids are elongated, bent, and sometimes irregular in shape. They are poorly sorted and have a great variety of sizes (0.2mm to 0.8mm), but generally they are parallel to bedding (Figure 20C). Internally, this type of peloid contains inclusions of silt-sized carbonate or terrigenous particles that are similar as the mud matrix. The dramatically varied size and texture may indicate an intraclast origin. It is important to note that their occurrence is in association with allochems such as phosphate, which also suggests a transported origin. Besides, they may be associated with high-energy depositional events that were able to scour and rip up the previously deposited mud.

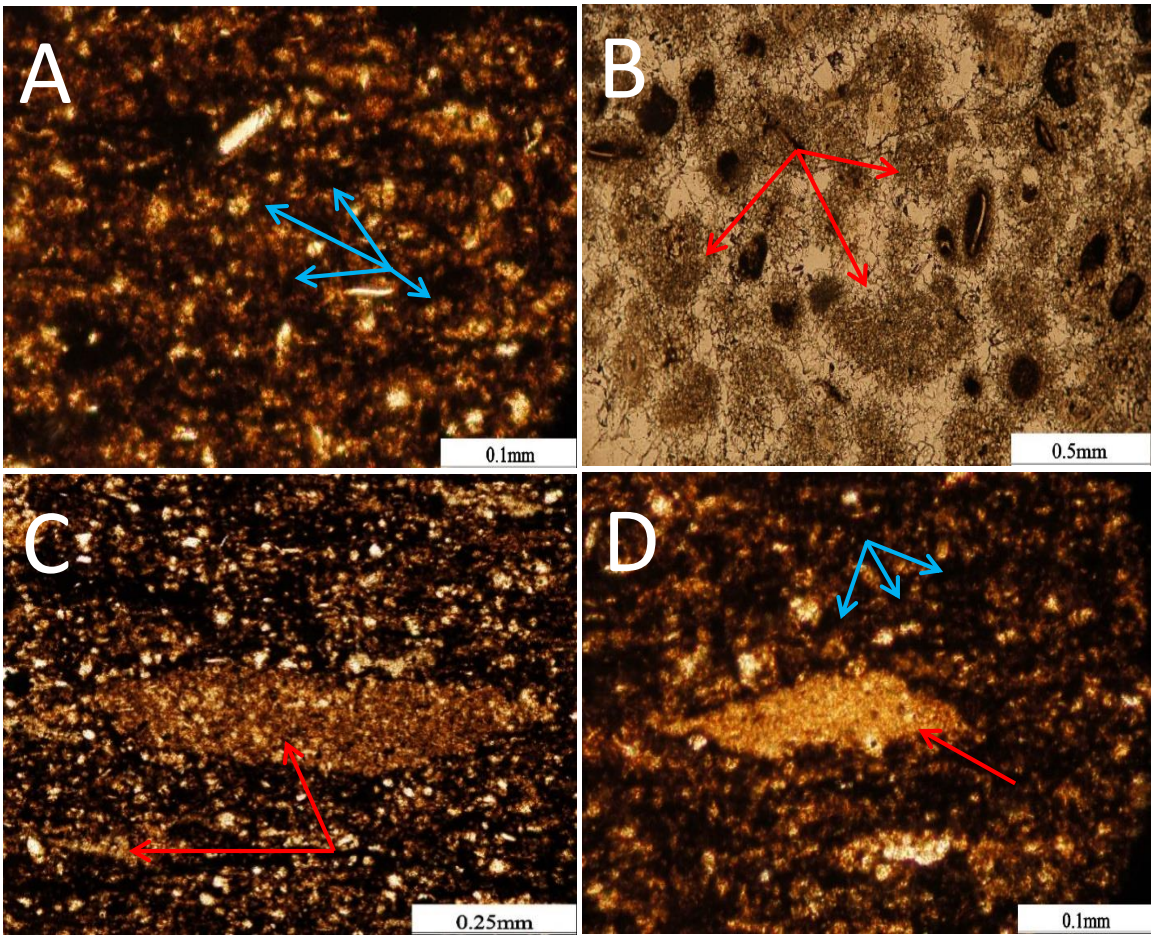

Figure 20: Peloids. A) Black rounded peloid matrix (blue arrows) with detrital quartz. Lake Davis No. 1, 4113.2 ft. B) Peloids from calcite concretion (red arrows). Lake Davis No. 1, 4104.2 ft. C) The flat peloids (red arrows) show a large contrast in size. Lake Davis No.1, 4137.7 ft. D) An elongated flat peloid (red arrow) that is much coarser than surrounding rounded black peloids (blue arrows). Lake Davis No. 1, 4113.2 ft.

Phosphate

In the Barnett, the phosphate accumulations are composed of pellets and cement (Figure 21). Phosphatic pellets as first proposed by Prevot (1982) may appear as ooids, coated grains, and structureless grains. They have a broad spectrum of various morphologies, which differ slightly in the origin and internal texture, but mostly are rounded and rarely irregular. Since the Barnett was deposited in deep-water conditions below storm-wave base (as discussed in earlier), most of the phosphate accumulations are considered to have been transported to the basin from the adjacent slope area (Loucks and Ruppel, 2007).

The rim envelopes and apatite cement developed around a variety of different grains. The coated grains are rounded or elongated. As seen in the microscope, the nucleus within the coated grain appears diverse, including bioclasts, detrital grains, grain aggregates, pre-existing phosphate grains, ooids, and organic matter (e.g. Figure 21A to C). Some internal cavities within clasts such as the chambers of foraminifera are filled with apatite cement (Figure 21F). According to Follmi et al. (1991), low-sedimentation rates and repeated reworking of the substrate accelerate phosphogenesis by allowing high concentrations of phosphate and fluoride to build up within pore waters, which provided the materials for cementing and coating. As revealed from the cores and thin sections, most of the grains are coated with more than one layer of phosphate, and the different colors reveal their different formation times. Some of the coated grains may not form in situ, but were transported. The coated phosphate grains and ooids (Figure 21D) confirm that there were bottom currents strong enough to erode the muddy bottom and redposit the phosphate

grains. Thus, most of the ooids and coated grains are formed by a composite action: progressive rim cement, plus several episodes of scouring and reworking.

Carbonate Intraclasts

Carbonate intraclasts (Figure 22) mainly exist in nonlaminated silty peloidal calcareous mudstone, phosphatic packstone to grainstone, and in thin layers of debris flow deposits. Most of the clasts are rounded and subrounded. Their shapes suggest that they were eroded and then transported. Most of the intraclasts have a micritic texture, indicating that they are reworked firm carbonate mud (Figure 22B).

Glauconite

Glauconite (Figure 23) commonly occurs with other materials. These diagenetic glauconites are characterized by their particular green color. They were transported to the basin with other biota lived on the slope.

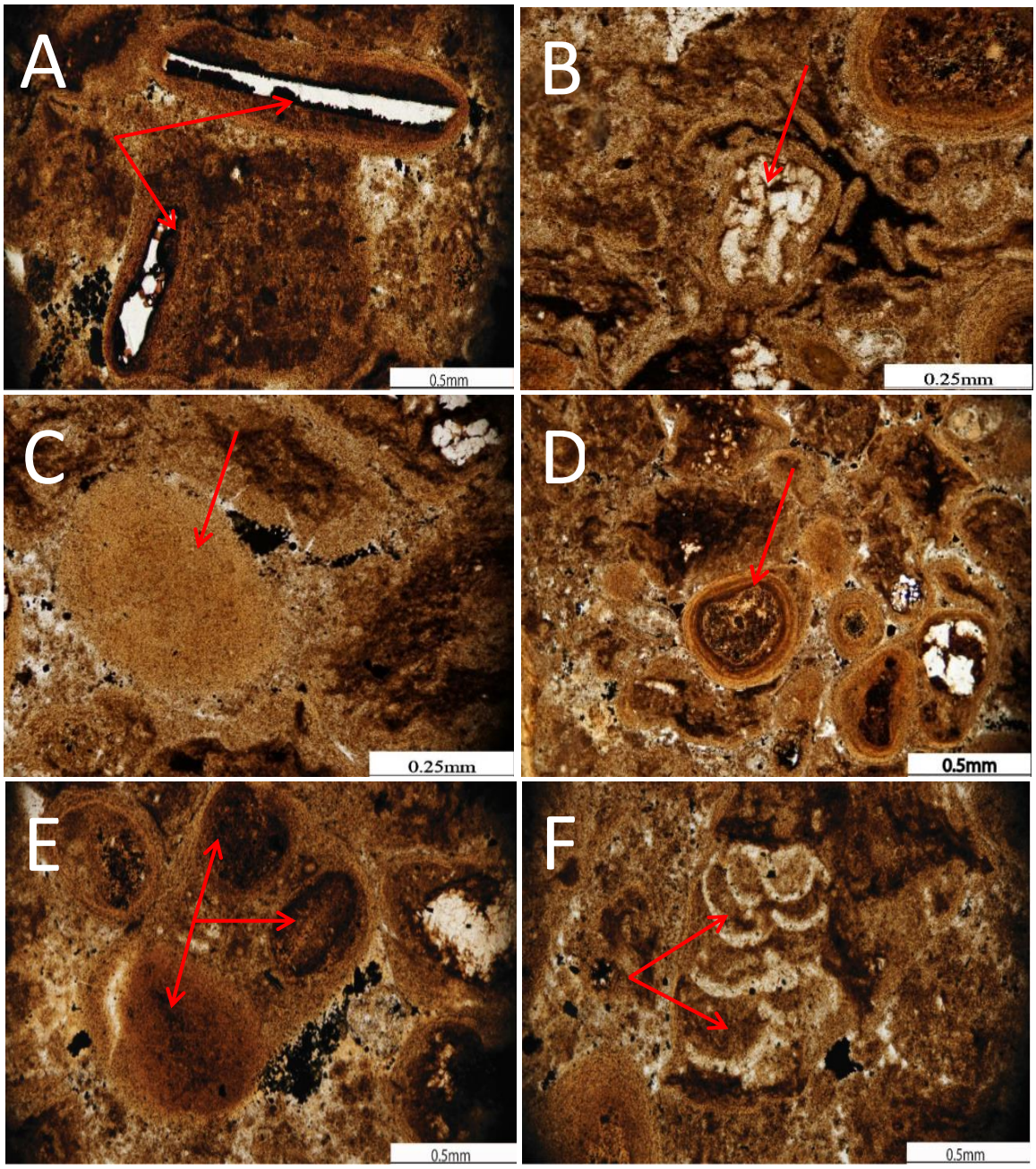

Figure 21: Phosphatic grains. Lake Davis No. 1, 4140.2 ft. A) Nucleus is fish bone (red arrows). B) Nucleus is compacted shell (red arrow). C) Phosphate grain without nucleus (red arrow). D) Phosphatic ooid (red arrow) with several layers indicating several stages of reworking. E) Phosphatic composite grain comprised of three phosphatic grains (red arrows), which indicates reworking and redepositional processes. F) Phosphatic cement filling the chambers of a foraminifer (red arrows).

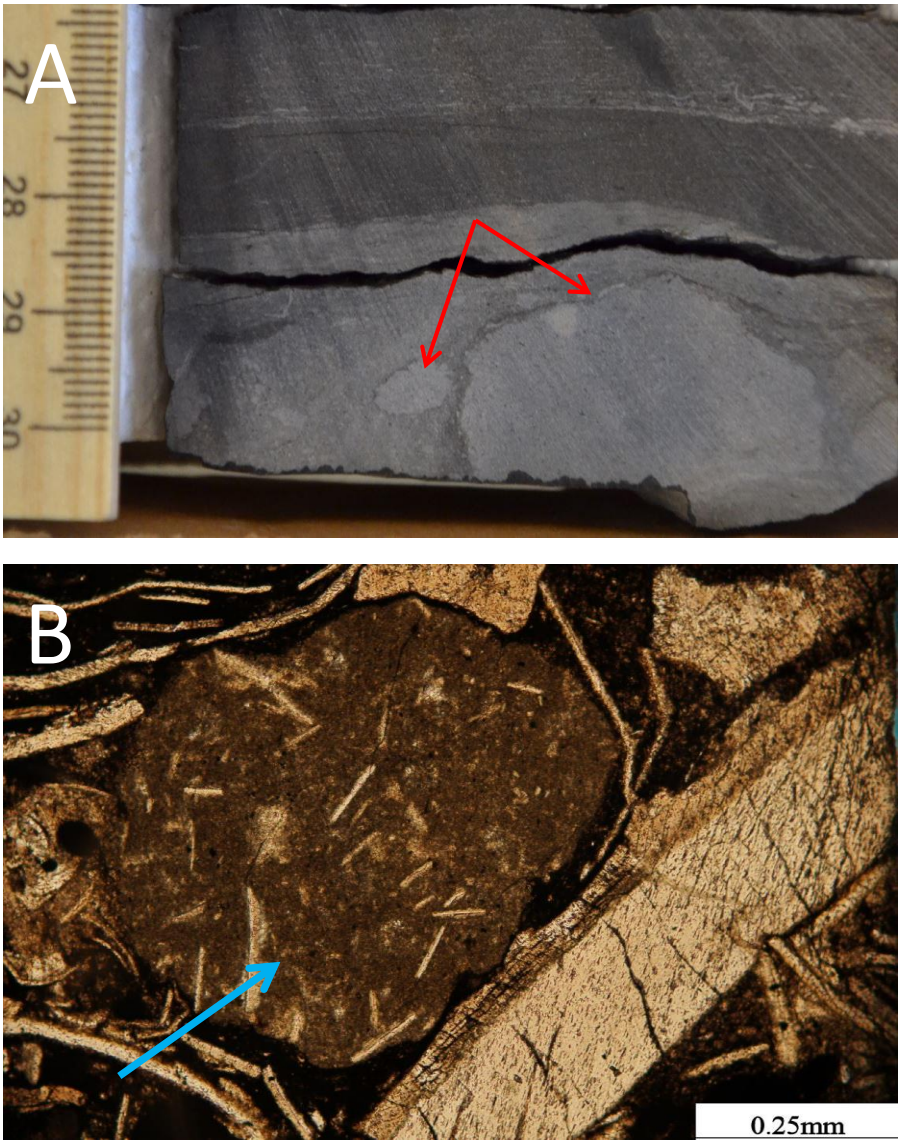

Figure 22: Intraclasts. A) Core slab photograph showing carbonate mud intraclasts (red arrows). Mesquite No. 1, 3782.9 ft. Scale in centimeters. B) A carbonate intraclast (blue arrow) with bivalve fragments. Presence of bivalves suggest the intraclast originated on a dysaerobic slope. Lake Davis No. 1, 4195.2 ft.

.

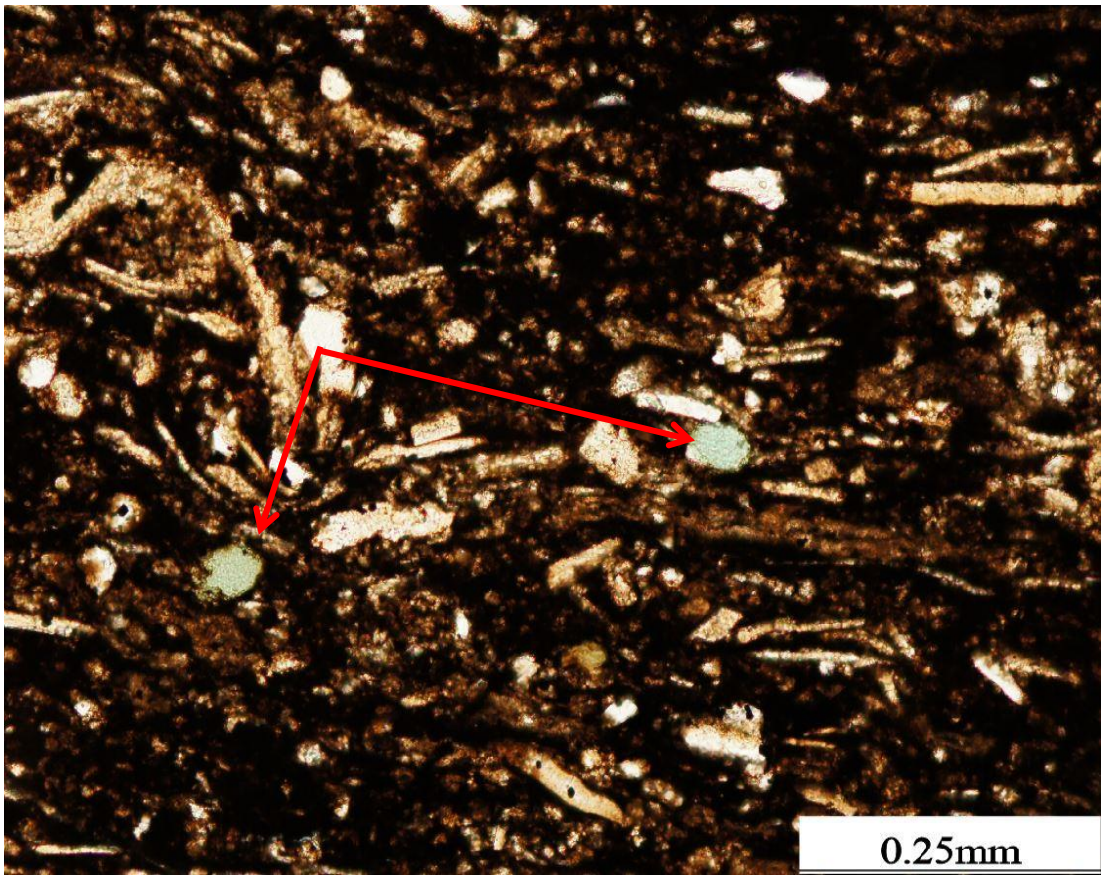

Figure 23: Glauconite (red arrows) appears as green grains. Lake Davis No. 1, 4185.9 ft.

.

Fossils

Agglutinated Foraminifera

Agglutinated foraminifera (Figure 24) are benthic organisms that live in varying environments from brackish coastal water to bathyal (Chekhovskaya, 1973; Scholle and Ulmer-Scholle, 2003; Flügel, 2004; Schieber, 2009). Under plane light, agglutinated foraminifera form a test comprised of particles with the test having a predominantly elongated morphology. Their central lenticular microporous structure resulted from collapse of a formerly hollow spheroidal or tubular body during compaction (Milliken et al., 2007). Highly compacted agglutinated foraminifera may lose the central structure (Figure 24C). Under cross-polaized light, the Barnett agglutinated foraminifera show a microcrystalline quartz fabric. The size of the quartz grains forming the wall is similar to the size of the quartz grains in the adjacent mud, indicating that the quartz silt in the mud is selected by the foraminifera for its wall. With the aid of bright CL intensity, Milliken et al. (2007) also observed detrital feldspars within the agglutinated wall. Agglutinated foraminifera are widely distributed in a variety of lithofacies within the Barnett Formation. Among these lithofacies, siliceous mudstone has the most abundant and intact agglutinated foraminiferal tests, which are aligned parallel to the bedding. Some of them are deformed by differential compaction around more rigid particles (e.g., phosphatic grains) (Figure 24F). The agglutinated foraminifera are rare in calcareous-rich lithofacies, especially where some shell fragments of mollusks and brachiopods are locally abundant, and this is consistent with observations by Milliken et al. (2007). Foraminifera are dispersed in the

phosphatic facies and are highly distorted, indicating compaction after transport (Figure 24A, D).

Radiolarians

Radiolarians (Figure 25) are marine plankton distributed around the thermocline (e.g., Takahashi and Ling, 1980; Gowing, 1986). A study of 136 radiolarian taxa (Kling and Boltovskoy, 1995) reported that radiolarians could live from shallow water to a depth of 6000 ft. (2000 m). Generally, radiolarians have a siliceous skeleton that may transform to chert and quartz (Scholle and Ulmer-Scholle, 2003) or be replaced by calcite. Their living habitat and planktonic characterization indicate that they are generally deposited by hemipelagic and pelagic settling. In the Barnett mudstone, the size of radiolarians ranges between 0.1 and 0.2 mm. Almost all of the radiolarians are spumellarian skeletons, with or without spines (Figure 25A, B). They are all replaced by calcite and quartz (Figure 25C). Within the sphere framework, equant calcite is the dominant cementing form (Figure 25D). Radiolarians were observed within each lithofacies, but they are only abundant in carbonate concretions. Their abundance in concretions may be related to better preservation.

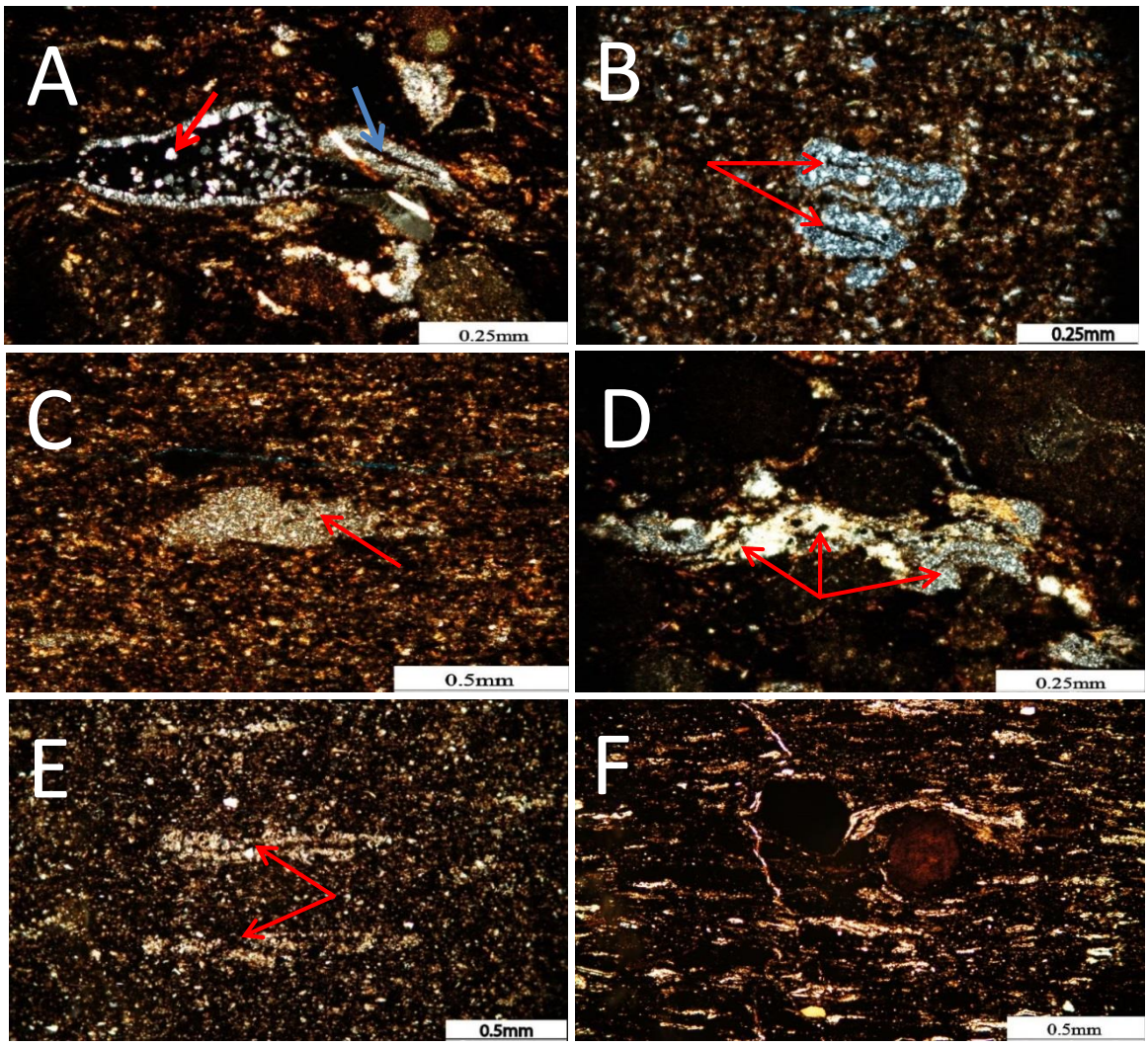

Figure 24: Agglutinated foraminifera. A) An uncompacted agglutinated foraminifera (red arrow) comprised of silt-sized quartz. A compacted agglutinated foraminifera (blue) is also present. Cross-polarized light. Lake Davis No. 1 4140.1 ft. B) Two agglutinated foraminifera with siliceous outer walls (red arrows). Cross-polarized light. Lake Davis No. 1, 4140.2 ft. C) A cut through an agglutinated foraminifera where the central chamber has collapsed (red arrow). Cross-polarized light. Lake Davis No. 1, 4113.2 ft. D) Highly deformed agglutinated foraminifera compacted around rigid phosphate grains (red arrows). Cross-polarized light. Lake Davis No. 1, 4140.1 ft. E) Agglutinated foraminifera comprised of carbonate grains (red arrows). The agglutinated foraminifera utilized grains that were available. Lake Davis No. 1, 4226.2 ft. F) Multiple parallel aligned agglutinated foraminifera and phosphatic grain. The concentration of agglutinated foraminifera may be the result of transport. Lake Davis No. 1, 4164.4 ft.

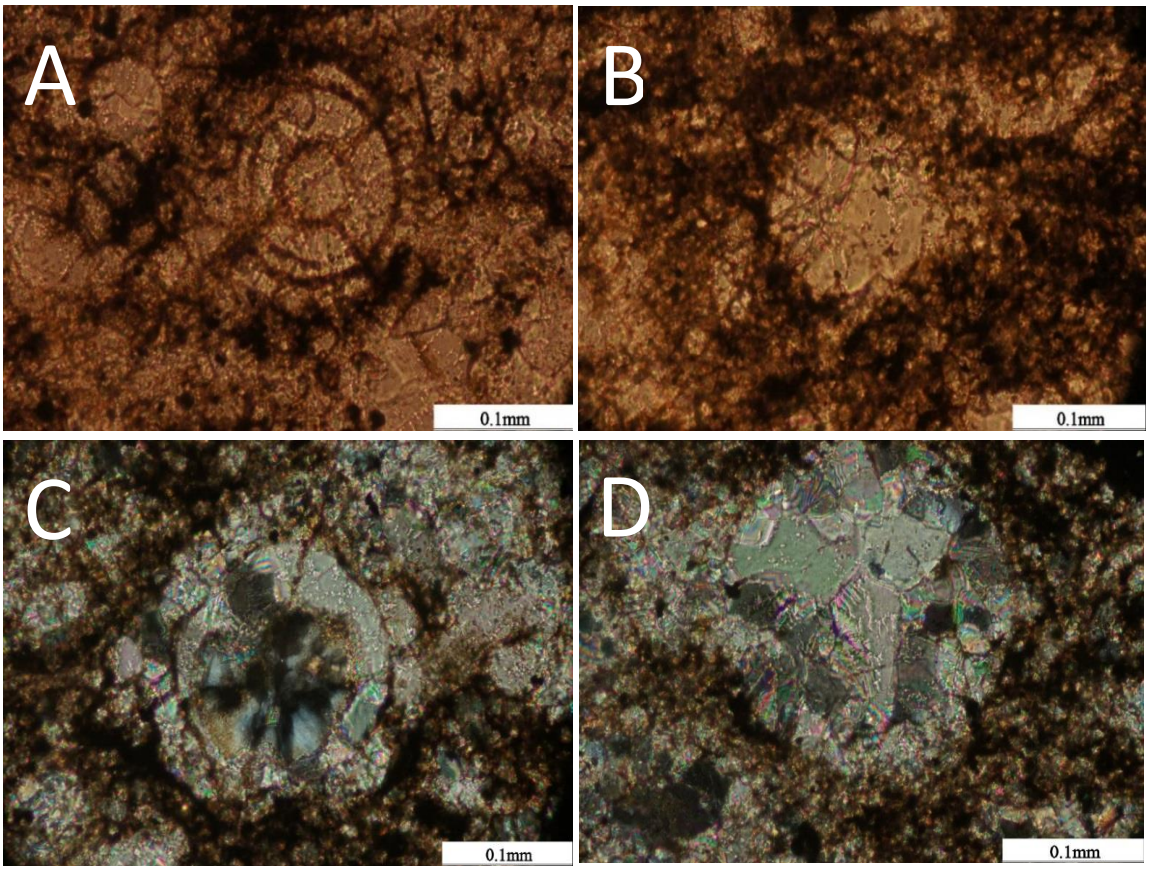

Figure 25: Radiolarians. A) Possibility a *Nyfrieslandia* with the inner wall and spines preserved. Lake Davis No. 1, 4104.1 ft. B) Calcite replaced radiolarian. Lake Davis No. 1, 4104.1 ft. C) A radiolarian replaced by calcite and quartz. Photomicrograph taken with cross-polarized light. Lake Davis No. 1, 4103.9 ft. D) Radiolarian replaced by equant calcite cement. Photomicrograph taken with cross-polarized light. Lake Davis No. 1, 4103.9 ft.

Sponge Spicules

Sponge spicules (Figure 26) are one of the most important silica-producing animals in the Barnett Formation. Most of them lived on deeper water shelf and slopes shallower than 1000 m (Scholle and Ulmer-Scholle, 2003). The accumulations of sponge spicules were thought to have originated from the Chappel Platform, the site of spiculite-bearing sponge reefs (Abouelresh and Slatt, 2011). They are most common in the siliceous mudstone of the Barnett Formation. Many sponge spicules were not preserved as they were dissolved and assimilated in the siliceous matrix. Microscleres as seen with the microscope are generally 1 micrometer or less in transverse section, which appears as a ring (Figure 26C). In the two cores, the smaller-sized sponge spicules can be monaxons or multi-axoned (Figure 26A), and they commonly have a central canal (Figure 26B). As noted by the thin section analysis, nearly all of the sponge spicules were replaced by quartz (Figure 26D).

Bivalves, Ostracods, and Brachiopods

The occurrence of bivalves, ostracods, and brachiopods is evidence of gravity flows transporting allochems deposited on the dysaerobic slope into the anoxic basin. In the core, except for some thick-shelled bivalves and ostracods (Figure 27B), most fossils are broken and extensively compacted (Figure 27C).

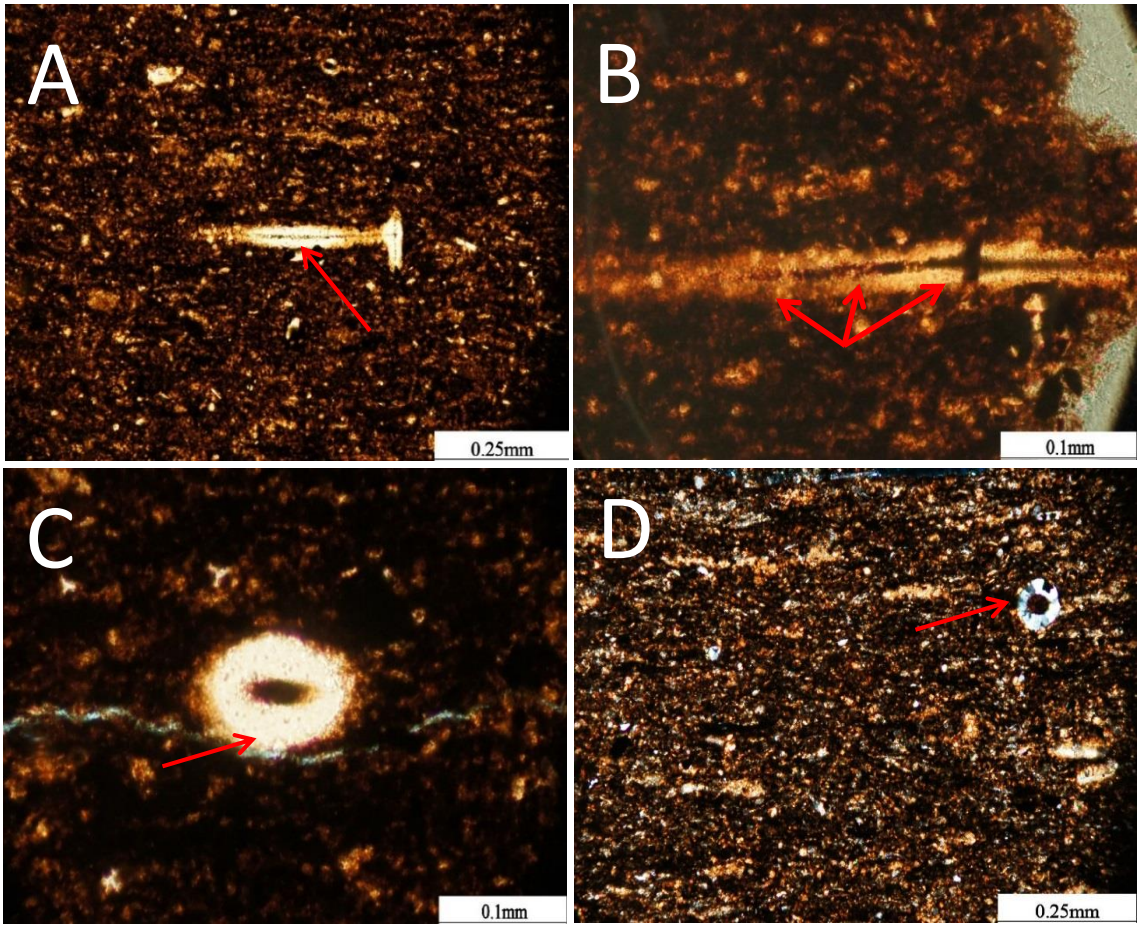

Figure 26: Examples of sponge spicules from the Lake Davis No. 1, 4115.9 ft. A) A longitudinal section of a sponge spicule with its holdfast (red arrow). B) Longitudinal section of a sponge spicule (red arrows). C) Transverse section of a sponge spicule. D) A sponge spicule under cross-polarized light showing it is comprised of silica.

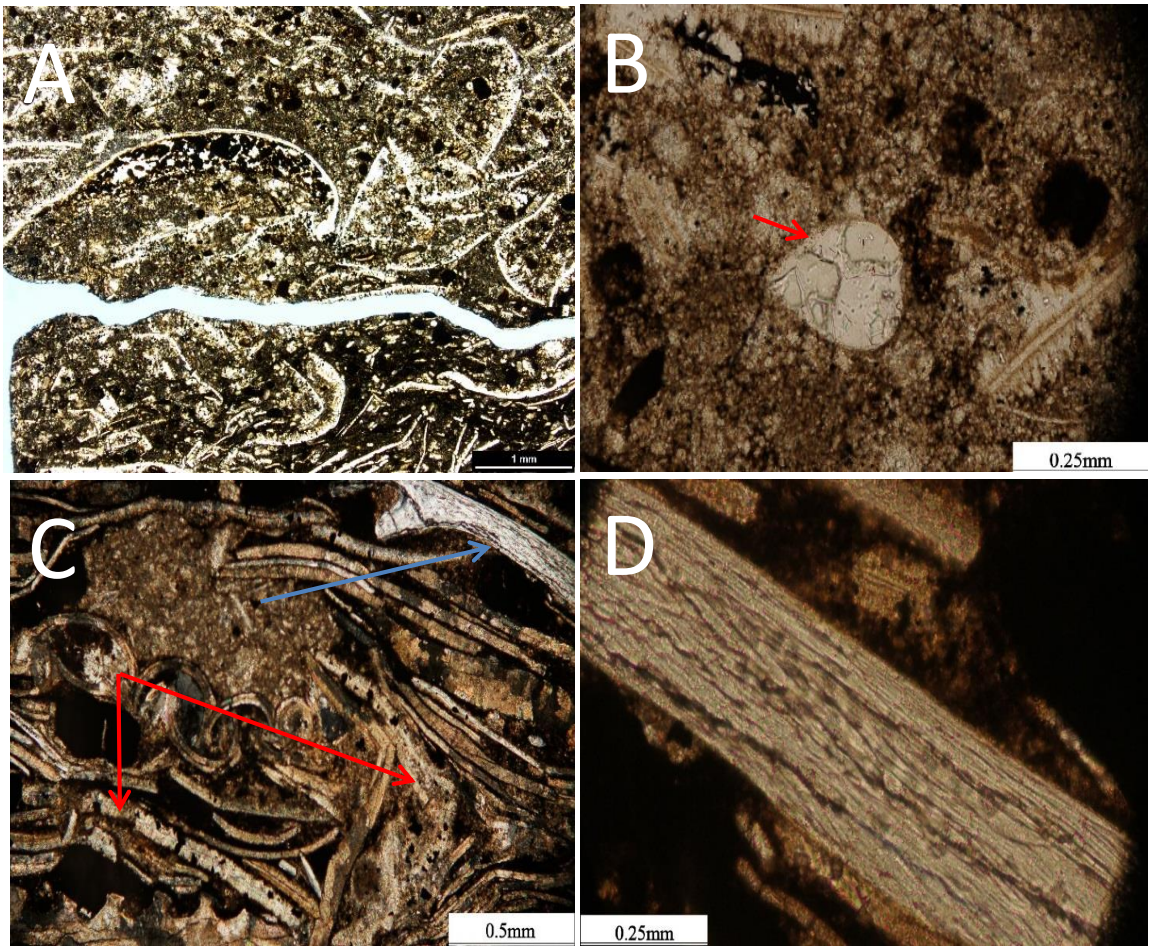

Figure 27: Bivalves, brachiopods, and ostracods. A) Broken and compacted thin-walled bivalves. Lake Davis No. 1, 4095.2 ft. B) Ostracod in center of photomicrograph (red arrow). To the right is a bivalve fragment with bladed cement. Lake Davis No. 1, 4095.2 ft. C) Debris flow deposit containing bivalves (red arrows), brachiopods (blue arrow), and carbonate intraclasts. Lake Davis No. 1, 4168.2 ft. D) *Platystropha cypha* (brachiopod) with impunctate wall. Lake Davis No. 1, 4168.2 ft.

Other Fossils

Cephalopods and echinoderms (probably crinoids) are present (Figure 28D). Cephalopods are common in the Barnett, and most of them are ammonoids. They are whole cephalopods to fragments that range from 0.3 mm or less to more than 1 cm (Figure 28A). In the whole cephalopods, the internal chambers are filled with calcite or saddle dolomite. The saddle dolomite is a late diagenetic feature and indicates higher temperature precipitation (Radke and Mathis, 1980) (Figure 28B). Echinoderms account for only a small fraction of the fossils. In the core, large crinoid spines commonly occur along with shell fragments transported by gravity flow (Figure 28C).

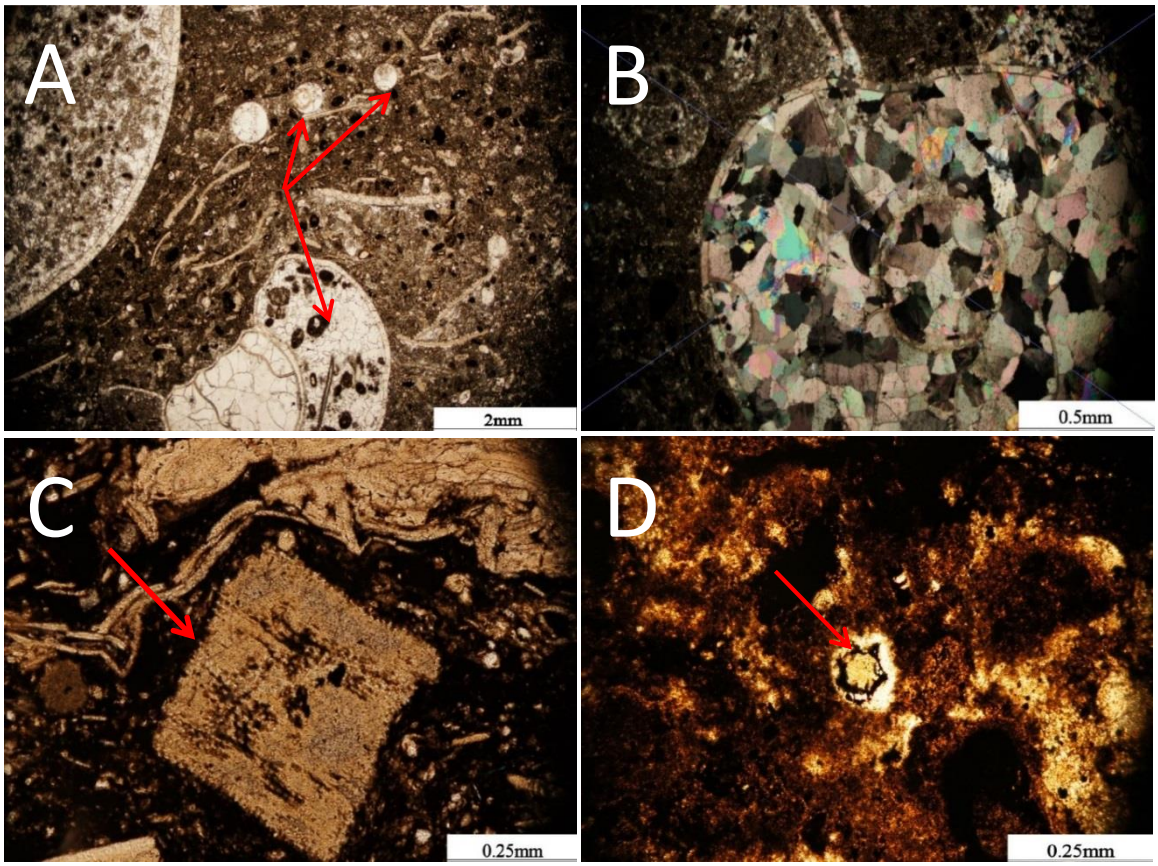

Figure 28: Cephalopods and crinoids. A) Cephalopods of several sizes (red arrows). Lake Davis No. 1, 4095.2 ft. B) Large, intact cephalopod filled with saddle dolomite. Cross-polarized light. Lake Davis No. 1, 4095.2 ft. C) Crinoid fragments (red arrow). Lake Davis No. 1, 4177.6 ft. D) Cross section of echinoderm spine (red arrow). Lake Davis No. 1, 4145.2 ft.

LITHOFACIES

INTRODUCTION

Classification of lithofacies within a mudrock succession is of great importance for the recognition of sweet spots and for future reservoir development. Mudrock lithofacies are difficult to identify by utilizing core description alone because of the fine-grain size of the particles in each lithofacies. Thin section analysis greatly aided in the description and designation of the lithofacies. Therefore, in this study a combination of conventional core observation, thin sections, and XRF-based elemental logs was used to derive a classification of lithofacies.

The workflow was to 1) make a general classification of the three dominant matrix types (siliceous, argillaceous/clay-rich siliceous, and calcareous-dominated) in the cored mudrock succession based on XRF (Figure 7) and XRD chemical data (Figure 10); 2) describe the texture of the rock with a binocular microscope; 3) use thin sections to determine the texture, fabric, dominant mineralogy, and biota; and 4) integrate all the information to designate the lithofacies. In this classification, five dominant lithofacies were identified: 1) laminated clay-rich silty and skeletal peloidal siliceous mudstone; 2) laminated skeletal silty peloidal siliceous mudstone; 3) nonlaminated silty peloidal calcareous mudstone; 4) laminated and nonlaminated skeletal calcareous mudstone; and 5) skeletal phosphatic packstone to grainstone.

LAMINATED CLAY-RICH SILTY PELOIDAL SILICEOUS MUDSTONE

Laminated clay-rich silty peloidal siliceous mudstone is the dominant lithofacies in cores (Figure 29), and composes 40 percent of the total lithofacies. This lithofacies is generally organic rich; statistical data on TOC content is presented in Organic Geochemistry Chpater. This lithofacies is poorly to well laminated, as can be seen in thin section and core. With organic matter and abundant flat peloids, it becomes laminated because flat peloids tend to be horizontally aligned (Figure 29B). No bioturbation occurred as evidenced by the undisturbed laminations, probably related to a deep-water anoxic environment (as will be discussed in Inorganic Geochemistry Chapter). The rock is composed predominantly of clay-sized minerals, as well as varying amounts of silt-sized to coarser allochems. Clay to silt-sized peloid and detrital silts such as quartz and feldspar are the dominant grains in this lithofacies (Figure 29C). Other coarser grains include rounded phosphate grains, isolated fossils such as agglutinated foraminifera, and fragments of bivalves. Variations in the amount of organic matter, peloids, silt-sized grains, and bioclasts have created very dissimilar lithofacies appearances (Figure 29B, D). Early lithified phosphatic grains are locally concentrated and ductile grains have compacted around the rigid phosphate grains. Well-developed laminations are observed from the interbedding of peloid layers and agglutinated foraminifera-rich layers (Figure 29D).

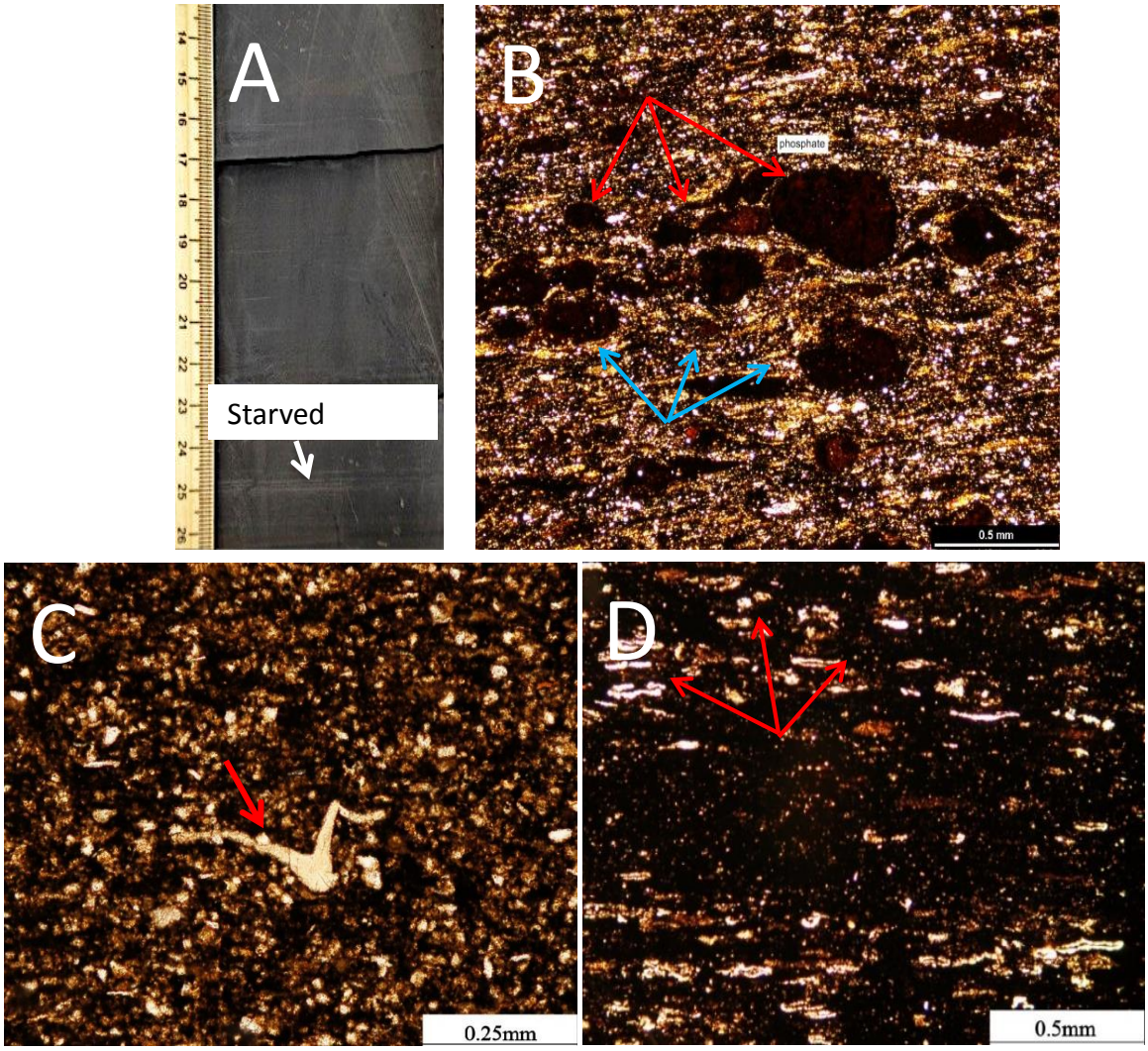

Figure 29: Laminated clay-rich silty and skeletal peloidal siliceous mudstone. A) Core slab showing starved ripples. Lake Davis No. 1, 4154.7 ft. Scale in centimeters. B) Well-laminated fabric caused by the large amount of flat peloids (blue arrows); some peloids are compacted around phosphate grains (red arrows). Lake Davis No. 1, 4076.4 ft. C) Fish bone fragment (red arrow) in the silt-rich peloidal matrix. Lake Davis No. 1, 4198.9 ft. D) Lamination produced by peloid-rich layer and agglutinated foraminifera-rich layer. Red arrows indicate agglutinated foraminifera. Lake Davis No. 1, 4164.4 ft.

LAMINATED SKELETAL SILTY PELOIDAL SILICEOUS MUDSTONE

Skeletal silty peloidal siliceous mudstone accounts for 20 percent of the section in the two cores (Figure 30). It is the predominant lithofacies in the upper section of both cores, and thin intervals of this lithofacies are also interbedded with other lithofacies in the lowest part of the core. The facies is generally well laminated, and bioturbation is absent. Loucks and Ruppel (2007) noticed rare trace fossils from the same lithofacies to the north of the study area, including *Helminthopsis*, *Cosmoraphe*, *Chondrites*, and *Nereites*. Two of the most important components of the lithofacies are silt grains and peloids. Black rounded peloids that may be composed of organic matter and clay minerals are uniformly and extensively distributed in the siliceous matrix. Silts are predominantly detrital quartz and fragments of sponge spicules (Figure 30C) as well as some feldspars and micas. Bioclasts are mostly compacted agglutinated foraminifera (Figure 30D). Rounded carbonate grains with unknown origin are present (Figure 30B, D). Various skeletal fragments also contribute to the texture of the lithofacies, including sponge spicules, radiolarians, agglutinated foraminifera, and a small amount of fragmented mollusks. Of these, sponge spicules are the most abundant in this lithofacies. Compared with other lithofacies, the amounts of quartz silt present in this lithofacies are similar to the lithofacies described above (as evidenced by thin section observations). The large amount of siliceous material in this lithofacies is considered not to be related to detrital quartz silt, but to authigenic microcrystalline quartz within the rock. Starved ripples (e.g., Papazis, 2005; Loucks and Ruppel, 2007) were identified in this lithofacies and throughout the core (Figure 30A). Bunting and Breyer (2012) also reported that the mudstone lithofacies has

experienced prevalent silicification so that it contains large amounts of cherty matrix or cement in some areas.

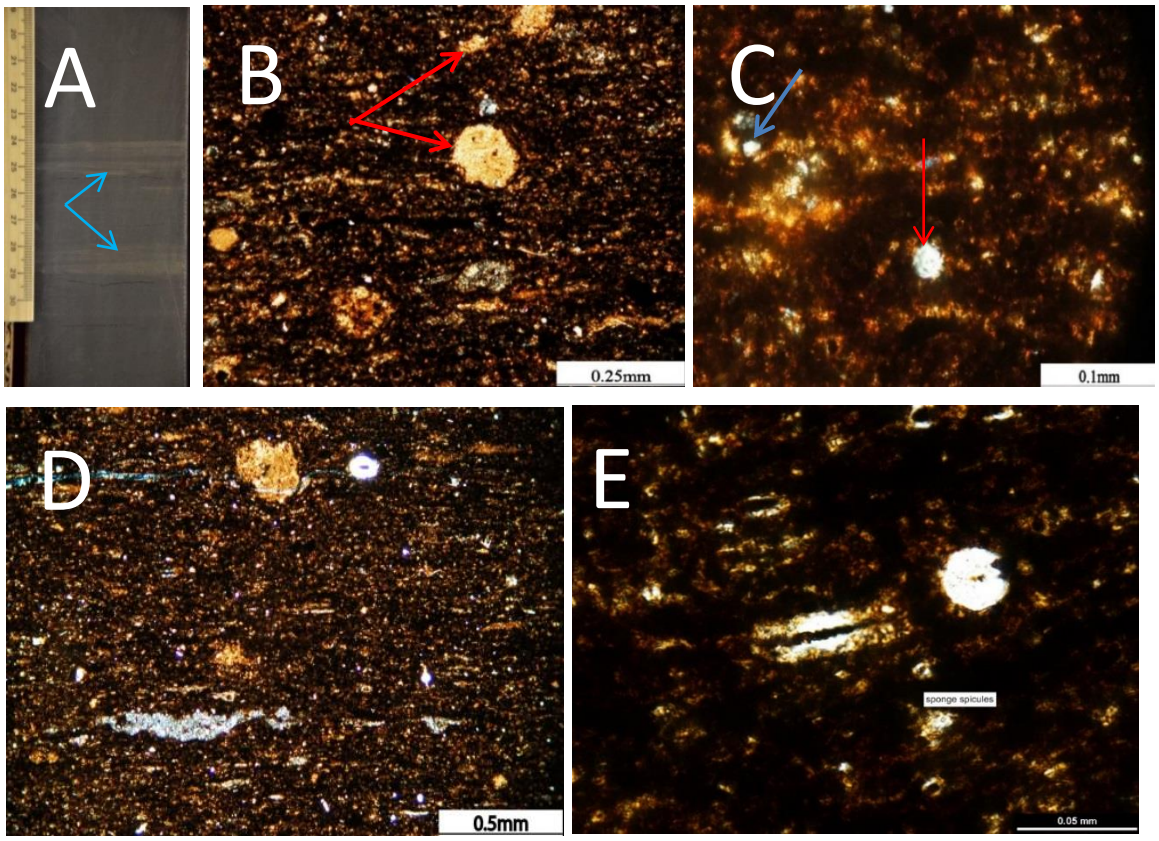

Figure 30: Laminated skeletal silty peloidal siliceous mudstone. A) Core slab with starved ripples (blue arrows). Lake Davis No. 1, 4107.6 ft. Scale in centimeters. B) Well-laminated fabric with rounded carbonate grains (red arrows) and peloids. Lake Davis No. 1, 4081.8 ft. C) Silt-sized mineral disseminated in the peloidal matrix. Blue arrow indicates detrital quartz; red arrow indicates sponge spicules. Lake Davis, No. 1, 4081.8 ft. D) Black, rounded peloidal matrix with rounded carbonate grain (red arrow) and collapsed agglutinated foraminifera (blue arrow). Lake Davis No. 1, 4081.8 ft. E) Thin section showing different slices through sponge spicules. Lake Davis No. 1, 4098.8 ft.

NONLAMINATED SILTY PELOIDAL CALCAREOUS MUDSTONE

In the Mesquite No.1, this lithofacies occurs in the middle and lower part of the core; in the Lake Davis No.1, this lithofacies is concentrated in the upper and lower section but is particularly thin in the middle section of the core as compared to the Mesquite No.1. This lithofacies appears light gray in the core (Figure 31A) because of greater carbonate content. This lithofacies and skeletal calcareous mudstone are both carbonate rich and appear similar on XRF-based elemental logs, but the difference is based on the amount of skeletal fragments that are present. Overall, this facies also has a peloidal texture and nonlaminated fabric with abundant silt-sized particles (Figure 31C). Relatively intact skeletal grains and quartz silt are scarce. Milliken et al. (2012) reported finding agglutinated tests that incorporated dolomite crystals instead of quartz as their outer wall, and this same agglutinated pattern appeared in this lithofacies (Figure 31B). Localized dolomitization was observed at 4175.1 ft in this lithofacies (Figure 31D). These dolomite crystals have a semieuhedral shape that may be related to abrasion or corrosion. The abundant calcareous material in this lithofacies may be related to more frequent gravity flow deposits. The calcareous material is interpreted to have been deposited by dilute turbidity flows or by debris flows that originated from the slope. These deposits led to the accumulation of fine-grained carbonate material in a mudstone matrix.

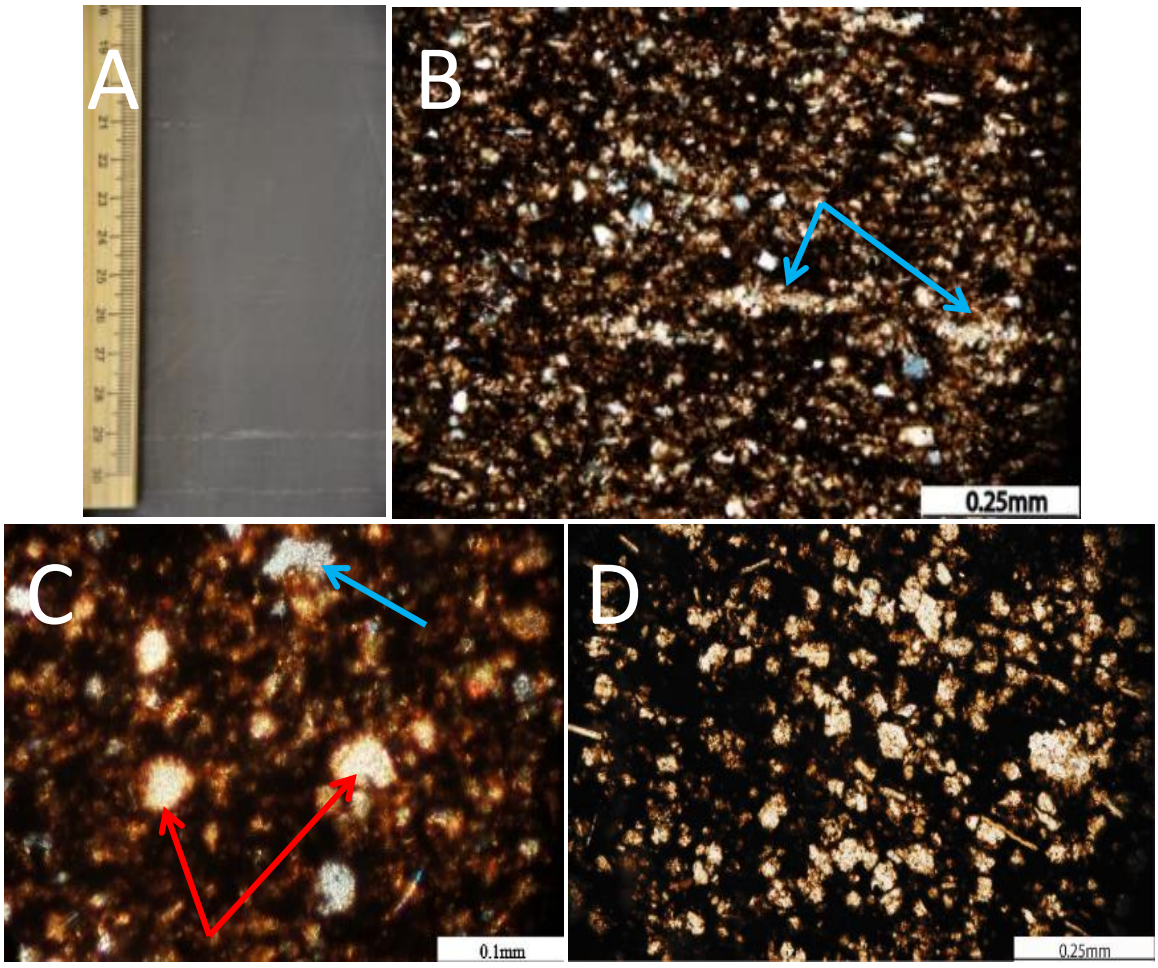

Figure 31: Laminated and nonlaminated skeletal calcareous mudstone. A) Core slab photo showing calcareous mudstone. Lake Davis No. 1, 4211 ft. Scale in centimeters. B) Black peloidal matrix with quartz silt; agglutinated foraminifera with outer wall comprised of carbonate grains (blue arrow). Lake Davis No. 1, 4217.4 ft. C) Carbonate silt (red arrows) and quartz silt (blue arrows) in peloidal matrix. Lake Davis No. 1, 4217.4 ft. D) Dolomitic rhombs disseminated in peloidal matrix. Lake Davis No. 1, 4175.1 ft.

NONLAMINATED SILTY PELOIDAL CALCAREOUS MUDSTONE

Nonlaminated silty peloidal calcareous mudstone composes only a small fraction of the core and occurs as thin layers intercalated in other lithofacies (Figures 32, 33). A comparison between the two cores indicated that these skeletal layers do not correlate. The main components of the lithofacies are skeletal fragments, especially bivalves and brachiopods. This skeletal calcareous lithofacies can be subdivided into laminated or nonlaminated types. In the cores it was commonly noted that the nonlaminated and laminated skeletal calcareous lithofacies are interbedded.

Nonlaminated Skeletal Calcareous Mudstone

Nonlaminated skeletal calcareous mudstone may be the most obvious lithofacies identifiable without a microscope. It is conspicuously white and the fossils are highly compacted. Thickness of this lithofacies ranges from 0.1 to 1.6 inches (0.2 to 4 cm), and the contacts between the skeletal layer and the overlying and underlying layers are very sharp (Figure 32A). In most cases, the contact between the skeletal layer and the mud layer is horizontal, but with more random arrangement and size variations of the skeleton clasts, the contact becomes irregular. Microscopically, this lithofacies is characterized by nonlaminated fabric composed predominantly of transported skeletal fragments of different sizes. Most of the fragments are elongated, deformed or broken (Figure 32B). Fragments of diverse fauna were recognized, including bivalves, brachiopods, ostracods, cephalopods (Figure 32C), and crinoids (Figure 32D). Coarse-grained shell fragments are the most abundant and they are relatively well preserved. The rigidity of the coarser shell

fragments protected the interstitial peloids from compaction (Figure 32E). Commonly, the deposition of coarse-grained skeletal fragments was accompanied by abundant sand-sized, rounded, phosphatic intraclasts (Figure 32F), which in turn dilute the skeletal fragment accumulations. Shell fragments compacted around rigid phosphated grains (Figure 32G). The dominant process that deposited this lithofacies is considered to be debris flows, because the coarse grains comprising this lithofacies were derived from areas on the slope.

Laminated Skeletal Calcareous Mudstone

This type of skeletal calcareous mudstone is much thicker than the last type. Similar biota were recognized from this laminated type, but most of the fragments are silt size, rarely reaching sand-size or coarser. Well-developed laminae are present. The grains are commonly square and elongated, which are biogenic calcite remnants from shell fragments (Figure 33B). Glauconite is common in this lithofacies (Figure 33C). The laminations are a result of skeletal-rich layers interbedded with mud-rich layers (Figure 33D). For the more rigid skeletal-rich layer, the thicknesses are generally from 2 to 2.8 inches (5 to 7 mm); for the soft-mud-rich layer, thicknesses range from 0.8 to 2 inches (2 to 5 mm), which could be related to differential compaction. The fine-grained sediments are considered to be transported by turbidity flows, as indicated by the lamination and grain size. However, they may have also formed by weak bottom currents.

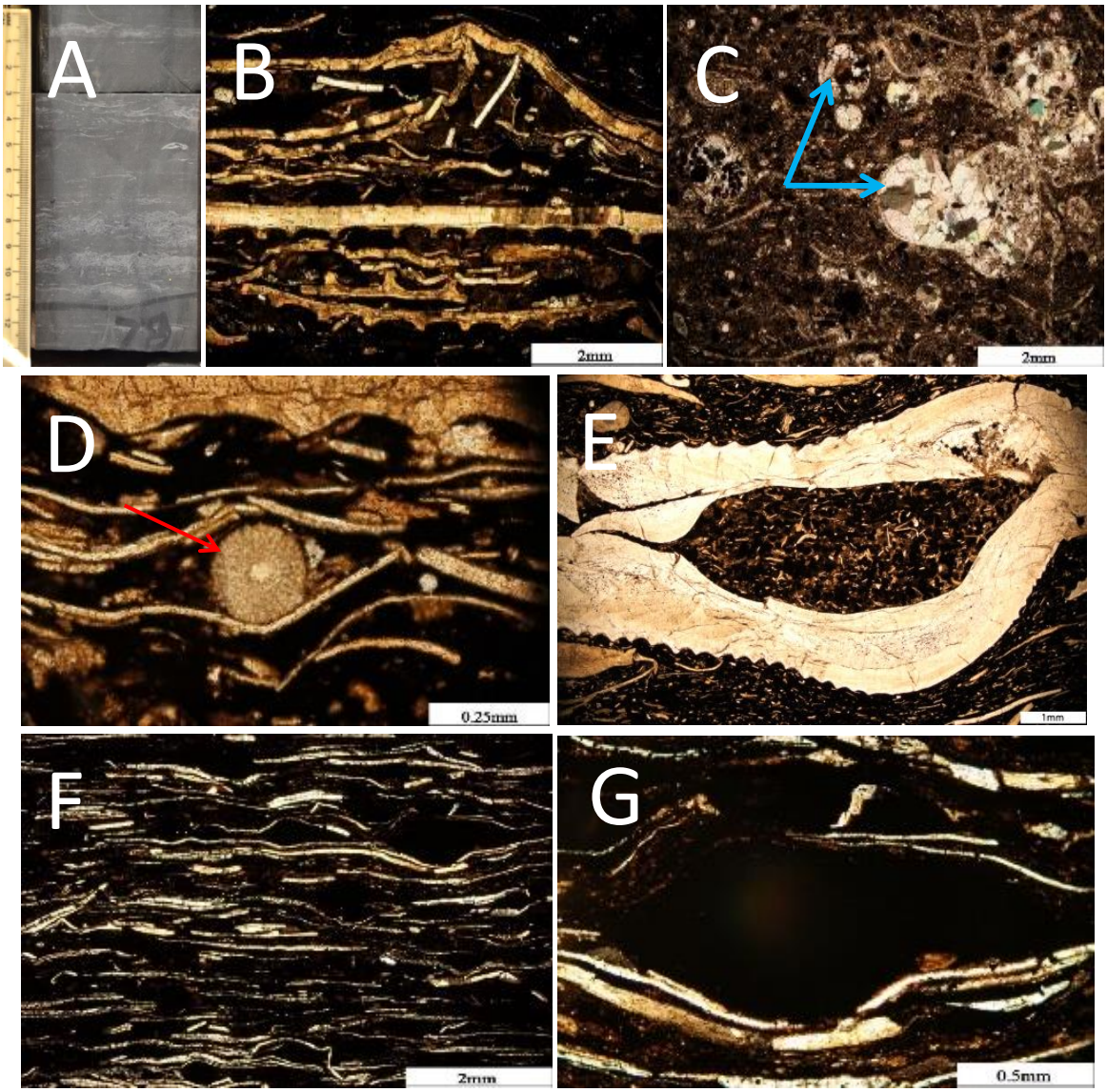

Figure 32: Nonlaminated skeletal calcareous mudstone. A) Core slab displaying several layers of nonlaminated skeletal calcareous mudstone. Lake Davis No. 1, 4077.8 ft. Scale in centimeters. B) Skeletal layer with elongated and deformed bivalve fragments. Lake Davis No. 1, 4188.4 ft. Photomicrograph taken with polarized light. C) Skeletal fragments and whole cephalopods (blue arrows). Lake Davis No. 1, 4095.2 ft. D) Compacted, thin-walled bivalves around of crinoid ossicle fragments (red arrow). Lake Davis No. 1, 4177.6 ft. E) Uncompacted peloids within articulated bivalve; the rigid shell protected the peloids from compaction. Lake Davis No. 1, 4095.2 ft. F) Shell layer of flattened bivalves and phosphate grains comingled during transport. Lake Davis No. 1, 4188.4 ft. G) Compacted bivalve fragments around phosphate grain. Lake Davis No. 1, 4130.6 ft. \

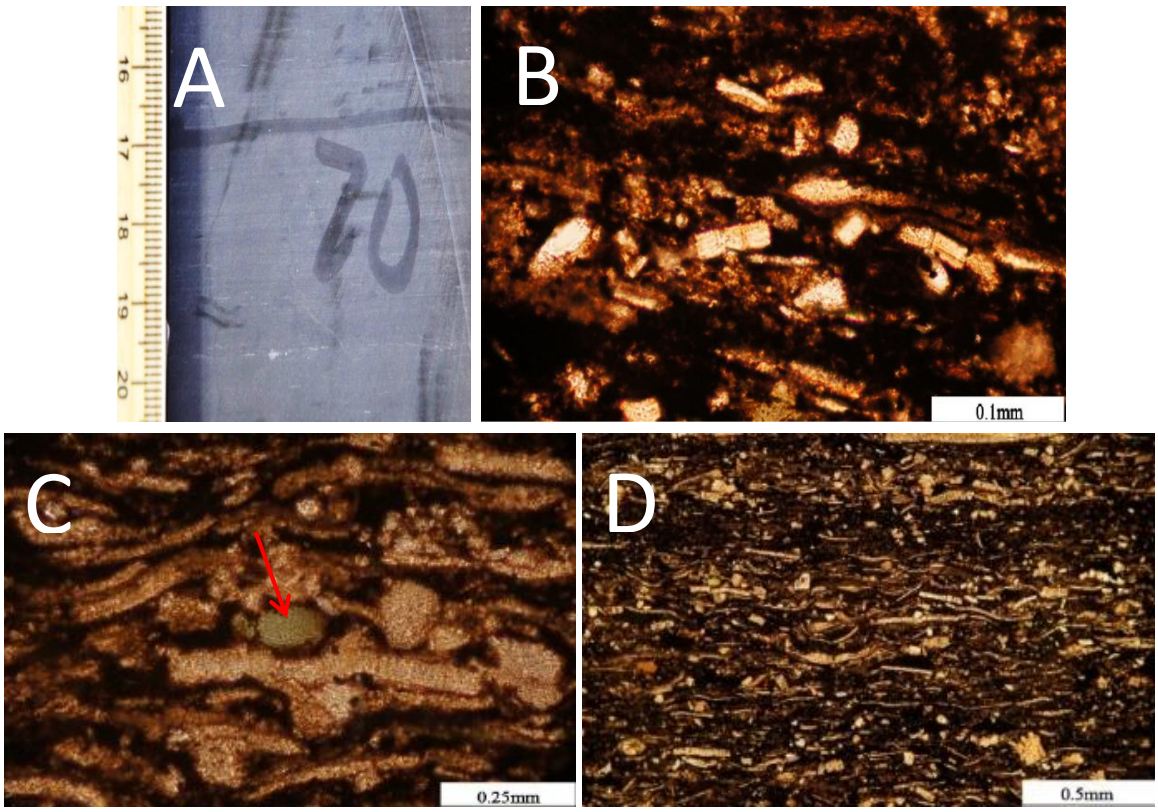

Figure 33: Laminated skeletal calcareous mudstone. A) Core slab showing well-developed laminations. Lake Davis No. 1, 4170.5 ft. Scale in centimeters. B) Rectangular fragment of bivalves. Lake Davis No.1, 4170.5 ft. C) Mixture of glauconite (red arrow) and bivalve fragments. Lake Davis No. 1, 4170.5 ft. D) Interlaminated peloidal layers and bivalve fragment layers. Lake Davis No. 1, 4170.5 ft.

SKELETAL PHOSPHATIC PACKSTONE TO GRAINSTONE

The skeletal phosphatic packstone to grainstone (Figure 34) lithofacies composes only a small fraction of the two cores, but they have a wide distribution in the Barnett section. They commonly exist in the form of thin layers intercalated within the other lithofacies. The layers are generally at the millimeter scale, but they can be as much as several centimeters in thickness. Phosphatic facies are predominantly composed of different types of phosphatic grains (pellets, ooids, coated grains, and intraclasts) (Figure 34A). They have a size range from 0.1 mm to 1 mm, but most are between 100 to 250 micrometers. The varying hues, from light brown to dark brown, may suggest that they formed at different times or underwent different levels of diagenesis. Within these phosphatic layers, subrounded to rounded phosphate grains are dominant and irregular phosphate intraclasts are rare. Large amounts of the phosphatic grains are coated by apatite or pyrite (Figure 34B). Transported accumulations of phosphate grains are common in the two cores. Generally they are interbedded with thick layers of other lithofacies and have sharp contacts with the underlying layers (Figure 34C). Transported phosphatic particles were deposited with bioclasts (e.g. shell fragments and fish bones) and detrital grains (e.g. glauconite). Since most of the phosphatic grain layers are of millimeter scale, they are too thin to show obvious grading. According to the classification of phosphate stratification proposed by Follmi and other researchers (Follmi et al., 1991; Follmi and Garrison, 1991; Glenn et al., 1994), these transported deposits can be classified as allochthonous phosphate. In some cases, a sharp boundary exists between phosphatic ooids layer and an uncemented phosphate layer above (Figure 34D). They are not contemporaneous sediments. The layer

above was transported after the layer below was lithified, because no apparent erosional surface was identified and no gradual change occurred between the two layers.

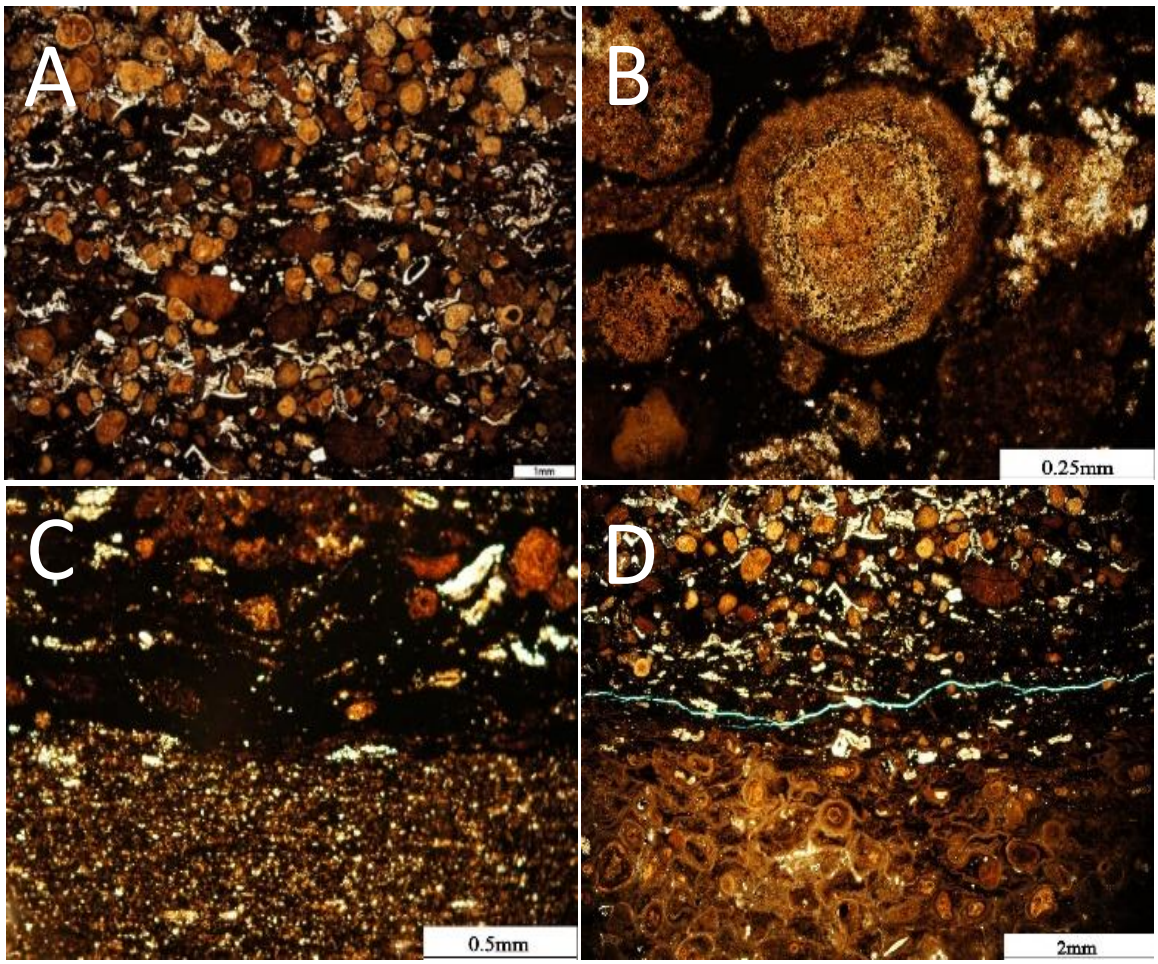

Figure 34: Skeletal phosphatic packstone to grainstone. A) Rounded phosphatic coated grains mixed with peloids and skeletal fragments. Lake Davis No. 1, 4145.5 ft. B) Phosphatic grains showing poorly developed concentric coatings. Lake Davis No. 1, 4145.5 ft. C) Phosphate-rich layer in sharp contact with underlying mudstone layer suggesting an erosional contact. Lake Davis No. 1, 4145.6 ft. D) Sharp boundary between a phosphatic ooids layer and an overlying layer of transported phosphate grains. Lake Davis No. 1, 4140.3 ft.

LITHOSTRATIGRAPHY

Wireline-log correlations (Figure 35) between the two cored wells, which are 12.6 miles apart, have good lateral continuity of lithofacies. Both wells can be divided into four intervals based on wireline gamma-ray curves and core description. In the lowest sections of the cores (Interval I), which represents the time when Barnett deposition began, several cycles of argillaceous/clay-rich siliceous, calcareous, and purer siliceous mudstone are observed. In both cores, Interval I is similar. Upward, the cores display two relatively thicker calcareous beds separated by argillaceous layers (Interval II). These calcareous layers of the two cores were both bounded by thick argillaceous beds that have high API values on wireline logs. However, the difference is that the calcareous beds of Lake Davis No.1 are much thicker than those of Mesquite No.1. These calcareous beds are very distinct and can be considered as marker beds in the middle of the Barnett section. Except for their calcareous matrix, no evidence indicates that this interval is an extension of the Forestburgh Limestone.

As the deposition continued, the sediments became more argillaceous; Interval III is 20 to 30 ft (7 to 10 m) thick and has an increased API value. Within this interval, phosphatic layers can be correlated between the two cores. The identification of abundant phosphatic materials as well as hardgrounds probably indicates a hiatus during this period of time. Overlying Interval III is a much purer siliceous mudstone interbedded with calcareous mudstone (Interval IV). In addition, more carbonate concretions appear in Interval IV.

Between the four intervals, their transitions are easily recognized and correlated, and each interval reflects a similar depositional setting and processes between the two areas. Although the major intervals and wireline-log curves correlate well at the larger scale, the continuity of lithofacies becomes poor at the higher frequency scale of deposition. In addition, the coarser grained skeletal beds, which are interpreted as debris flows, show little correlation, indicating a random triggering mechanism.

As stated before, the Barnett was deposited in a second-order highstand with a depositional depth of more than 450 ft (150 m) throughout its depositional history (Ross and Ross, 1987; Loucks and Ruppel, 2007). The depth of the water was so great that minor sea-level changes did not affect bottom sedimentation. As discussed before, there were several source areas for the Barnett sediments that consisted of different compositions. As a result, any excessive supply from one source correspondingly dilutes the sediments from other sources. Thus, the three transitions of the four intervals probably resulted from the changes in the dominance of the difference sources. As illustrated from the core description (Figure 8), the nonskeletal and skeletal calcareous facies were concentrated in Interval II of the core, which is Early Mississippian. During that time the distance between the southern Fort Worth Basin and the probable clastic source---the Caballos-Arkansas Islands chain---was still too great for that clastic source to dominate. The Chappel platform slope may have dominated sediment input by supplying carbonate sediments, resulting in the calcareous matrix. Transitioning from Interval II to Interval III, Interval III reveals a more terrigenous facies. During this period, the collision between the plates increased rapidly, causing more input of siliciclastic sediments; in the Late Mississippian (Interval IV), purer

siliceous matrix existed because more clastics were transported into the basin because of the closer proximity of the island chain.

Overall, argillaceous/clay-rich siliceous mudstone is the dominant facies in the two cores. Purer siliceous mudstone is concentrated in only the upper interval of the two cores and is less common in the other part of the cores. In the Mesquite No.1, the siliceous brittle zone (clay-rich siliceous and siliceous mudstone) is approximately 70 ft (24 m) thick, but the continuous interval is only 55 ft (18 m) thick. The siliceous zone in the Lake Davis No.1 totals about 90 ft (30 m), but it is also compartmentalized by calcareous mudstones, which made the effective thickness much thinner.

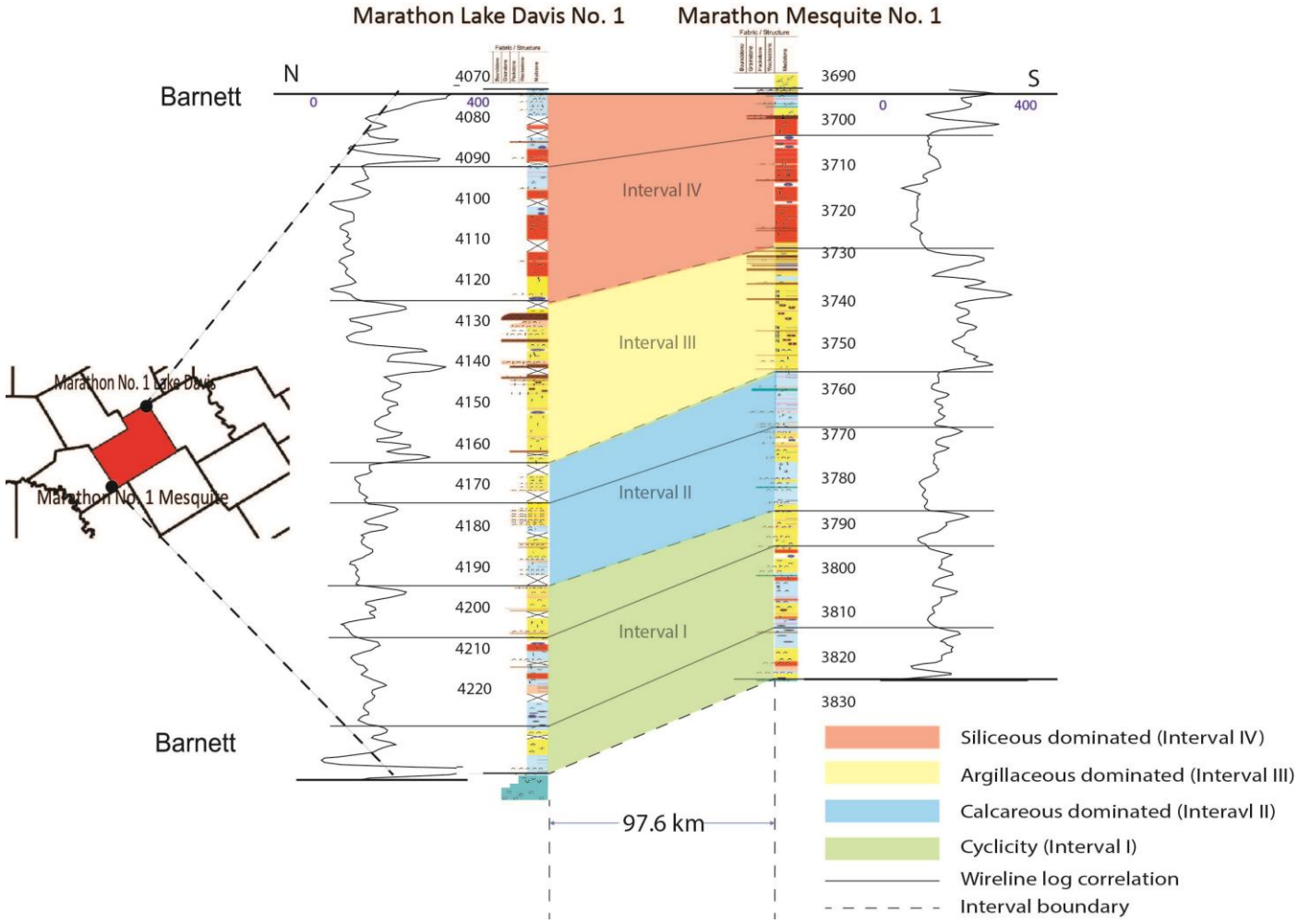

Figure 35: Lithostratigraphy and gamma-ray correlations between the Mesquite No. 1 and Lake Davis No. 1.

INORGANIC GEOCHEMISTRY

More silica residing in the siliceous mineral phase means greater brittleness, which is better for fracturing (Matthews et al., 2007). Therefore, it is useful to analyze the Barnett section to look for the best lithofacies for hydraulic fracturing through examining the amount of silica (as explained below) in each lithofacies.

Ninety-six XRF samples were selected from the Mesquite No.1 core to represent the argillaceous/clay-rich, siliceous, and calcareous facies. Minor lithofacies (skeletal calcareous mudstone and phosphatic grainstone) were excluded. A cross plot of %Si versus %Al distinguishes the three facies in terms of silica excess facies (excessive silica resides in siliceous material), clay-rich facies (normal silica resides in siliceous material), and the diluted-silica facies (insufficient silica in both siliceous material) (Figure 36). According to Rowe (2008), the regression line of argillaceous/clay-rich mudstone defines the trend of aluminosilicates in clay minerals, mostly in illite in this case, so it is termed the illite-silica line. This line represents a standard silica level in the siliceous material. Samples plotting above the illite-silica line suggest silica excess, which means greater brittleness. Samples that fall below the line indicate silica dilution, which in this case is caused by calcareous material.

Figure 36 reveals that the purer siliceous mudstones plot much higher above the illite-silica line. Though both purer siliceous mudstone and clay-rich siliceous mudstone are good for developing fractures according to their high siliceous content shown in XRD data, the former is much better because it has more silica in siliceous material such as

quartz. Significantly, samples from calcareous mudstone plot below the illite-silica line, which indicates their lack of silica.

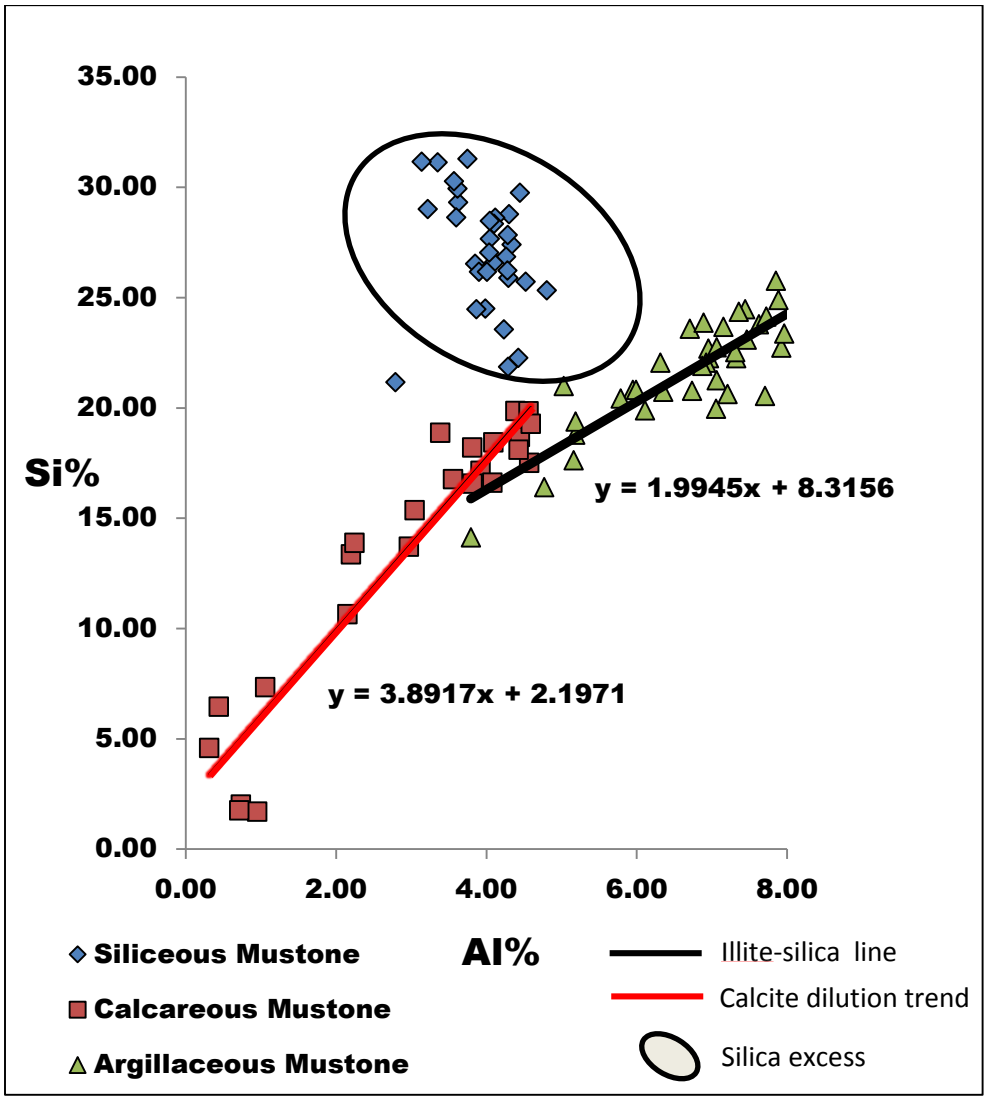

Figure 36: Cross plot of Si% and Al% Samples from argillaceous/clay-rich and calcareous and siliceous mudstone (excluded skeletal-rich facies and phosphatic grainstone) were plotted. This figure displays which lithofacies may be more brittle and better for fracking by comparing the silica content. Data from Mesquite No. 1.

In a mudrock reservoir, TOC is essential for the generation of oil and gas. The relationship between the value of TOC and depositional environment is important because the relationship will provide useful information for exploring new areas with high TOC. Thus, this study also examined the general depositional environments by separating them into aerobic, anoxic, and euxinic conditions and determining the relationships between the three conditions and the preservation of TOC.

A plot of Mo content with depth was generated, accompanied by the normal Mo content in gray shale (Wedepohl, 1971) for comparison (Figure 37). As indicated in the figure, the amount of Mo in Mesquite No.1 is much higher than the average Mo content in normal gray shale, which indicates a general anoxic condition during the deposition of the Barnett.

The DOP_T plot was generated together with the Mo plot for testing the anoxic conditions of the depositional environment (Figure 38). This DOP_T plot also indicates an anoxic condition during most of Barnett time. Under this anoxic environment, the TOC value is persistently high, which may prove that an anoxic condition is favorable for the preservation of TOC. There were only a few periods when the sea water was aerobic ($DOP_T < 0.46$) or euxinic ($DOP_T > 0.75$) with some peaks to the left or right, respectively. For the aerobic periods, they are represented at depths such as 3696-3697 ft. To understand why the peaks occur, the values of DOP_T have been correlated with cores and TOC value. The TOC at the depths between 3696 to 3697 ft. drops from more than 4% to less than 0.5%. In core, this interval corresponds to the nonlaminated skeletal facies, which contains large amount of cephalopods and other shell fragments. The same thing occurs at the depth

interval of 3760.8 ft, where the TOC value drops from 4.1% to less than 0.5%, because of the presence of another debris flow layer. Other values lower than 0.46 also appear along with carbonate-rich layers as well as concretions. The evidence from the core reveals that the input of more calcareous material (much more than the content in calcareous mudstones) will decrease the TOC content rapidly. The excess calcareous material can rapidly change the depositional environment by bringing in a certain amount of oxygen, which accelerated the degradation of TOC. The debris flow is also organic poor because it may have originated from upper slope where is a more anaerobic setting. So generally aerobic environment is adverse for TOC preservation. Noticeably, the presence of concretions cannot be considered as a fact of carbonate material diluting TOC because concretions just prevent the compaction of sediments, and therefore they prevent the TOC from concentrating.

The main interval of DOP_T greater than 0.75 (the euxinic condition) appears from 3755 to 3770 ft, and the lowermost part from 3793 to 3826 ft. The TOC values of the two intervals are approximately 4.5% and 3.5%, respectively. This preliminary test reveals that an euxinic condition is also good for TOC preservation.

Correlations of DOP_T values, and TOC reveals a strong relationship between the two curves, including some of the low values that are caused by large amounts of carbonate input (Figure 39). Overall, the geochemical data show that the Barnett mudstones were deposited in anoxic and euxinic conditions. The TOC curve and its strong correlation with DOP_T values indicate that organic TOC material was well preserved under both anoxic and euxinic conditions, and the TOC value is high throughout the core. The relatively good

preservation of TOC better enables the formation to have the potential to become a shale reservoir. Further organic geochemistry analysis will be presented in next chapter.

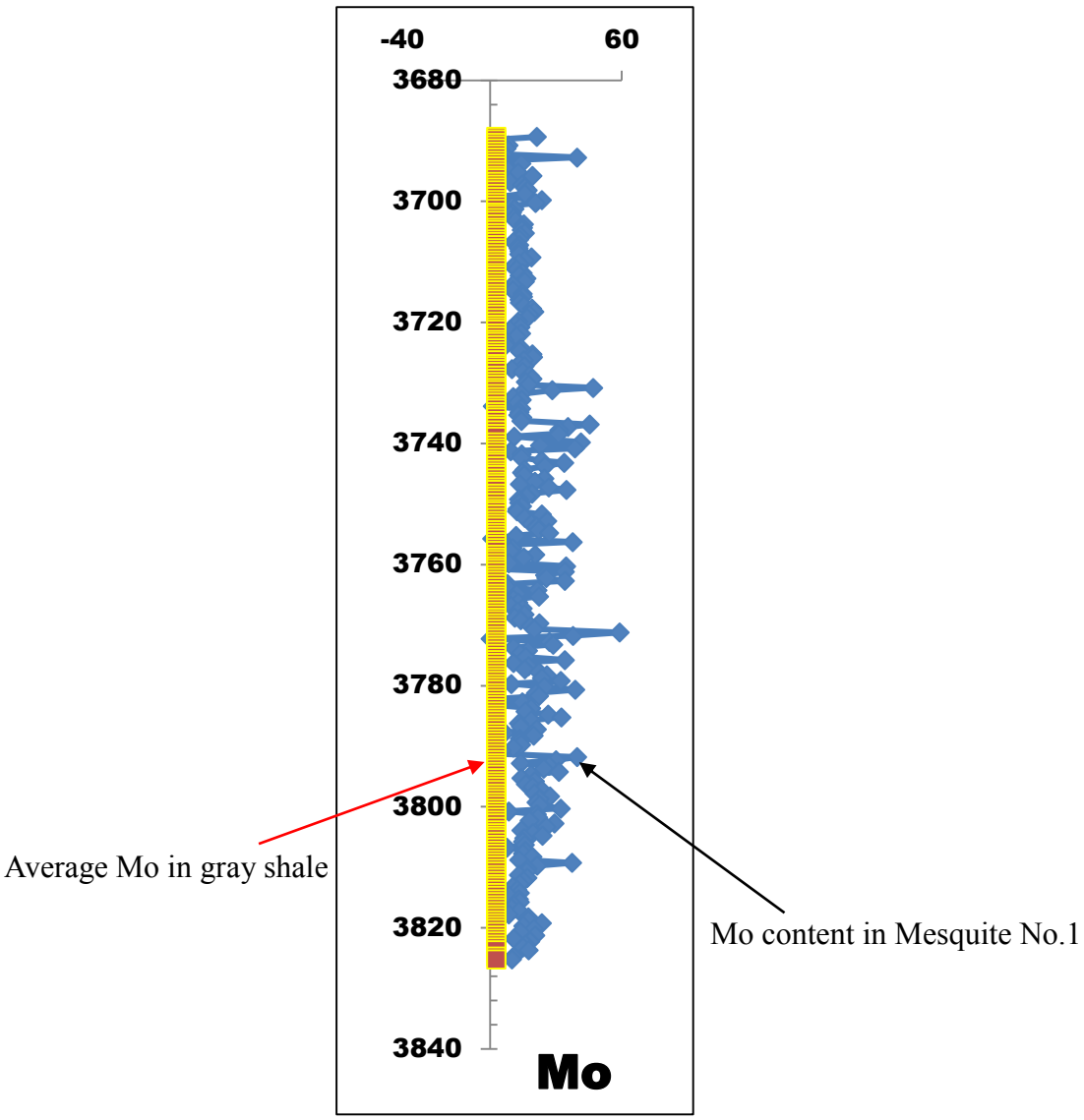

Figure 37: Comparison of Mo content in normal gray shale (Wedepohl, 1971) and Mo content in Hamilton County, data from Mesquite No.1

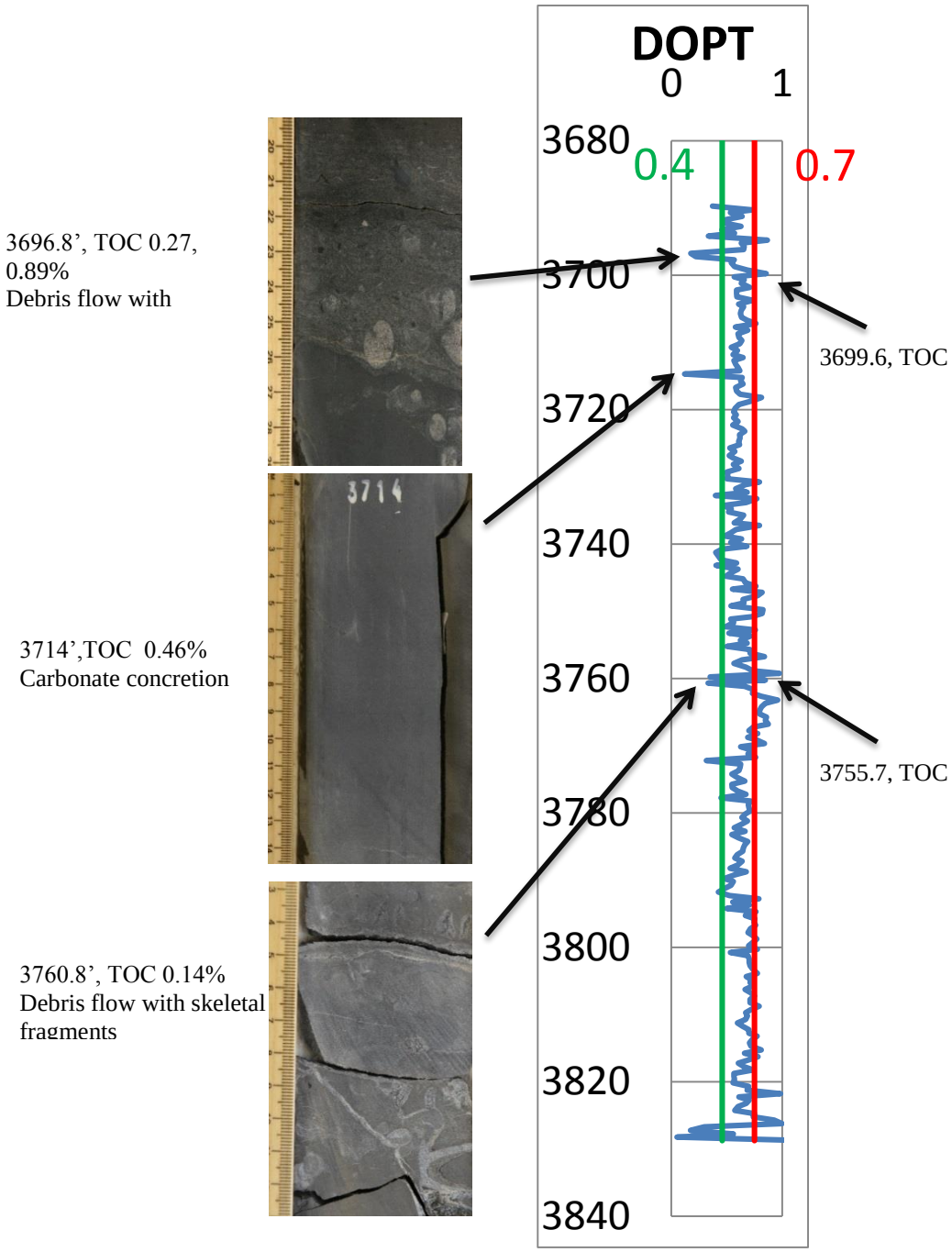

Figure 38: DOP_T is plotted for the Mesquite No. 1 core. Some corresponding core photographs are shown and associated with TOC content.

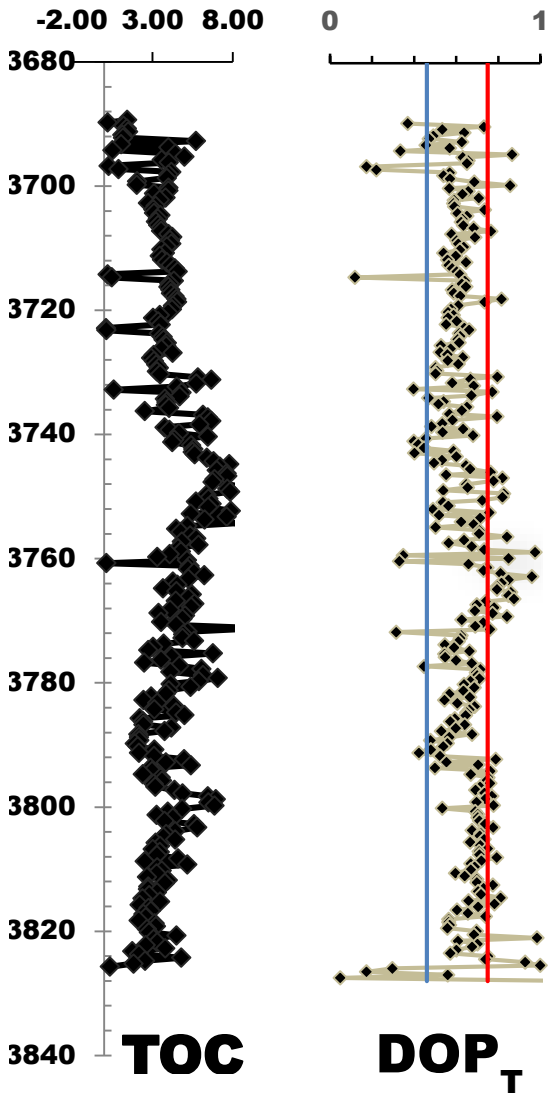

Figure 39: Figure showing there is a strong correlation between DOP_T and TOC, data from Mesquite No.1

ORGANIC GEOCHEMISTRY

TOTAL ORGANIC CARBON (TOC)

This chapter presents the organic geochemistry of this area using pyrolysis analysis of the Mesquite No. 1 core; there is no organic geochemical data from the Lake Davis No. 1, but the difference of geochemical condition between the two cores is probably similar because of the very close distance. The following analysis of organic geochemistry focuses on TOC values and distribution, kerogen type, thermal maturity, and hydrocarbon generation potential.

The Mesquite No.1 core has a mean TOC of 4.05% and a distribution of from 2% to 9% (Figure 40), both of which are similar to the values in the Barnett Formation in the main producing area (Loucks and Ruppel, 2007). The most concentrated interval is from 3.0% to 4.5%. The TOC varies according to the dominant matrix. The argillaceous/clay-rich siliceous mudstone has the highest mean TOC value of the three matrix types, at 4.85%, and TOC values are relatively even and more widely distributed, from 2% to 7%. In siliceous mudstone, the mean TOC is 3.81% (Figure 40). This lithofacies displays a narrower distribution, and most of the values were limited, from 3% to 4.5%. In calcareous mudstone, the mean TOC is 3.85%, and TOC is mostly distributed from 2.5% to 5.5%. The TOC analysis indicates that the three dominant lithofacies all have a high TOC content, which suggests that all the lithofacies can be considered as potential targets for production. However, high TOC alone does not indicate a good shale reservoir, because different

kerogen types generate different hydrocarbons or even no hydrocarbon (Type IV). Thus, an examination of kerogen type is necessary.

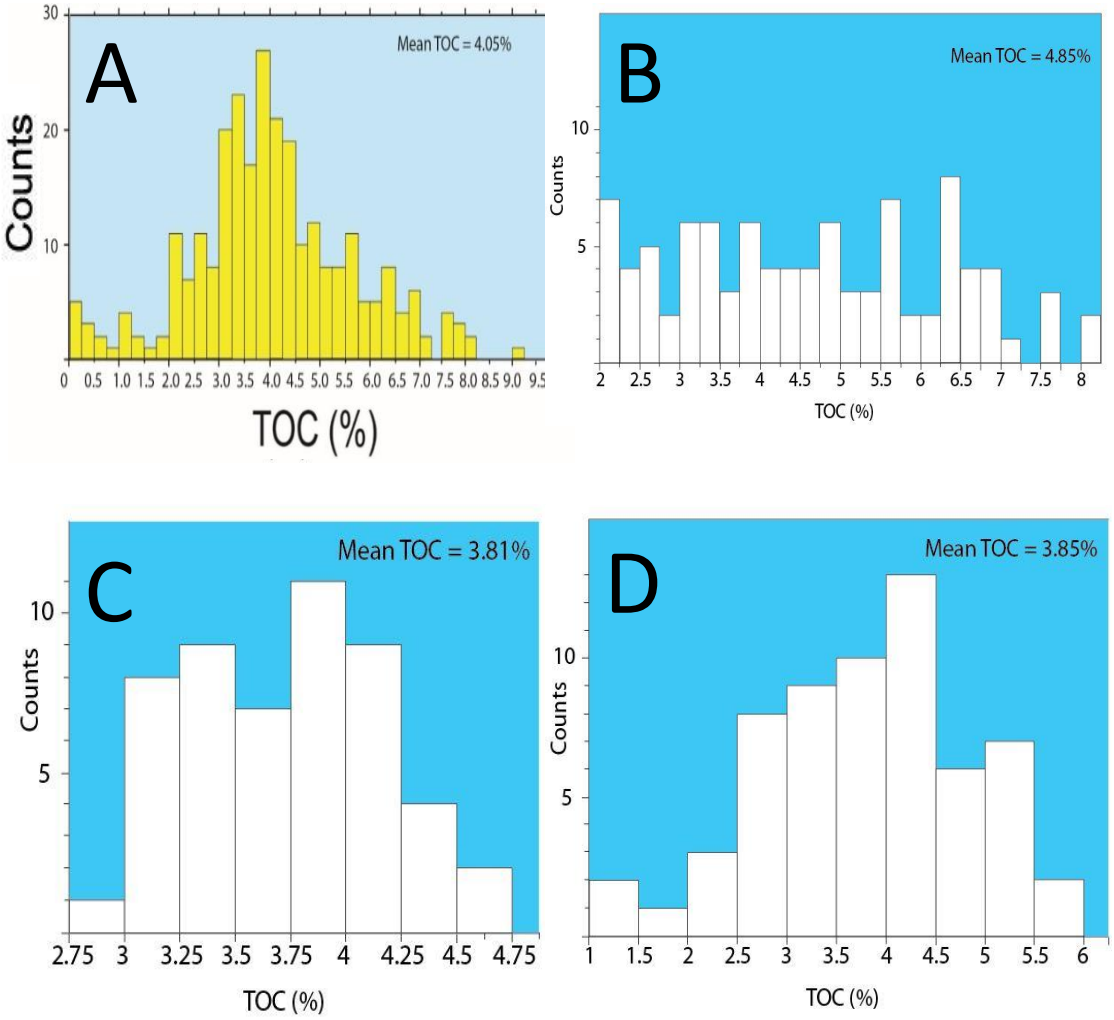

Figure 40: Total Organic Carbon data. A) Histogram of all TOC data from Mesquite No. 1. B) Histogram of TOC data from argillaceous dominated matrix. C) Histogram of TOC data from siliceous dominated matrix. D) Histogram of TOC data from calcareous dominated matrix.

KEROGEN TYPE

In order to distinguish kerogen types, the cross plot of the calculated hydrogen index (HI) and oxygen index (OI) was generated on a Pseudo Van Krevelen plot (Van Krevelen, 1950) to analyze the kerogen types in this area. The results indicate that a mixture of Type II and Type IIS kerogen existed in the core (Figure 41A), both of which are oil-prone. The Type II and Type IIS kerogen has the same kerogen structure, and the only difference is the sulfur content. The special Type IIS kerogen is characterized by high initial H/C and low initial O/C ratios (Orr, 1986). Their low oxygen index is caused by the substitution of oxygen by large amount of sulfur. According to Dinur et al. (1981) and Orr (1986), Type II and Type IIS have a similar depositional environment, but Type IIS can be only formed in environments where clastic sediments are poor and sulfate reduction activity is extremely strong near the sediment/water interface. In the Barnett section, the active iron in abundant clastic material can remove the sulfur in the form of iron sulfides (e.g., Gransch and Posthuma, 1974; Dinur et al., 1981). It is also important to note that none of the published geochemical papers have supported the hypothesis that there was abundant Type IIS kerogen in the Barnett (e.g., Jarvie et al., 2005; Zhang et al., 2014). In addition, the cross plot of the hydrogen index versus T_{max} was also generated to aid the geochemical interpretation (41B). The plot shows that the samples were adjacent to the Type II kerogen curve. Incorporating the information above, and also in consideration of the fact that for high maturity material, it is difficult to differentiate the kerogen type in such a narrow area on the hydrogen index versus oxygen index plot, thus a Type II Kerogen is suggested. Given that this was a marine depositional environment, Type II kerogen

appears in the form of marine snow or organic aggregates that migrated downward by pelagic settling, and this is consistent with the depositional model proposed by Loucks and Ruppel (2007). Type III kerogen also is present, though it does not appear on this plot, as identified under the microscope and in core. In thin section, organic matter appears as organic flakes because of compaction, and it is difficult to differentiate Type II from Type III except in the uncompacted fabric.

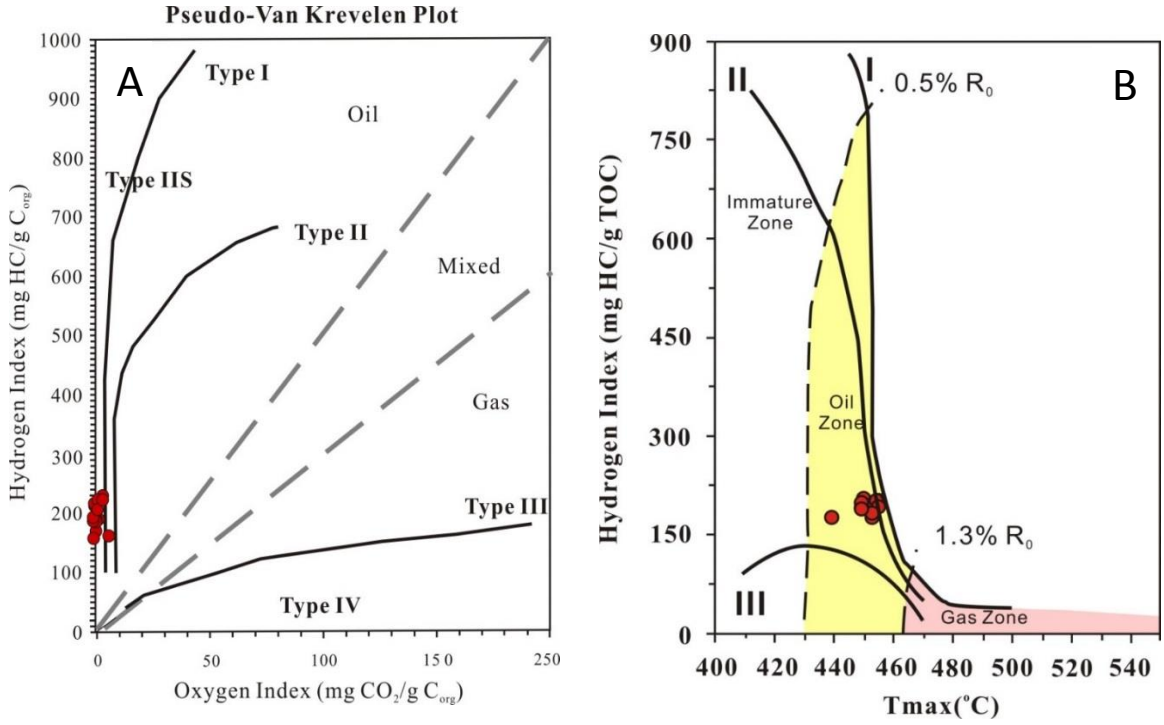

Figure 41: Kerogen type. A) Pseudo Van Krevelen plot, modified from Dembicki (2009). It is important to note that the samples have a mean R_o range of 0.94% indicating that samples have undergone thermal maturation and their original composition as evolved. Data from Mesquite No. 1. B) Plot of hydrgen index versus T_{max}, modified from Zhang et al. (2014). The combination of two figures shows Type II kerogen is dominant. Data from Mesquite No.1.

THERMAL MATURITY

Vitrinite reflectance (R_o) was calculated according to the method of Jarvie et al. (2001), who used a series of coefficients to derive R_o from Tmax. The distribution of R_o shows a mean value of approximately 0.94%, which is within the oil window. The total distribution of R_o is from 0.7 % to slightly more than 1.1% (Figure 42), all of which is still within the oil window. It can be concluded that this thermal maturity meets the requirement for oil generation.

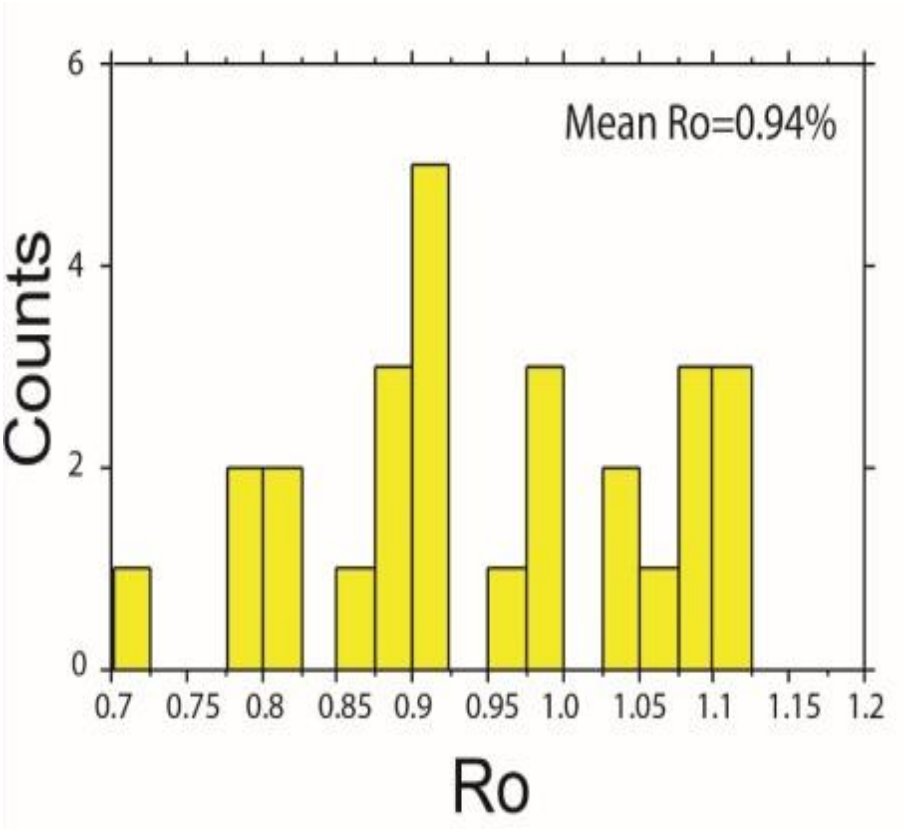

Figure 42: Histogram of thermal maturity (calculated R_o from RockEval). Data from Mesquite No. 1.

HYDROCARBON GENERATION POTENTIAL

In addition, a Dembicki plot (Dembicki, 2009) was created to examine the potential of hydrocarbon generation (Figure 43). This plot considered both TOC and pyrolysis results. Both S2 (generated hydrocarbon in the pyrolysis experiment) and S1+S2 (pre-existing and generated hydrocarbons) are considered in this plot. The plot reveals that the Barnett rocks in this area have an excellent potential for generating hydrocarbons, regardless of whether results are plotted with S2 alone or with S1+S2.

Results of organic geochemistry analysis clearly show that the Barnett Formation in Hamilton County is a good source rock for generating hydrocarbons, having a mixture of large amounts of Type II kerogen and very small amounts of Type III kerogen. The TOC content, which is approximately 4%, is similar to that in the main producing area. Within the different lithofacies, the mean TOC contents are also very similar, which indicates that all intervals of the Barnett Formation are organic rich. They show an average thermal maturity of 0.94 %, which puts the section within the oil window. Thermal maturity may also have a significant impact on pore types (as will be discussed in next chapter), and overall reservoir quality.

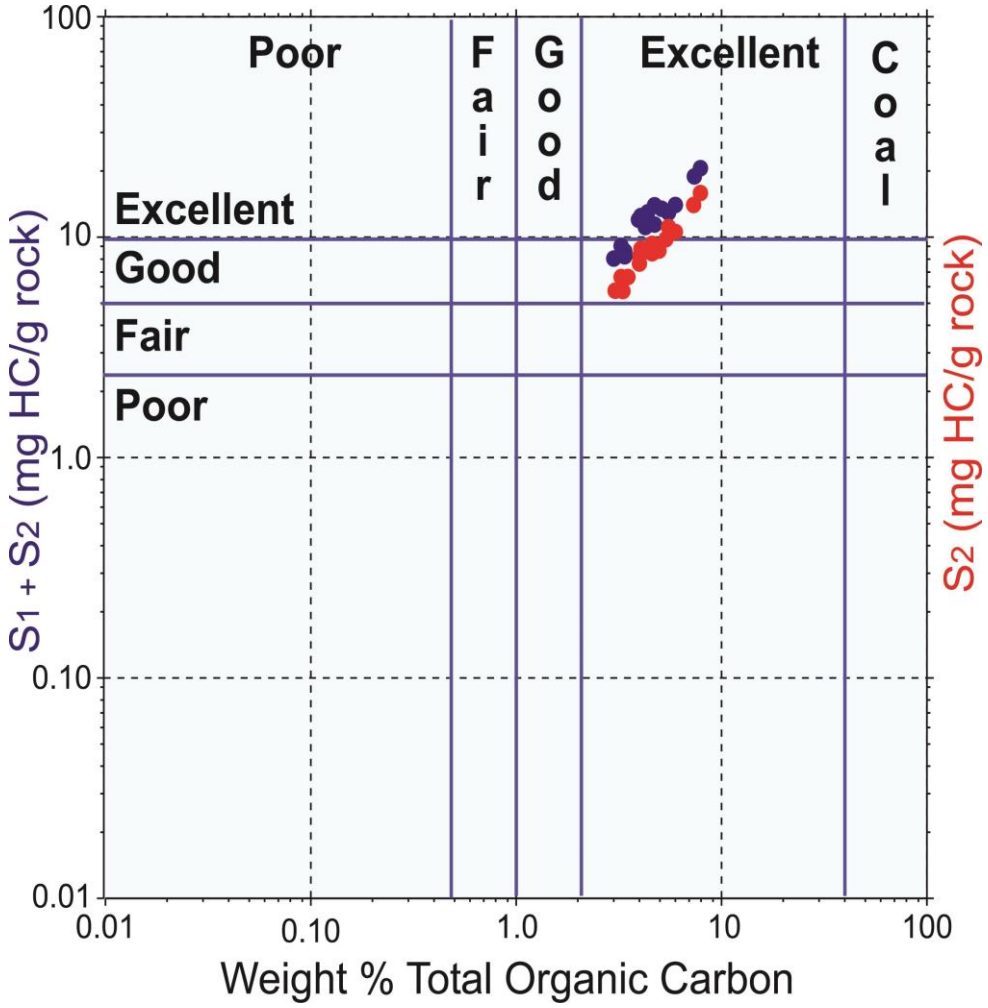

Figure 43: Dembicki plot showing hydrocarbon generation potential. See Dembicki (2009) for details. Data from Mesquite No. 1.

PORE TYPES

The study of pore types and associated pore networks are important to understanding the reservoir quality of mudrock reservoirs, as well as the relationship between the storage of the oil and gas and the pore networks .

In the Barnett Formation, the pores are largely nanometer- to micrometer-size pores that cannot be observed using a standard petrographicmicroscope (Loucks et al. 2009, 2012); therefore, the use of Ar-ion milling preparation and an field scanning electron microscope was required in this study. Compared with other polishing methods, Ar-ion milling generates a smoother surface with fewer artifacts that allows the observations of nano- and micropores (Loucks et al., 2009).

The classification used in this study is based on the work by Loucks et al. (2012), who proposed a classification of mudrock pores including two mineral-related pores, which are interparticle pores and intraparticle pores, and one organic-matter-related pore type, for the pores within organic matter.

INTERPARTICLE PORES

Interparticle pores are the pores that occur between particles and crystals (Loucks et al., 2012). They are very uncommon in the Barnett mudstones in the study area. In the samples, interparticle pores are generally angular to subangular, and they are commonly much larger than other pore types. The subangular interparticle pores, which range from <1 micrometer to 2 micrometers in size, were observed dispersed within the matrix (Figure 44A). Other interparticle pores (grain-edge pores) are more elongated and are largely

formed around the rim of rounded rigid minerals such as quartz and pyrite (Figure 44B). Most of the original interparticle pores were destroyed by early compaction (Rieke and Chilingarian, 1974).

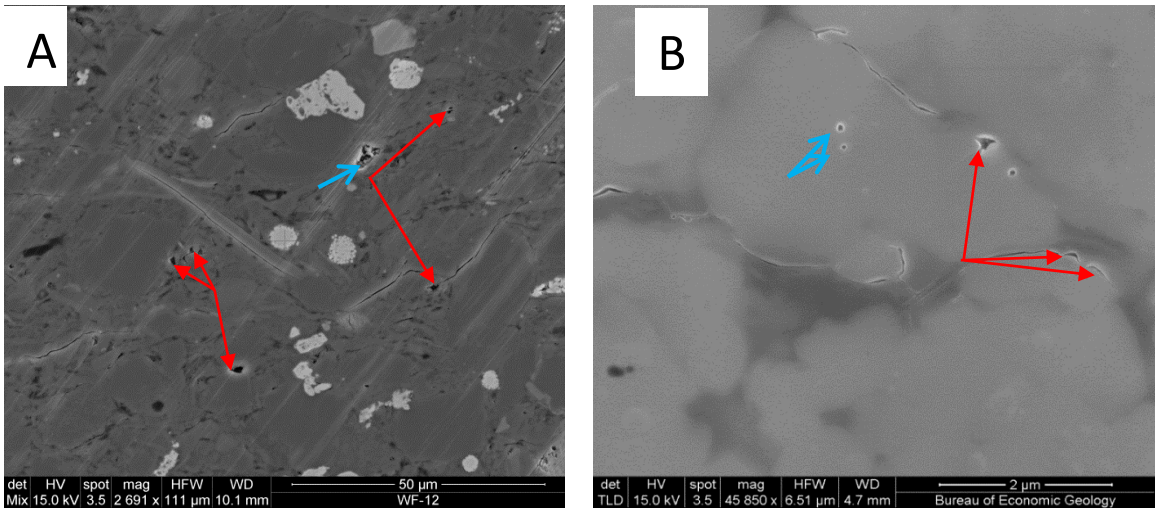

Figure 44: Example of interparticle pores. A) Interparticle pores highlighted by red arrows. Blue arrow shows dissolution pores. Lake Davis No. 1, 4204 ft. B) Interparticle pores highlighted by red arrows. The blue arrows indicate intraparticle pores. Lake Davis No. 1, 4188 ft. det = detector; HV = high voltage (accelerating voltage); spot = spot size; mag = magnification; HFW = horizontal frame width; WD = working distance.

INTRAPARTICLE PORES

Intraparticle pores are very common in this Barnett section. They commonly occur within clays and large mineral grains such as albite and calcite. According to Loucks et al. (2012), many intraparticle pores are destroyed by compaction or have been filled with cement, but some were formed by corrosive fluid dissolution. They are generally angular to subrounded and have no preferential orientation. The intraparticle pores associated with albite and calcite are commonly produced by partial dissolution (Figure 45A) or by fluid inclusions (Figure 45B). Fluids trapped in crystal during growth will produce bubbles in the crystal. These inclusions will form isolated intraparticle pores that can be as small as hundreds of nanometers.

Clay-associated intraparticle pores are abundant. The pores are generally elongated and parallel to the direction of the clay palettes. These are interpreted as cleavage-related pores, which are generally controlled by the internal sheet structure within clay minerals, and they can be opened by compaction (Figure 45C).

Intercrystalline pores are also common within pyrite framboids, and they are considered as intraparticle pores (Figure 45D). These pores occupied the space between crystals that composed the pyrite framboid. In the study area; the extensive occurrence of pyrite makes this type of pore one of the dominant pore types in these mudrocks.

In the samples studied in this work, there are other intraparticle pores. Fossils that were composed of calcite show minor amounts of dissolution intraparticle pores within the tests (Figure 46C). Also, micas with cleavage-related intraparticle pores were also observed in the samples (Figure 46D). These pores are elongate and developed along the cleavage

of micas. The intraparticle pores are enhanced by dissolution of the mica and some of the pores are filled by crystals of other minerals.

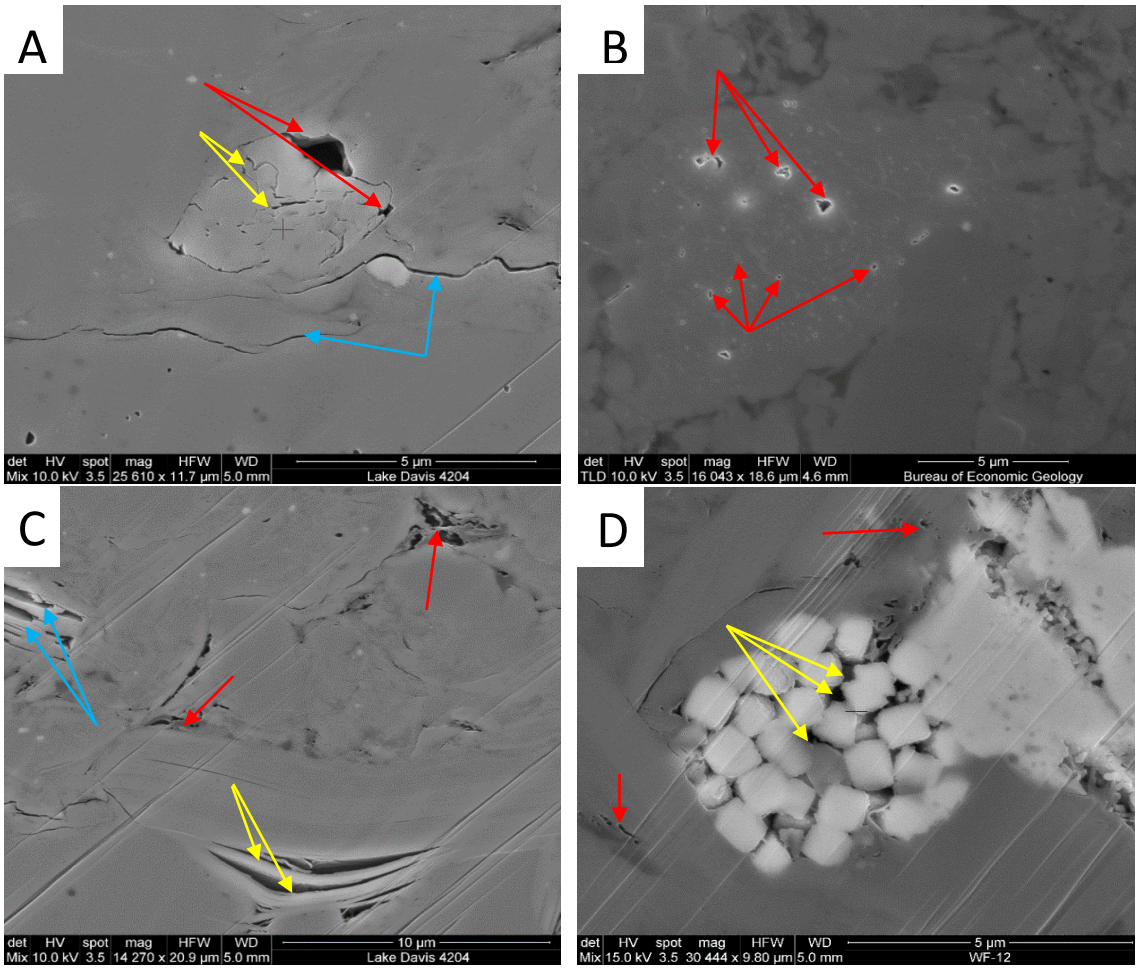

Figure 45: Example of intraparticle pores. A) Intraparticle pores that formed by partial dissolution around the rims (red arrows). Blue arrows indicate artifacts. Yellow arrows indicate pores within the albite crystal caused by dissolution. Lake Davis No. 1, 4204 ft. B) Fluid inclusion intraparticle pores (red arrows) within a calcite grain. Lake Davis No. 1, 4204 ft. C) Cleavage-related intraparticle pores (yellow arrows) within a clay mineral. Blue arrows indicate intraparticle pores in mica caused by dissolution. Red arrows indicate organic pores. Lake Davis No. 1, 4204 ft. D) Abundant intraparticle pores (yellow arrows) within a pyrite framboid. Red arrows show organic matter pores. Lake Davis No. 1, 4204 ft. det = detector; HV = high voltage (accelerating voltage); spot = spot size; mag = magnification; HFW = horizontal frame width; WD = working distance.

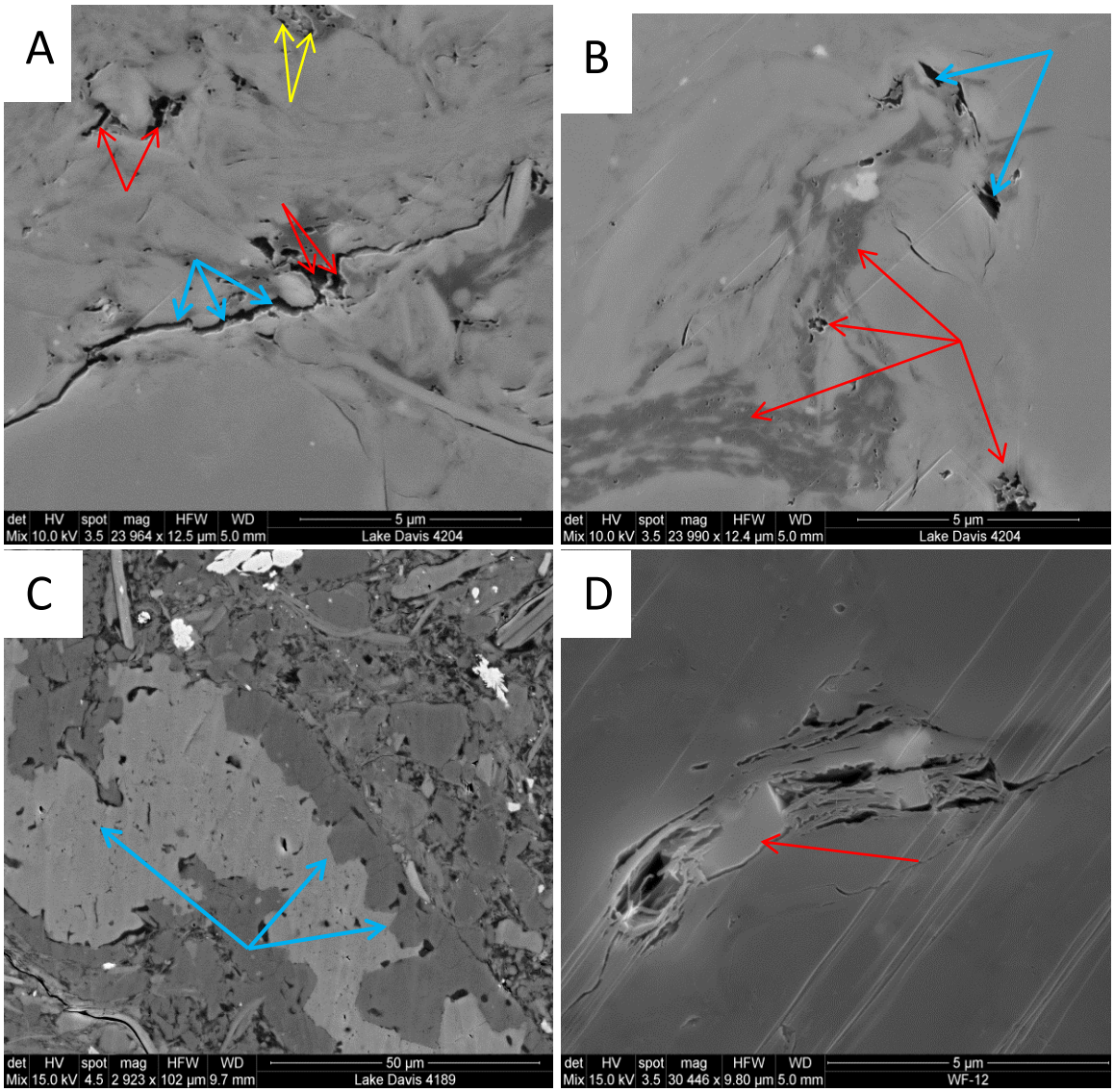

Figure 46: Examples of intraparticle pores and organic matter pores. A) Large organic matter pores that may be bubbles resulting from a two-phase inclusion (indicated by red arrows); blue arrows point to artifacts; yellow arrows show OM pores. Lake Davis No. 1, 4204 ft. B) Organic matter pores of various sizes (red arrows). Blue arrows indicate clay minerals undergoing dissolution. Lake Davis No. 1, 4204 ft. C) Intraparticle pores within a shell fossil (indicated by blue arrows). Lake Davis No. 1, 4189 ft. D) Dissolution intraparticle pores probably within a mica grain with crystals growth in them (red arrow). Lake Davis No. 1, 4204 ft. det = detector; HV = high voltage (accelerating voltage); spot = spot size; mag = magnification; HFW = horizontal frame width; WD = working distance.

ORGANIC MATTER PORES

Organic matter pores (OM) are the most abundant pore type in this Barnett section, and they are also the most common pore type in the Barnett Formation (e.g., Loucks et al. 2009). As the organic matter was buried and thermally matured, OM pores were generated (Loucks et al., 2009). Because the mean R_o is 0.94 %, OM pores are expected. As seen in the samples, the OM pores are very small, ranging from 20 to 60 nm in diameter. Their shapes can be angular (triangular or polygonal), rounded, or elliptical (Figure 47D). Some samples show connected organic matter pores within a single type of organic matter, as reflected by their various pore depths and tortuosities (Figure 47A). The porosity in different organic matter varies significantly from zero percent (Figure 47C) to more than 20 percent. Larger organic matter pores can have consumed much of the organic matter particle (Figure 46A). Loucks and Reed (2014) suggested that this type of pore was formed by two-phase hydrocarbon inclusions. They explained that the bitumen first migrated into the pore; then the fluid or gas in the bitumen bubble escaped and left a large pore (Loucks and Reed, 2014).

The size of the OM pores varies significantly but the controlling factors have not been well studied, however, it is known to be associated with the thermal maturity. As the temperature and thermal maturity increases, pores begin to form in the organic matter. When large amounts of pores form, they begin to coalesce with each other and form larger pores. Aligned organic matter pores which were thought to be controlled by inherited structure in the organic matter (Loucks et al., 2009) were not seen in these samples.

However, as observed in these Barnett samples, the thermal maturity in this area is high enough to generate large amounts of organic pores.

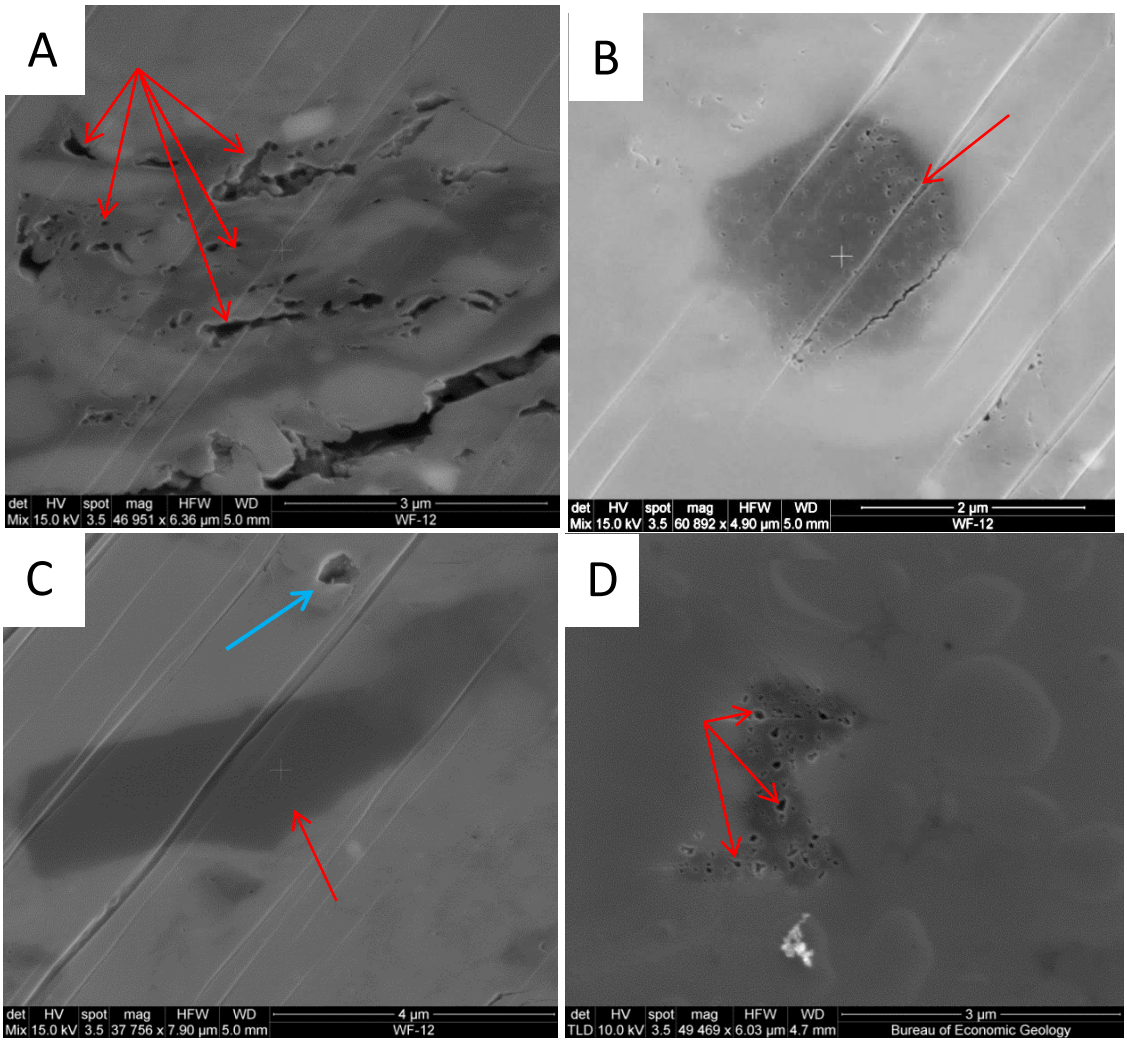

Figure 47: Examples of organic matter pores. A) Organic matter pores of various sizes. Red arrows point to organic matter pores that appear to show three dimensional connectivity. Lake Davis No. 1, 4204 ft. B) Organic matter with numerous small rounded OM pores. Lake Davis No. 1, 4204 ft. C) Some organic matter (red arrows) do not display pores. Blue arrow indicates a dissolution intraparticle pore. Lake Davis No. 1, 4188 ft. D) Organic matter with many pores. Lake Davis No. 1, 4204 ft. det = detector; HV = high voltage (accelerating voltage); spot = spot size; mag = magnification; HFW = horizontal frame width; WD = working distance.

DISCUSSION

LITHOFACIES AND DEPOSITIONAL PROCESSES

According to Loucks and Ruppel (2007), based on their study of four cores in northern Fort Worth Basin, the dominant depositional processes were pelagic and hemipelagic settling, turbidity currents, debris flows, and bottom-current reworking. Based on this study in Hamilton County, the same dominant depositional processes occurred in southern Fort Worth Basin.

Hemipelagic settling processes are characterized by both vertical settling and low lateral advection caused by river plumes and other water currents (Stow and Tabrez, 1998; Stow et al., 2001). In the Barnett, sediments deposited by hemipelagic settling contain a mixture of biogenic and terrigenous material that involves the presence of silt-sized detritus such as quartz silts and clay-sized minerals. These terrigenous materials that were deposited by hemipelagic settling may come from aeolian dust and nepheloid flows (Wignall, 1994), and this is also inferred by Bunting (2007) based on his study of the Barnett Formation in Johnson County.

Unlike the two forces (vertical and lateral forces) that acted on hemipelagic settling in different directions, pelagic settling is a process of only vertical settling, by which very fine-grained sediments in the water column such as clay minerals and marine snows settle to the seafloor (Stow et al., 2001) without the effect of lateral water plumes. In the Barnett, fecal pellets of zooplanktons and marine snow were probably the most important sediments deposited by pelagic settling. Marine snow is characterized by those suspended aggregates

that are larger than 500 microns and are composed of organic detritus, microorganisms, and clay minerals (Alldredge and Silver, 1988). Algal-secreted mucus-producing marine organisms and biologically enhanced aggregation of smaller component particles (peloids) of pelagic biota are the two most important contributors to the origin of marine snow (Alldredge and Youngbluth, 1985; Alldredge and Silver, 1988). Boggs (1987) also indicated that the flocculation of clay minerals could form peloids in the water column. Except for the marine snow related peloids, zooplankton fecal pellets could also sink rapidly from the water column (Turner, 2002).

The above types of peloids as well as those peloids transported from the slope all contribute to the peloidal texture of the Barnett mudstones. More evidence for pelagic settling is the large amount of Type II marine kerogen. This algal-rich kerogen is considered to be derived from basin upwelling (Gutschick and Sandberg, 1983), which caused algal blooms. As discussed earlier, algal bloom is one of the main contributors to marine snow. The abundant Type II organic flakes can be interpreted as compacted marine snow.

Long-duration and persistent hemipelagic and pelagic settling of mud throughout the deposition of the Barnett is evidenced by fine-grained sediments including detrital quartz and clay minerals occurring in all of the lithofacies, laminations as seen in the siliceous mudstone, and the large amounts of TOC and peloids that are abundant throughout the mudstones.

Turbidity currents are recorded as dilute turbidites. In many cases, no complete Bouma sequences can be identified, and only the fine-grained D and E units are deposited

This is consistent with the conclusions of Loucks and Ruppel (2007), who interpreted that the lack of a complete Bouma sequence is the result of long-distance transportation from the sediment source, during which coarser material was deposited first and the finer material was deposited in the distal part of the basin.

Debris flow is described as a gravity-driven process with poorly sorted sediments coming down to the basin from the slope (Iverson, 1997). In core, although the sediments might have been reworked after deposition, the direct evidence of debris flows is nonlaminated skeletal calcareous mudstone and part of the phosphatic grainstone, because transported bioclasts such as mollusks and brachiopods, phosphate, and carbonate intraclasts as well as fine-grained material are commonly mixed. Loucks and Ruppel (2007) suggested that the mollusks and brachiopods originated from the dysaerobic slope. Though the nonlaminated shell layers were interpreted as the results of debris flow, in several cases in the Hamilton County area, these debris layers are all simply composed of coarse materials. (Figure 32B). Only rare carbonate mud and other finer skeletal materials are present. This phenomenon can also be interpreted by the model of long-distance transportation that was mentioned above. The coarse shell fragments presented here are equivalent to those coarse materials that deposited first during the transportation; the absent of silt-sized or finer materials in these coarse shell layers were transported further down into the basin. Several researchers described the process as a transition process from a debris flow to a low-density turbidity flow (Hampton, 1972; Mulder and Alexander, 2001). Combining this theory (Hampton, 1972; Mulder and Alexander, 2001) with evidence seen in core, the process can be described as:

1) Debris flows that involved bivalves, brachiopods, crinoids, and other intraclasts were triggered on the slope;

2) As the flows travelled into the basin, the lack of confinement and reduced velocity caused coarse shell fragments to be deposited first;

3) Finer materials stayed suspended and was further transported as water-suspended load;

4) Finer materials were finally deposited in the distal part of the Fort Worth Basin as low-density turbidites as incomplete Bouma sequences.

In some cases, the interbeddings of nonlaminated skeletal layers (coarse skeletal debris) and a series of well-sorted silt-sized skeletal layers (finer debris of skeletal and peloids) indicate that the turbidity currents and debris flows alternated. In normal situations, they should have been deposited in different places laterally. The presence of interbedding suggests that the source that triggered the debris flow events migrated and those sources had different relative distances to the site of deposition.

Within the Barnett, bottom current reworking is also a significant depositional process (Hickey and Henk, 2007; Loucks and Ruppel, 2007; Abouelresh and Slatt, 2011). Unlike the other depositional processes, bottom-current reworking involves sediments that were already deposited and later resedimented. Aided by the Coriolis force that acted on the western margins of the basin, bottom currents can move relatively fast, at 10-20 cm/s, and sometimes they can locally exceed 100 cm/s and 200m/s (Stow, 2002). With such a high speed, Stow et al. (2002) think it is possible for these strong currents to transport a wide range of grains, from clay to fine-sand. In Hamilton County area, the bottom-current

reworking created the widely extended low-angle starved ripples that formed on the seafloor. The ripples are mostly composed of silt-sized to sand-sized carbonate materials. In phosphatic facies, the coated phosphatic grains and ooids formed with the aid of bottom-current reworking, which scoured, reworked, and reburied the grains (Pufahl and Grimm, 2003), so that new rims of phosphate could form on the grains. Commonly the contacts between silt-rich and mud-rich layers are not sharp. These phenomena may imply the occurrence of bottom-current reworking, which obscured the contacts between low-density turbidites and made them gradational. On the other hand, winnowing processes induced by bottom currents (Stow et al., 1998) can winnow out mud and other small uncemented allochems because of their low lithification rate as compared to the lithification rate of phosphate (Trappe, 1998). This process gave rise to the formation and accumulation of well-sorted phosphatic grains.

DEPOSITIONAL ENVIRONMENT

According to the inorganic geochemistry presented in this thesis, the Barnett was deposited in an anoxic to euxinic condition with high enrichment of Mo in the study area. However, as we have stated above, agglutinated foraminifera are widely observed in almost all the lithofacies in the Barnett Formation. On the basis of this fact, some researchers indicate that the sea water during deposition was not totally out of oxygen because agglutinated foraminifera require at least some oxygen to live in generally oxygen-deficient environments (Bernhard and Reimers, 1991; Bernhard et al., 2003; Schieber, 2009). However, based on the study in this thesis, most of the agglutinated foraminifera were

concentrated and parallel to the bedding indicating that they have been transported from the dysaerobic slope environment. Wiggins (1982) also suggests that most of the calcareous material on the seafloor of Barnett is transported allochems since no in-situ biota exists. Both of these lines of evidence indicate that most of the agglutinated foraminifera were transported to the basin from a dysaerobic slope setting by debris flow.

Although most of the agglutinated foraminifera were transported to the basin, some may have lived for a short time in the anoxic/euxinic area under some certain conditions. As discussed above, the sediment gravity-flow is a short-lived, relatively high-energy event deposit. It is possible that the oxygen associated with the current could have allowed for a bloom of short-lived foraminifera. The transported biota that may have lived in such a severe condition for a short time are termed doomed pioneers (Follmi and Grimm, 1990). However, no burrowing developed in association with these oxygenated waters (or strong bottom currents later destroyed them).

RESERVOIR QUALITY

The TOC distribution (Figure 40) and the Dembicki plot (Figure 43) suggest that all three dominant facies have high TOC and offer excellent hydrocarbon generation potential. And the excellent potential can be translated to oil, for the reasons given below. The pseudo Van Krevelen plot and core data show that there is much more Type II than Type III kerogen, which indicates an oil-prone source rock. Vitrinite reflectance shows that the thermal maturity is within the oil window, with an average of 0.94%. Both data reveal that this area is a highly potential shale reservoir.

According to the study conducted by Papazis and Milliken (2005), biogenic quartz is the dominant mineral in the Barnett that caused its high brittleness. The results from the Si% versus Al% plot (Figure 36) can also prove the great abundance of biogenic silica in siliceous mudstone in the southern Fort Worth Basin. In addition, XRD analysis shows a pattern of mineral distribution in a ternary plot that is similar to Loucks and Ruppel's (2007) study of the main producing area of the Barnett (their figure 10).

Concentrating on the siliceous mudstone, the Barnett section in the southern area has a slightly higher content of carbonate material and a similar content of clay with the northern area. In terms of the TOC of two types of siliceous mudstones, though there is a 1% difference in TOC, they are all high enough for producing. A major problem is that the siliceous interval may be too thin to be commercially produced.

This study also suggests that organic matter pores are the most abundant pore type. Intraparticle pores are also abundant in the core, but this type of pore does not contribute to the effective porosity. Interparticle pores, which is another effective pore type, are rare in the Barnett samples. Just as the organic matter pores predominate in the main producing area (Loucks et al., 2009), these organic matter pores in the southern Fort Worth Basin can serve the same function, which is to supply storage space for oil and gas and provide pathways for production.

CONCLUSIONS

The conclusions of this study are that five dominant lithofacies were identified from the two cores in the Barnett Formation, in the southern Fort Worth Basin. They are 1) laminated silty clay-rich peloidal siliceous mudstone; 2) laminated skeletal silty peloidal siliceous mudstone; 3) nonlaminated silty peloidal calcareous mudstone; 4) laminated and nonlaminated skeletal calcareous mudstone; and 5) skeletal phosphatic packstone to grainstone. Pelagic and hemipelagic settling, debris and turbidity flows, and bottom-current reworking are the dominant depositional processes, and their interaction along with biota production defined the lithofacies of the Barnett Formation. The deposition environment of Barnett in the southern Fort Worth Basin was anoxic and euxinic with periods of overtuning.

Although these two wells were not productive, the area has several good parameters that would favor production, such as 1) high TOC that has excellent potential to generate oil and gas (mainly Type II organics); 2) brittle siliceous mudstone that is favorable for hydraulic fracturing; 3) thermal maturity values suitable for generation of oil; and 4) development of abundant organic matter pores. The sole limitation to economical oil production in this area is the thinness of the Barnett mudstone.

APPENDIX A

Table A1: Thin-sections used in this study

Thin Section	Core	Depth (ft)	Orientation	Formation
LDTS-001	Lake Davis No.1	4073.5	Vertical	Penn Detrital
LDTS-002	Lake Davis No.1	4076.4	Vertical	Barnett
LDTS-003	Lake Davis No.1	4076.5	Vertical	Barnett
LDTS-004	Lake Davis No.1	4078.2	Vertical	Barnett
LDTS-005	Lake Davis No.1	4081.8	Vertical	Barnett
LDTS-006	Lake Davis No.1	4087.0	Vertical	Barnett
LDTS-007	Lake Davis No.1	4095.2	Vertical	Barnett
LDTS-008	Lake Davis No.1	4098.8	Vertical	Barnett
LDTS-009	Lake Davis No.1	4104.1	Vertical	Barnett
LDTS-010	Lake Davis No.1	4113.2	Vertical	Barnett
LDTS-011	Lake Davis No.1	4115.9	Vertical	Barnett
LDTS-012	Lake Davis No.1	4116.6	Vertical	Barnett
LDTS-013	Lake Davis No.1	4128.4	Vertical	Barnett
LDTS-014	Lake Davis No.1	4129.5	Vertical	Barnett
LDTS-015	Lake Davis No.1	4134.2	Vertical	Barnett
LDTS-016	Lake Davis No.1	4137.7	Vertical	Barnett
LDTS-017	Lake Davis No.1	4139.9	Vertical	Barnett
LDTS-018	Lake Davis No.1	4140.1	Vertical	Barnett
LDTS-019	Lake Davis No.1	4141.2	Vertical	Barnett
LDTS-020	Lake Davis No.1	4141.5	Vertical	Barnett
LDTS-021	Lake Davis No.1	4143.7	Vertical	Barnett
LDTS-022	Lake Davis No.1	4145.7	Vertical	Barnett
LDTS-023	Lake Davis No.1	4151.7	Vertical	Barnett
LDTS-024	Lake Davis No.1	4154.5	Vertical	Barnett
LDTS-025	Lake Davis No.1	4158.4	Vertical	Barnett
LDTS-026	Lake Davis No.1	4164.4	Vertical	Barnett
LDTS-027	Lake Davis No.1	4168.2	Vertical	Barnett
LDTS-028	Lake Davis No.1	4175.1	Vertical	Barnett
LDTS-029	Lake Davis No.1	4177.6	Vertical	Barnett
LDTS-030	Lake Davis No.1	4181.3	Vertical	Barnett
LDTS-031	Lake Davis No.1	4183.3	Vertical	Barnett
LDTS-032	Lake Davis No.1	4184.3	Vertical	Barnett
LDTS-033	Lake Davis No.1	4188.4	Vertical	Barnett
LDTS-034	Lake Davis No.1	4195.9	Vertical	Barnett
LDTS-035	Lake Davis No.1	4196.3	Vertical	Barnett

Table A1: continued

LDTS-036	Lake Davis No.1	4197.8	Vertical	Barnett
LDTS-037	Lake Davis No.1	4198.9	Vertical	Barnett
LDTS-038	Lake Davis No.1	4206.6	Vertical	Barnett
LDTS-039	Lake Davis No.1	4207.6	Vertical	Barnett
LDTS-040	Lake Davis No.1	4209.0	Vertical	Barnett
LDTS-041	Lake Davis No.1	4210.5	Vertical	Barnett
LDTS-042	Lake Davis No.1	4215.0	Vertical	Barnett
LDTS-043	Lake Davis No.1	4217.5	Vertical	Barnett
LDTS-044	Lake Davis No.1	4218.5	Vertical	Barnett
LDTS-045	Lake Davis No.1	4226.2	Vertical	Barnett
LDTS-046	Lake Davis No.1	4229.6	Vertical	Barnett
LDTS-047	Lake Davis No.1	4230.6	Vertical	Barnett
LDTS-048	Lake Davis No.1	4232.4	Vertical	Barnett
LDTS-049	Lake Davis No.1	4233.4	Vertical	Barnett
LDTS-050	Lake Davis No.1	4237.4	Vertical	Barnett
LDTS-051	Lake Davis No.1	4239.0	Vertical	Barnett
LDTS-052	Lake Davis No.1	4239.9	Vertical	Barnett
LDTS-053	Lake Davis No.1	4240.5	Vertical	Barnett
LDTS-054	Lake Davis No.1	4240.8	Vertical	Ives Breccia

Table A2: XRF sampling intervals on Hamilton cores.

Core	Location	Depth Interval (ft)	Resolution
Mesquite No.1	Hamilton, Texas	3639.3 to 3828.8	6 inches
Lake Davis No.1	Hamilton, Texas	4024.2 to 4243.5	6 inches

Table A3: SEM samples used in this study

Sample	Core	Depth (ft.)
LDSEM-001	Lake Davis No.1	4167.5
LDSEM-002	Lake Davis No.1	4188
LDSEM-003	Lake Davis No,1	4189
LDSEM-004	Lake Davis No.1	4204

Table A4: Organic chemical data used in this study.

Core	Sample	Depth (ft)	LECO TOC	S1	S2	S3	Tmax (˚C)	Cal. R_o %	HI	OI
Mesquite No.1	Mesq-001	3696	3.35	2.86	5.90	0.24	440	0.76	176	7
Mesquite No.1	Mesq-002	3699	4.27	4.93	8.97	0.14	452	0.98	210	3
Mesquite No.1	Mesq-003	3712	4.10	5.31	8.31	0.13	449	0.92	203	3
Mesquite No.1	Mesq-004	3723	3.95	5.59	8.20	0.15	453	0.99	208	4
Mesquite No.1	Mesq-005	3737	4.62	5.05	9.74	0.20	451	0.96	211	4
Mesquite No.1	Mesq-006	3740	4.86	3.02	8.43	0.11	457	1.07	173	2
Mesquite No.1	Mesq-007	3752	7.33	4.20	14.26	0.11	460	1.12	195	2
Mesquite No.1	Mesq-008	3759	5.97	2.83	11.31	0.09	459	1.10	189	2
Mesquite No.1	Mesq-009	3759	4.67	2.91	8.69	0.15	458	1.08	186	3
Mesquite No.1	Mesq-010	3771	5.29	3.28	10.01	0.18	458	1.08	189	3
Mesquite No.1	Mesq-011	3783	8.05	3.81	16.44	0.20	458	1.08	204	2
Mesquite No.1	Mesq-012	3802	5.62	3.69	11.07	0.16	459	1.10	197	3
Mesquite No.1	Mesq-013	3819	3.25	2.32	6.64	0.07	449	0.92	204	2
Mesquite No.1	Mesq-014	3819	3.67	2.07	6.60	0.11	455	1.03	180	3
Mesquite No.1	Mesq-015	3822	2.91	2.25	5.73	0.12	446	0.87	197	4

Table A5: XRD data used in this study.

Core	Sample	Depth	Quartz (%)	Albite (%)	Fluorapatite (%)	Dolomite (%)	Calcite (%)	Illite (%)	Pyrite (%)	Total (%)
Lake Davis No.1	LD-001	4078.4	18.6	12.0	7.7	7.6	32.4	16.8	4.9	100.0
Lake Davis No.1	LD-002	4087.1	6.7	8.4	8.7	9.8	47.2	10.4	8.8	100.0
Lake Davis No.1	LD-003	4113.3	41.9	14.2	4.3	4.4	8.2	20.5	3.5	100.0
Lake Davis No.1	LD-004	4137.7	31.9	11.9	5.6	10.1	18.6	14.7	7.2	100.0
Lake Davis No.1	LD-005	4140.1	16.1	8.7	23.3	7.6	5.9	20.2	18.2	100.0
Lake Davis No.1	LD-006	4158.4	29.4	7.2	8.2	7.1	8.4	26.2	13.5	100.0
Lake Davis No.1	LD-007	4164.4	28.7	12.3	7.3	8.1	6.9	25.9	10.8	100.0
Lake Davis No.1	LD-008	4181.5	13.6	9.7	11.1	8.6	18.6	19.3	19.1	100.0
Lake Davis No.1	LD-009	4184.4	14.5	12.8	10.4	12.4	27.9	12.7	9.3	100.0
Lake Davis No.1	LD-010	4195.9	17.0	9.3	7.6	11.7	32.1	15.2	7.1	100.0
Lake Davis No.1	LD-011	4206.6	19.5	9.9	8.1	8.3	29.1	14.9	10.2	100.0
Lake Davis No.1	LD-012	4226.2	18.0	9.7	9.8	14.0	24.2	16.5	7.8	100.0
Lake Davis No.1	LD-013	4110.1	37.0	13.5	8.5	8.4	6.6	18.3	5.4	100.0
Lake Davis No.1	LD-014	4117.4	47.5	8.9	4.7	8.6	6.6	18.3	5.4	100.0
Lake Davis	LD-015	4123	31.5	15.5	6.8	7.8	8.2	22.8	7.4	100.0

Table A5: continued

No.1										
Lake Davis No.1	LD-016	4155.7	29.3	15.9	5.3	7.3	7.7	24.5	10.0	100.0
Lake Davis No.1	LD-017	4175.5	16.2	8.2	6.3	28.9	18.6	14.5	7.3	100.0
Lake Davis No.1	LD-018	4200.8	33.7	11.9	5.4	8.4	8.0	23.5	9.1	100.0
Mesquite No.1	Mes-001	3734	34.0	13.0	0.0	9.0	7.0	33.0	4.0	100.0
Mesquite No.1	Mes-002	3756.5	18.0	12.0	1.0	9.0	23.0	30.0	8.0	100.0
Mesquite No.1	Mes-003	3768	23.0	11.0	4.0	11.0	20.0	25.0	6.0	100.0
Mesquite No.1	Mes-004	3780	30.0	14.0	2.0	3.0	11.0	34.0	6.0	100.0
Mesquite No.1	Mes-005	3811	39.0	12.0	1.0	7.0	7.0	30.0	4.0	100.0
Mesquite No.1	Mes-006	3824.4	41.0	13.0	0.0	6.0	1.0	36.0	3.0	100.0

REFERENCES

Abouelresh, M. O., and R. M. Slatt, 2011, Shale depositional processes: Example from the Paleozoic Barnett Shale, Fort Worth Basin, Texas, USA, Central European Journal of Geosciences, v. 3, No. 4, p. 398-409.

Abouelresh, M. O., and R. M. Slatt, 2012, Lithofacies and sequence stratigraphy of the Barnett Shale in east-central Fort Worth Basin, Texas AAPG Bulletin, v. 96, p. 1-22

Algeo, T. J., 2004, Can marine anoxic events draw down the trace element inventory of seawater?, Geology, v. 32, No. 12, p. 1057-1060.

Algeo, T. J., and T. W. Lyons, 2006 Mo–total organic carbon covariation in modern anoxic marine environments: Implications for analysis of paleoredox and paleohydrographic conditions, Paleoceanography, v. 2, No. 1.

Alldredge, A. L., and M. J. Youngbluth, 1985, The significance of macroscopic aggregates (marine snow) as sites for heterotrophic bacterial production in the mesopelagic zone of the subtropical Atlantic, Deep Sea Research Part A. Oceanographic Research Papers, v. 32, No. 12, p. 1445-1456.

Alldredge, A. L., and M. W. Silver, 1988, Characteristics, dynamics and significance of marine snow, Progress in oceanography, *v.* 20, No. 1, p. 41-82.

Baldwin, G. J., 2014, The stratigraphy and geochemistry Of the Rapitan Iron Formation, Northwest Territories And Yukon, Canada [Ph.D. Dissert.]: Laurentian University Of Sudbury, 248 p.

Baturin, G. N., 1982, Phosphorites on the sea floor: Origin, composition, and distribution: New York, New York, Elsevier Scientific, 343 p

Berner, R. A., 1970, Sedimentary pyrite formation, American Journal of Science, v. 268, No. 1, p. 1-23.

Bernhard, J.M. and C.E. Reimers, 1991, Benthic foraminiferal population fluctuations related to anoxia: Santa Barbara Basin. Biogeochemistry, v. 15, p. 127–149.

Bernhard, J.M., P.T. Visscher, and S. S. Bowser, 2003, Sub-millimeter life positions of Bacteria, protists, and metazoans in laminated sediments of the Santa Barbara Basin, Limnology and Oceanography, v. 48, p. 813–828.

Blakey, R. C., 2013, Paleogeography and tectonic history of North America: North American, Key Time-Slice Paleogeographic Maps, Carboniferous Mississippian (308 Ma),

< http://jan.ucc.nau.edu/~rcb7/nam.html> Accessed August 7, 2013.

Boggs, S. Jr., 1987, Principles of sedimentology and stratigraphy: Columbus, Ohio, Merrill Publishing Co., 784 p.

Boles, J. R., and S. G. Franks, 1979, Clay diagenesis in Wilcox sandstones of southwest Texas: implications of smectite diagenesis on sandstone cementation, Journal of Sedimentary Research 49, No.1.

Bowker, K. A, 2002, Recent developments of the Barnett Play, Fort Worth basin, Innovative Gas Exploration Concepts Symposium: Rocky Mountain Association of Geologists and Petroleum Technology Transfer Council.

Briggs, G., and D. Roeder, 1975, Sedimentation and plate tectonics, Ouachita Mountains and Arkoma basin, Dallas Geological Society, p. 1-22.

Browning, J., S. W. Tinker, S. Ikonnikova, G. Gulen, E. Potter, Q, Fu, S, Horvath, T. Patzek, F. male, W, Fisher and F. Roberts, 2013, Study develops decline analysis, geologic parameters for reserves, production forecast model-1, Oil and Gas Journal, v. 111, No. 8, p. 62-73.

Bunting, P. J., and J. A. Breyer, 2012, Lithology of the Barnett Shale (Mississippian), southern Fort Worth Basin, Texas--Giant resources for the 21st century: AAPG Memoir 97, p. 322–343.

Bunting, P.J., 2007, Petrographic analysis of the Barnett Shale in the Fort Worth Basin [M.S. thesis]: Fort Worth, Texas Christian University, 101 p.

Byers, C. W., 1977, Biofacies patterns in euxinic basins: A general model, in H. E. Cook and P. Enos, eds., Deep-water carbonate environments: SEPM Special Publication, v. 25, p. 203–219.

Chekhovskaya, M.P., 1973, Distribution of benthic Foraminifers in the Northeastern Bering Sea, Oceanology, v. 13, p. 571–575.

Cheney, M. G., 1940, Geology of North-Central Texas, AAPG Bulletin, v. 24, no. 1, p. 65-118.

Dembicki, H, Jr., 2009, Three common source rock evaluation errors made by geologists during prospect or play appraisals, AAPG Bulletin v. 93, No. 3, p. 341-356.

Dinur, D, B. Spiro, and Z. Aizenshtat, 1981, The distribution and isotopic composition of sulfur in organic-rich sedimentary rocks, Chemical Geology v. 31, p. 37-51.

Dunham, R. J., Classification of carbonate rocks according to depositional textures, 1962, AAPG Specail Volumes: Classification of Carbonate Rocks—A Symposium, p. 108-121.

Flawn, P. T., A., Goldstein, Jr., P. B. King, and C. E., Eaver, 1961, The Ouachita System: Publication No. 6120, Bureau of Economic Geology, The University of Texas, Austin, Texas, 401 p.

Flippin, J. W., 1982, The stratigraphy, structure, and economic aspects of the Paleozoic strata in Erath County, North-Central Texas, in C. A. Martin, ed., Petroleum geology of the Fort Worth Basin and Bend Arch area, Dallas Geological Society, p. 129-155.

Flügel, E., 2004, Microfacies of carbonate rocks: analysis, interpretation and application, Springer, 984 p.

Folk, R. L., 1980, Petrology of sedimentary rocks: Austin, Texas, Hemphills Publishing Co., 182 p.

FöIlmi, K. B., and K. A. Grimm, 1990, Doomed pioneers: Gravity-flow deposition and bioturbation in marine oxygen-deficient environments, Geology, v. 18, No.11, p. 1069-1072.

Föllmi, K. B., R.E. Garrison, and K.A. Grimm, 1991, Stratification in phosphatic sediments: Illustrations from the Neogene of Central California in G. Einsele, W. Ricken, A. Seilacher (Eds.), Cycles and Events in Stratigraphy, Springer, Berlin, p. 492–507.

Föllmi, K. B., and R. E. Garrison, 1991, Phosphatic sediments, ordinary or extraordinary deposits? The example of the Miocene Monterey Formation (California), Controversies in Modern Geology, Academic Press, London, p. 55-84.

Glenn, C, R., K. B., Follmi, S. R. Riggs, G. N., Baturin, K. A., Grimm, J. Trappe and A. M. Abed, 1994, Phosphorus and phosphorites: sedimentology and environments of formation, Eclogae Geologicae Helvetiae v. 87, No. 3, p. 747-788.

Gowing, M. M., 1986, Trophic biology of phaeodarian radiolarians and flux of living radiolarians in the upper 2000 m of the North Pacific central gyre, Deep Sea Research Part A. Oceanographic Research Papers v. 33, No. 5, p. 655-674.

Graham, S. A., W. R. Dickinson, and R. V., Ingersoll, 1975, Himalayan-Bengal model for flysch dispersal in the AppalachianOuachita system." Geological Society of America Bulletin v. 86, No. 3, p. 273-286.

Gransch, J. A. and J. Posthuma, 1974, On the origin of sulfur in crudes, Advances in Organic Geochemistry, p. 727-739.

Gutschick, R., and C. Sandberg, 1983, Mississippian continental margins on the conterminous United States, in D. J. Stanley and G. T. Moore, The shelf break: Critical interface on continental margins, SEPM Special Publication v. 33, p. 79– 96.

Hampton, M. A., 1972, The role of subaqueous debris flow in generating turbidity currents. Journal of Sedimentary Research, v. 42, No. 4, p. 775-793.

Henry, J. D, 1982, Stratigraphy of the Barnett Shale (Mississippian) and associated reefs in the northern Fort Worth Basin, Petroleum Geology of the Fort Worth Basin and Bend Arch Area, p. 157-177.

Hickey, J. J., and B. Henk, 2007, Lithofacies summary of the Mississippian Barnett Shale, Mitchell 2 TP Sims well, Wise County, Texas, AAPG Bulletin v. 91, No. 4, p. 437-443.

Hoffman, P., 1973, Evolution of an early Proterozoic continental margin: the Coronation geosyncline and associated aulacogens of the northwestern Canadian shield, Phil. Trans, R. Soc. London, A., v. 273, p. 547-581

Hoffman, P., 1974, Aulacogens and their genetic relation to geosynclines with a Proterozoic example from Great Slave Lake Canada, SEPM, v. 19, No. 18.

Iverson, R, M., 1997, The physics of debris flows, Reviews of geophysics, v. 35, No. 3, p. 245-296.

Jarvie, D. M., B. L. Claxton, Floyd, B. Henk, and J. T. Breyer, 2001, Oil and Shale Gas from the Barnett Shale, Ft. Worth Basin, Texas, AAPG National Convention, June 3-6, 2001, Denver, CO, AAPG Bulletin, v. 85, No. 13 (Supplement), p. A100.

Jarvie, Daniel M., Ronald J. Hill, and Richard M. Pollastro. "Assessment of the gas potential and yields from shales: The Barnett Shale model." *Oklahoma Geological Survey Circular* 110 (2005): 9-10.

Jarvie, D. M., R. j. Hill, T. E. Ruble, and R. M. Pollastro, 2007, Unconventional shale-gas systems: The Mississippian Barnett Shale of north-central Texas as one model for thermogenic shale-gas assessment, AAPG Bulletin, v. 91, No. 4, p. 475-499.

Keller, G. R., and S. E. Cebull, 1973, Plate tectonics and the Ouachita system in Texas, Oklahoma, and Arkansas, Geological Society of America Bulletin, v. 84, No, 5, p. 1659-1666.

Kier, R. S., L. F. Brown Jr., and E. F. McBride, 1980, The Mississippian and Pennsylvanian (Carboniferous) systems in the United States—Texas: Bureau of Economic Geology,

University of Texas at Austin, Geological Circular 80-14. Reprinted from U. S. Geological Survey Professional Paper 1110-S, 45 p.

Kling, S. A., and D. Boltovskoy, 1995, Radiolarian vertical distribution patterns across the southern California Current, Deep Sea Research Part I: Oceanographic Research Papers, v. 42, No. 2, p. 191-231.

Kuich, N. F., 1964, Carboniferous stratigraphy of the Sloan area, San Saba county, Texas, [M.S. Thesis], Austin The University of Texas at Austin, 181 p.

Lineback, J. A., 1969, Illinois Basin--Sediment-Starved During Mississippian, AAPG Bulletin, v. 53, No. 1, p. 112-126.

Loucks, R.G., and S. C. Ruppel, 2007, Mississippian Barnett Shale: Lithofacies and depositional setting of a deep-water shale-gas succession in the Fort Worth Basin, Texas, AAPG Bulletin v. 91, No. 4, p. 579-601.

Loucks, R. G., R. M. Reed, R. M. Ruppel, and D. M., Jarvie., 2009, Morphology, genesis, and distribution of nanometer-scale pores in siliceous mudstones of the Mississippian Barnett Shale, Journal of Sedimentary Research, v. 79, No. 12, p. 848-861.

Loucks, R. G., R. M. Reed, R. M. Ruppel, and U. Hammes, 2012, Spectrum of pore types and networks in mudrocks and a descriptive classification for matrix-related mudrock pores, AAPG Bulletin, v. 96, No. 6, p. 1071-1098.

Loucks, R. G., and R. M., Reed, 2014, Scanning-Electron-Microscope petrographic evidence for distinguishing organic matter pores associated with depositional orgaic matter versus igrated organic matter in mudrocks, GCAGS Journal, v. 3, (in press).

Lowrie, W., 2007, Fundamentals of geophysics, Cambridge University Press, 2nd edition, 390 p.

Lynch, F. L, 1997, Frio shale mineralogy and the stoichiometry of the smectite-to-illite reaction: the most important reaction in clastic sedimentary diagenesis, Clays and Clay Minerals, v. 45, No. 5, p. 618-631.

Lyons, T. W., and S. Severmann, 2006, A critical look at iron paleoredox proxies: New insights from modern euxinic marine basin, Geochimica et Cosmochimica Acta, v. 70, No. 23, p. 5698-5722.

Matthews, H. L., G. W. Schein, and M. R. Malone, 2007, Stimulation of gas shales: they're all the same—right?, SPE Hydraulic Fracturing Technology Conference, SPE, p. 16.

McDonnell, A., R. G. Loucks, and T. Dooley, 2007, Quantifying the origin and geometry of circular sag structures in northern Fort Worth Basin, Texas: Paleocave collapse, pull-apart fault systems, or hydrothermal alteration?, AAPG bulletin, v. 91, No. 9, p. 1295-1318.

McKee, E. D., and R.C. Gutschick, 1969, History of the Redwall Limestone of northern Arizona, GSA Memoir v. 114, p. 1-700.

McKinney, W. N., 1963, Carboniferous stratigraphy of the San Saba area, San Saba county, Texas, [M.S. Thesis], Austin, The University of Texas at Austin, Austin, 164 p.

Merrill, G. K., 1980, Road log-Day two, in Geology of the Llano region, central Texas: Guidebook to the Annual Field Trip of The West Texas Geological Society, Oct. 19-21, p. 60-199.

Milliken, K. L., 1994. Cathodoluminescent textures and the origin of quartz silt in Oligocene mudrocks, South Texas, Journal of Sedimentary Research, v. 64A, p. 567–571.

Milliken, K. L., S. J. Choh, P. k. Papazis and J. Schieber, 2007, "Cherty" stringers in the Barnett Shale are agglutinated foraminifera, Sedimentary Geology, v. 198, No. 3, p. 221-232.

Milliken, K. L., R. J. Day-Stirrat, P. K. Papazis, and C. Dohse, 2012, Carbonate Lithologies of the Mississippian Barnett Shale, Fort Worth Basin, Texas, in J. A. Breyer, ed., Shale reservoirs—Giant resources for the 21st century, AAPG Memoir, v. 97, p. 290-321.

Montgomery, L., D, M. Jarvie, K. A. Bowker, and R. M. Pollastro, 2005, Mississippian Barnett Shale, Fort Worth basin, north-central Texas: Gas-shale play with multi–trillion cubic foot potential, AAPG Bulletin, v. 89, p. 155-175,

Morris, R. C., 1974, Sedimentary and tectonic history of the Ouachita Mountains, SEPM, Tectonics and Sedimentation (SP 22).

Mulder, T., and J. Alexander, 2001, The physical character of subaqueous sedimentary density flows and their deposits, Sedimentology, v. 48, No. 2, p. 269-299.

Oden, J. W., 1958, Carboniferous stratigraphy of the Leonard Ranch Area, San Saba County, Texas, [M.S. Thesis], Austin, The University of Texas at Austin, 158 p.

Orr, W. L., 1986, Kerogen/asphaltene/sulfur relationships in sulfur-rich Monterey oils, Organic Geochemistry 10, p. 499-516.

Orth, C. J., L.R. Gilmore, L.R. Quintana, and P.M. Sheehan, 1986, Terminal Ordovician extinction: Geochemical analysis of the Ordovician/Silurian boundary, Anticosti Island, Quebec, Geology, v. 14, No. 5, p. 433-436.

Papazis, K. P., 2005, Petrographic characterization of the Barnett Shale, Fort Worth Basin, Texas [M. S. Thesis]: Austin, The University of Texas at Austin, 142 p.

Papazis, P. K., and K. L. Milliken, 2005, PS Cathodoluminescent Textures and the Origin of Quartz in the Mississippian Barnett Shale, Fort Worth Basin, Texas, Poster presentation at AAPG Annual Convention, Calgary, Alberta, June 19-22, 2005.

Peters, K. E., 1986, Guidelines for evaluating petroleum source rock using programmed pyrolysis, AAPG Bulletin, v. 70, No. 3, p. 318-329.

Peters, K. E., and M. R. Cassa, 1994, Applied source rock geochemistry, AAPG Memoir, v. 60, p. 93-120.

Pickens, W. R., 1959, Carboniferous stratigraphy of the Jackson Ranch Area, Lampasas County, Texas, [M.S. Thesis], Austin, The University of Texas at Austin, 145 p.

Plummer, F. B., and Moore, R. C., 1922, Stratigraphy of the Pennsylvanian formations of North-Central Texas: Univ. Texas, Bulletin, No. 2132.

Plummer, F. B., and Scott, Gayle, 1937, Upper Paleozoic ammonites in Texas, in The geology of Texas, v. 3, pt.1, Univ. Texas, Bulletin, No. 3701.

Pollastro, R.M., J. H. Ronald, D.M. Jarvie, and M. E. Henry, 2003, Assessing Undiscovered Resources of the Barnett-Paleozoic Total Petroleum System, Bend Arch–Fort Worth Basin Province, Texas: Online adaptation of presentation at AAPG, Southwest Section Meeting, Fort Worth, TX, March 2003.

Pollastro, R.M., D.M. Jarvie, J. H. Ronald, and C.W. Adams, 2007, Geologic framework of the Mississippian Barnett Shale, Barnett-Paleozoic total petroleum system, Bend arch-Fort Worth Basin, Texas. AAPG Bulletin, v. 91, No. 4, p. 405-436.

Potter, P.E., J. B. Maynard, and P. J. Depetris, 2004, Mud and Mudstones: introduction and overview, Springer, 297 p.

Prevot, L., 1982, Proposal for normalized easy description of the so-called palaeophosphorites. IGCP Proj 156, Newsletters, v. 10, p. 24-31.

Pufahl, P. K., and K.A. Grimm, 2003, Coated phosphate grains: Proxy for physical, chemical, and ecological changes in seawater, Geology, v. 31, No. 9, p. 801-804.

Radke, B. M., and R. L. Mathis, 1980, On the formation and occurrence of saddle dolomite, Journal of Sedimentary Research, v. 50, No. 4, p. 1149-1168.

Raiswell, R., and R. A. Berner, 1986, Pyrite and organic matter in Phanerozoic normal marine shales." Geochimica et Cosmochimica Acta, v. 50, No. 9, p. 1967-1976.

Raiswell, R., 1971, The growth of Cambrian and Liassic concretions, Sedimentology, v. 17, No. 3-4, p. 147-171.

Raiswell, R., F. Buckley, R. A. Berner, and T. F. Anderson, 1988, Degree of pyritization of iron as a paleoenvironmental indicator of bottom-water oxygenation. Journal of Sedimentary Petrology, v. 58, No.5, p. 812–819.

Reed, R. M., and R. G. Loucks, 2007, Imaging nanoscale pores in the Mississippian Barnett Shale of the northern Fort Worth Basin, AAPG Annual Convention Abstracts, v. 16.

Rieke, H. H., and G. V. Chilingarian, 1974, Compaction of argillaceous sediments, Elsevier Science, 438 p.

Ross, C. A., and J. R. P. Ross, 1987, Late Paleozoic sea levels and depositional sequences, in C. A. Ross and D. Haman, eds., Timing and deposition of eustatic sequences: Constraints on seismic stratigraphy: Cushman Foundation for Foraminiferal Research Special Publication 24, p. 137– 149.

Rowe, H. D., R. G. Loucks, S. C. Ruppel, and S. M. Rimmer, 2008, Mississippian Barnett Formation, Fort Worth Basin, Texas: Bulk geochemical inferences and Mo–TOC constraints on the severity of hydrographic restriction, Chemical Geology, v. 257, No.1, p. 16-25.

Rowe, H. D., N. Hughes, and K. Robinson, 2012, The quantification and application of handheld energy-dispersive x-ray fluorescence (ED-XRF) in mudrock chemostratigraphy and geochemistry." Chemical Geology, v. 324, 122-131.

Ruppel, S. C., and C. Kerans. 1987, Paleozoic Buildups and Associated Facies, Llano Uplift, Central Texas. Austin, Austin Geological Society Guidebook 10.

Schieber, J., 2009, Discovery of agglutinated benthic foraminifera in Devonian black shales and their relevance for the redox state of ancient seas, Palaeogeography, Palaeoclimatology, Palaeoecology, v. 271, No. 3, p. 292-300.

Schmoker, J. W, 1995, Method for assessing continuous-type (unconventional) hydrocarbon accumulations, DL Gautier, GL Dolton, KI Takahashi, and KL Varnes, eds.

Scholle, P.A., and D. S. Ulmer-Scholle, 2003, A Color Guide to the Petrography of Carbonate Rocks: Grains, Textures, Porosity, Diagenesis, AAPG Memoir, v. 77, 474 p.

Selles-Martinez, J, 1996, Concretion morphology, classification and genesis, Earth-Science Reviews, v. 41, No. 3, p. 177-210.

Sternbeck, J., G. Sohlenius, and R. O. Hallberg, 2000, Sedimentary trace elements as proxies to depositional changes induced by a Holocene fresh-brackish water transition, *Aquatic Geochemistry* v. 6, No. 3, p. 325-345.

Stitt, J. H., 1964, Carboniferous stratigraphy of the Bend Area, San Saba County, Texas, [M.S. Thesis], Austin, The University of Texas at Austin, 152 p.

Stow, D. A. V., and A. R. Tabrez, 1998, Hemipelagites: processes, facies and model, *Geological Society, London, Special Publications* v. 129, No. 1, p. 317-337.

Stow, D.A.V., J. C. Faugeres, A. Viana, and E. Gonthier, 1998, Fossil contourites: a critical review, Sedimentary Geology, v. 115, No. 1, p. 3-31.

Stow, D. A. V., A-Y. Huc, and P. Bertrand, 2001, Depositional processes of black shales in deep water, Marine and Petroleum Geology, v. 18, No. 4, p. 491-498

Stow D. A. V., J. C., Faugères, J. A., Howe, 2002, Bottom currents, contourites and deep-sea sediment drifts: current state-of-the-art, Geological Society, London, Memoirs 22, No.1, p. 7-20.

Takahashi, K., and H. Y. Ling, 1980, Distribution of Sticholonche (Radiolaria) in the upper 800 m of the waters in the Equatorial Pacific, Marine Micropaleontology v. 5, p. 311-319.

Trappe, J., 1998, Phanerozoic phosphorite depositional systems: A dynamic model for a sedimentary resource system." Lecture Notes in Earth Sciences (Book 76), Berlin Springer, 316 p.

Tribovillard, N., T. J. Algeo, T. Lyons, and A. Riboulleau, 2006, Trace metals as paleoredox and paleoproductivity proxies: an update, Chemical Geology, v. 232, No. 1, p. 12-32.

Tribovillard, N., et al, 1994, Geochemical study of organic-matter rich cycles from the Kimmeridge Clay Formation of Yorkshire (UK): productivity versus anoxia, Palaeogeography, Palaeoclimatology, Palaeoecology, v. 108, No. 1, p. 165-181.

Turner, G. L., 1957, Paleozoic stratigraphy of the Fort Worth basin: Abilene and Fort Worth Geological Societies, Joint Field Trip Guidebook, W.C. Bell, (leader), p. 57-77.

Turner, N. L., 1970, Carboniferous stratigraphy of western San Saba County, Texas, [Ph. D. Dissertation], Austin, the University of Texas at Austin, 378 p.

Turner, J. T., 2002, Zooplankton fecal pellets, marine snow and sinking phytoplankton blooms, Aquatic Microbial Ecology v. 27, No. 1, p. 57-102.

Van Krevelen, D. W., 1950, Graphical-statistical method for the study of structure and reaction processes of coal, Fuel, v. 29, No. 12, p. 269-84.

Walper, J. L., and C. L. Rowett, 1972, Plate tectonics and the origin of the Caribbean Sea and the Gulf of Mexico, GCAGS, v. 22, p. 105-116

Walper, J. L., 1977, Paleozoic tectonics of the southern margin of North America, GCAGS, v. 27, p. 230-241.

Walper, J. L., 1982, Plate tectonic evolution of the Fort Worth basin, in Martin, C. A., ed., Petroleum geology of the Fort Worth basin and Bend arch area: Dallas Geological Society, p. 237–251.

Watson, W. G., 1980, Paleozoic stratigraphy of the Llano Uplift area in D. Windle, ed., Guidebook to the annual field trip of the West Texas Geological Society, October 19-21, 1980, Publication, vol. 80-73, West Texas Geological Society, p. 27-51

Wedepohl, K. H, 1971, Environmental influences on the chemical composition of shales and clays, Physics and Chemistry of the Earth v. 8, p. 305-333.

Weeks, L. G, 1957, Origin of carbonate concretions in shales, Magdalena Valley, Colombia, GSA Bulletin, v. 68, No. 1, p. 95-102.

White, J. R., 1948, A study of the Mississippian deposits in the subsurface of North-Central Texas, [M. S. thesis], Fort Worth, Texas Christian University.

Wiggins, W. D., 1982, Depositional history and microspar development in reducing pore water, Marble Falls Limestone (Pennsylvanian) and Barnett Shale (Mississippian), central Texas, [Ph. D., Dissert.], Austin, The University of Texas at Austin.

Wignall, P. B, 1994, Black Shales, Vol. 30. Oxford: Clarendon Press, 144 p.

Wignall, P. B., R. Newton, and M. E. Brookfield, 2005, Pyrite framboid evidence for oxygen-poor deposition during the Permian–Triassic crisis in Kashmir, Palaeogeography, Palaeoclimatology, Palaeoecology, v. 216, No. 3, p. 183-188.

Wilkin, R. T., H. L. Barnes, and S. L. Brantley, 1996, The size distribution of framboidal pyrite in modern sediments: an indicator of redox conditions, Geochimica et Cosmochimica Acta, v. 60, No. 20, p. 3897-3912.

Wood, S. G., 2013, Lithofacies, depositional environments, and sequence stratigraphy of the Pennsylvanian (Morrowan-Atokan) Marble Falls Formation, Central texas, [M.S. Thesis], Austin, The University of Texas at Austin, 276 p.

Yurewicz, D. A., 1977, Sedimentology of Mississippian basin-facies carbonates, New Mexico and west Texas— The Rancheria Formation in H. E. Cook and P. Enos, eds., Deep-water carbonate environments: SEPM Special Publication 25, p. 203–219.

Zhang, T., R., Y, K. L., Milliken, S. C., Ruppel, R. J., Pottorf, X. Sun, 2014, Chemical and isotopic composition of gases released by crush methods from organic rich mudrocks, Organic Geochemistry, v. 73, p. 16-28.

VITA

Xufeng Liu was born and grew up in Dongying, Shandong Province, P.R. China. After the college entrance examination, he inherited his father's footprint to become a geologist. Then he spent the first two years of undergraduate time in China University of Petroleum Beijing (CUPB) from 2008 to 2010. In CUPB, he participated the "2+2" program between CUPB and University of Tulsa, Oklahoma for the other two years spent in the United States. In May 2012, he graduated from both of the two universities with double degrees of Bachelor of Science in Geology. Then, he continued pursuing on geology by attending the master program of the University of Texas at Austin in August 2012. While at the University of Texas, he worked as a graduate research assistant for the Mudrock System Research Laboratory, Bureau of Economic Geology. After graduated from University of Texas, he will move back to P.R. China to work in the oil and gas industry.

Permanent email: liu919xf@gmail.com

This thesis was typed by Xufeng Liu